ENCOUNTERS OF PROTOSTELLAR DISKS AND SUBSTELLAR OBJECTS

ENCOUNTERS OF PROTOSTELLAR DISKS AND FORMATION OF SUBSTELLAR OBJECTS

By

SIJING SHEN, B.SC.

A Thesis
Submitted to the School of Graduate Studies
in Partial Fulfilment of the Requirements
for the Degree
Master of Science

McMaster University

Master of Science (2006) McMaster University

(Department of Physics and Astronomy) Hamilton, Ontario

TITLE: Encounters of Protostellar Disks and Formation of Substellar Objects

AUTHOR: Sijing Shen, B.Sc.

SUPERVISOR: Dr. James Wadsley

NUMBER OF PAGES: xiii, 141

Abstract

Fragmentation during encounters between protostellar disks provides a possible scenario for the formation of substellar objects such as brown dwarfs and planets. A series of simulations of protostellar disk encounters were performed to investigate the fragmentation under different encounter parameters, and to characterize the properties of any resultant fragments. It was found that the initial disk minimum Toomre Q must satisfy $Q_{ini} \lesssim 1.1$ for the fragmentation to be induced by the encounters. Fragments of substellar mass can form via disk fragmentation, shock layer fragmentation and tidal tail fragmentation, and the effectiveness of each mechanism is closely related to the initial disk configuration. The fragmentation is also constrained by the relative encounter velocity since the number of fragments decreases quickly with increasing velocity.

In comparing to previous studies of protostellar disk encounters it was also found that resolving both the local Jeans Mass during the encounter and the disks' vertical structure are critical to prevent artificial fragmentation and give the correct picture. Heating and cooling rates were estimated in both the optically thin and thick regimes. The comparison between the two indicates that during strong impacts the heating rate increases rapidly but is still comparable to the cooling rate, so the locally isothermal equation of state used in this study is an acceptable approximation.

32 clumps formed in various $Q_{ini} = 0.9$ disk-disk encounters were taken as the sample in an analysis of fragment properties and prospects for their further evolution. The results show that the clump masses are all less than

the hydrogen burning mass limit $\sim 0.075 M_{\odot}$, so the objects are substellar. Most of the clumps are of brown dwarf mass since the formation of planetary-mass clumps is suppressed due to numerical resolution. The mass distribution is broadly consistent to the observed initial mass function in Pleiades. The clumps have highly flattened disk-like shapes and possess large spin angular momentum, which implies that young brown dwarfs may develop disks, jets, or planetary mass companions. About one third of the fragments are unbound to the stars and likely to form free floating brown dwarfs. Orbital analyses of the clumps which are bound to the stars show that there is a lack of close brown dwarf companions ($R < 3\ AU$), which is consistent to the observed "brown dwarf desert". Many of the orbits are highly eccentric and intersect with other orbits, so ejection of some clumps due to gravitational scattering is likely. Also, dispersion of gas during the encounter and the high spin angular momentum of the clumps may provide mechanisms other than ejection to prevent the clumps from accreting more mass, making the simulated clumps representative of the long term substellar mass function.

Acknowledgements

I would like to firstly thank my supervisor Dr. James Wadsley for providing me with this exciting project and giving me wonderful guidance and continous support through the progress of the project. Without his patience and help, the accomplishment of this project would have been impossible.

I would also like to thank my Masters committee members Dr. Ralph Pudritz and Dr. Doug Welch for their helpful suggestions and comments on this project.

A heartfelt thanks to my parents for their love and supports in the past two years, and to my friend Albert Zhengji Zhuge, who gives me the warmest support whenever I have difficulties.

I would also like to thank the following friends in this wonderful department at McMaster, from whom I got immeasurable helps during my research and writing, and for a lot of fun in leisure time: Marie-Josee Colbert, David Cooke, Jonathan Downing, Laura Filion, Pamela Klaassen, Soko Matsumura, Colin McNally, Kiri Nichol, Nicolas Petitclerc, Lesley Watters and Kristin Woodley.

Table of Contents

List of Figures

List of Tables

Chapter 1

Introduction

1.1 Overview

Substellar objects such as brown dwarfs and planets are abundant in our universe according to the stellar initial mass function. However, their formation scenarios have still not been completely understood, since their masses are generally less than 10% of the smallest clump a molecular could core is expected to form by inside-out collapse via gravitational instability.

In dynamical environments such as embedded clusters, interactions between protostars and their surrounding disks may play an important role in the formation of stellar systems. In particular, strong impulsive encounters between two extensive gaseous protostellar disks can induce local gravitational instabilities in the stable disks and produce gaseous condensations which have masses in the substellar regime. These encounters provide a possible way to explain the formation of substellar objects.

When studying strong interactions between gaseous disks, numerical simulations are often used to give a detailed picture, because of the intrinsic non-linearity of the interaction. However, numerical modeling and resolution play important roles in obtaining trustworthy results from a simulation. In this work, a numerical study of protostellar disk encounters is presented, and the parameter space of dynamical encounters is explored. The simulations adopt an improved disk model relative to previous work, in which the finite scale height of the disk is resolved and use high resolution to follow the fragmentation during the encounters.

1.2 Substellar Objects and Their Formation

1.2.1 Substellar Objects-Brown Dwarfs and Planets

Substellar objects are defined as objects with mass less than the hydrogen burning limit $\sim 0.075M_{\odot}$ (Oppenheimer et al., 2000). Conventionally, the family of substellar objects consists of two main categories: brown dwarfs, which have larger masses and substantial deuterium burning, and are found as both free-floating objects and star companions; planets, which have smaller masses ($\leq 0.013M_{\odot}$) and negligible deuterium burning, and are found as companions of stars most of time (Padoan & Nordlund, 2004; Marcy et al., 2000).

Observations have convincingly shown that there are large numbers of substellar objects in clusters and the field (Luhman et al., 1998; Mayor et al., 1998). The brown dwarfs and planets discovered reveal that the initial mass function (IMF), i.e., the number of objects per unit mass interval at the birth of these objects, turns out to be very flat when $M \leq 0.1M_{\odot}$ (Figure 1.1),

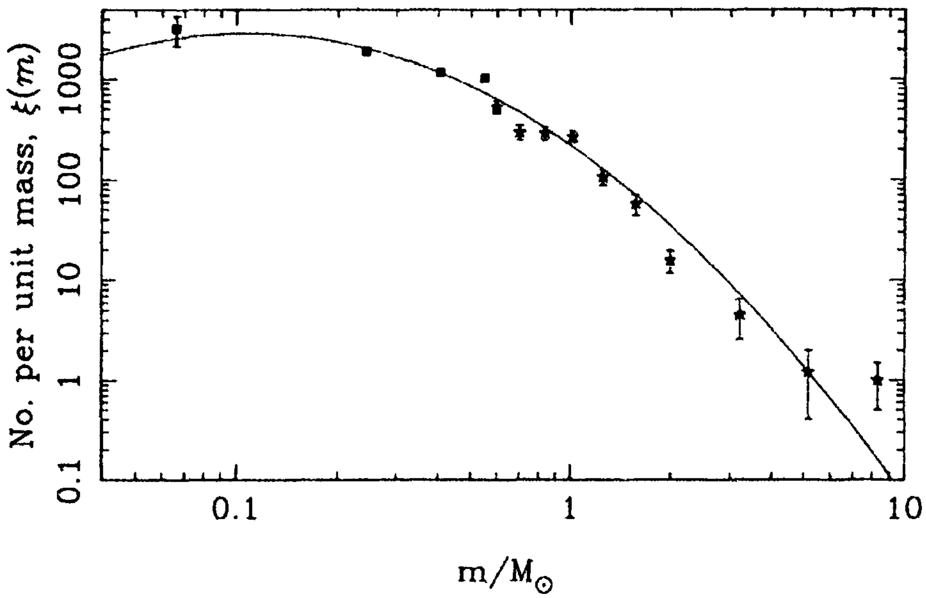

Figure 1.1 Stellar Initial Mass Function (IMF) in Pleiades with mass range 0.07 $M_{\odot}$ to 10 $M_{\odot}$. The flatness in low mass end indicates an abundance of substellar objects. Adapted from Hambly et al. (1999).

which indicates a large substellar population (Stahler & Palla , 2004; Bate et al., 2003).

1.2.2 Formation Scenarios of Substellar Objects

Despite the large population, the formation scenario of substellar objects are not completely understood. According to Bate et al. (2002), the Jeans Mass in typical isothermal molecular cloud cores is about 1 $M_{\odot}$, so fragments with substellar masses are too small to be produced from direct inside-out collapse and fragmentation of the molecular cloud cores. To solve this problem, many scenarios have been proposed. For brown dwarfs, the first scenario is that they can be formed from fragmentation of a much denser, low mass ($\sim 0.1 M_{\odot}$) core where the Jeans Mass can be on the substellar scale (e.g., Elmegreen, 1999). However, such cores are unlikely to be observed because of their short dynamical timescale (Bate et al., 2002). A second possibility is that they are formed in normal mass molecular cores but from secondary fragmentation of the dense regions and do not have enough time to accrete a lot of gas before being ejected from the dense region due to dynamical interactions. The ejection scenario was first proposed by Reipurth & Clarke (2001), and has been used to explain the lack of large-separation binary brown dwarfs and lack of brown dwarf companions for stars with masses larger than $0.5 M_{\odot}$ (the "brown dwarf desert")(Marcy & Butler, 1998, 2000; Halbwachs et al., 2000).

The ejection scenario was supported in the numerical studies by Bate et al. (2003), who simulated the collapse of a $50 M_{\odot}$ turbulent molecular cloud. The simulation showed a very dynamic formation process, where most of stars and protostellar disks formed via collapse of cores but most brown dwarfs formed from gravitational instability of disks. The low mass embryos had a high rate of ejection; hence those ejected stopped accreting gas. The simulation successfully reproduced the flatness in substellar IMF down to 0.1 $M_{\odot}$(cf. Figure. 10 in Bate et al. (2003)). However, due to limited resolution, the mass distribution below $0.1 M_{\odot}$ could not be produced. Also, the ejected brown-dwarf-mass clumps of sizes smaller than 10 AU were unresolved, which means the study was unable to be compared to the observational study of brown dwarf disks. Observationally, about 65±15% of young brown dwarfs exhibit infrared-excess emission, indicating the existence of disks around them (Muench et al., 2001).

As to the formation of planets, there are basically two scenarios: core accretion model, in which the planet core first forms by inelastic collision of dust in protoplanetary disk, then accretes enough gas to form a massive gaseous envelope around the core (Perri & Cameron , 1974). While planetesimal scenarios can explain the formation of terrestrial planets it has a timescale problem for gaseous exosolar planets, namely, the accretion of gas is too slow to result in the observed mass before the disk disappears. The second scenario is gravitational instability, which has the planet form via fragmentation of the protoplanetary disk (e.g., Mayer et al., 2004; Boss, 2001). Numerical simulations of the fragmentation of isolated disks show that there is no timescale problem for giant planet formation, but the fragmentation probability is sensitive to disk properties and thermal regulation (Mayer et al., 2004; Pickett et al., 2003).

It can be seen from both brown dwarf formation (Bate et al., 2003) and planet formation (Mayer et al., 2004; Pickett et al., 2003; Boss, 2001) that fragmentation of disks plays an important role in formation of clumps with substellar mass. However, as will be discussed in later section, not all the protostellar/protoplanetary disk would undergo gravitational instability spontaneously. Instead, in dense star forming regions, it is generally the interaction between protostars and disks that triggers non-linear growth of perturbations and fragmentation. Since the simulation of Bate et al. (2003) could not resolve the masses and sizes of small fragments due to the intrinsic large scale of their simulation, and isolated disk fragmentation is only suitable for a quiescent environment, it is worth studying dynamical interactions of protostars and protostellar disks at a smaller scale in order to explore their roles in substellar object formation and the properties of any resultant objects.

1.3 Protostellar Disks and Their Interaction

1.3.1 Protostars and Protostellar Disks–Formation and Evolution

The formation and existence of protostellar disks is an inevitable consequence of angular momentum conservation in the early stages of star formation. As mentioned in previous sections, protostars form inside molecular cloud cores via gravitational instability. The cores are mostly composed of cold molecular hydrogen (H_2) but also a small percentage of dust (about 1%), and they typically have mass of a few $M_\odot$ and number density $n_{H_2} = 10^3\ cm^{-3}$. The temperature of the core is around 10K. With these values the typical cloud core mass can be calculated and it is close to the local Jeans mass defined as

$$M_J = \frac{4\pi}{3}\rho(\frac{\lambda_J}{2})^3 \tag{1.1}$$

with the Jeans length, λ_J, given as

$$\lambda_J = \frac{\pi c_s^2}{G\rho}. \tag{1.2}$$

ρ is local density of the gas, G is Newton's Gravitational Constant and c_s is the sound speed defined as $c_s = \frac{k_B T}{m}$ for an ideal isothermal gas, with k_B the Boltzmann's constant and m the mean molecular mass.

The Jeans Length is the critical wavelength beyond which any perturbation grows exponentially. The Jeans Mass is the mass contained in a sphere with size of Jeans length, and therefore is the critical mass scale above which gravitational force exceeds gas pressure and causes collapse. Since typical molecular cloud cores are expected to have mass close to Jeans Mass, they are marginally unstable. Therefore, a little perturbation can trigger the formation of single protostar or multiple stellar system. When the collapse has been triggered, the pressure force becomes small compare to gravitational force, and the timescales of such collapses are on the order of the free-fall time, which is about 10^5 years (Bate et al., 2003).

The collapse does not form spherical protostar(s) directly. The reason is that most of the cores have considerable angular momentum, with angular velocities of about $10^{-14}-10^{-13} rad/s$ (Mejia, 2004). While angular momentum is almost conserved during free-fall, the size of the object shrinks dramatically in the collapse (form several pc to $\sim 10^3 AU$), hence, the centrifugal force becomes increasingly significant due to the increasing spin rate, which finally leads to formation of an accretion disk around the protostar.

At the early stage of star formation, the protostellar disk is embedded in a massive envelope with gas continuously accreting onto it. Meanwhile, angular momentum can be carried away by bi-polar jets due to magneto-hydrodynamic processes (Konigl & Pudritz, 2000), or redistributed by gravitational torques or turbulence (Yorke & Bodenheimer, 1999). These mechanisms lead to the accretion of disk material into the protostar. Disks can also be dispersed by stellar encounters, stellar winds, photoevaporation and planet formation

(See the review by Hollenbach et al. (2000) and Mejia (2004) for details). Generally speaking, the timescale of forming the disk (the free-fall time) is much shorter than the timescale of disk dispersal. Therefore, after a short but rapid growth phase, the disk mass decreases during most if its lifetime until it finally disappears.

Early observations of protostellar disks generally focused on the infrared excesses in the spectral energy distributions (SED)(Adams et al., 1988). The spectrum of radiation of a star itself is close to a Plank function. However, when a protostellar disk exists, the disk produces a spectrum peaking in IR, because the disk is much cooler. The observed SED, which is sum of the star and disk SED, thus naturally has an excess at IR or even longer wavelengths. Using this method, many young stellar objects have been found to have disks. More recently, with the advantage of adaptive optics or the Hubble Space Telescope, direct imaging has become another major tool for disk discovery, as shown in Figure 1.2 (Padgett et al., 1999; McCaughrean et al., 2000).

Most of the observed disks have masses $\leq 0.1 M_{\odot}$, sizes of about a few hundred AU ($\sim 150 - 200 AU$; Mejia (2004)), and correspond to a late stage of disk evolution. As for earlier protostellar disks, although it is clear that they would be larger and more massive than late ones, the disk outer radius and its mass are hard to observe since they are embedded in the envelope. Observations of CO and isotopic CO emissions find that the disk size is approximately 500 AU to several thousand AU and the total mass of disk and envelope is several tenths of a solar mass. The mass of the disk itself, however, is not well determined (Mundy et al., 2000) since it is difficult to find

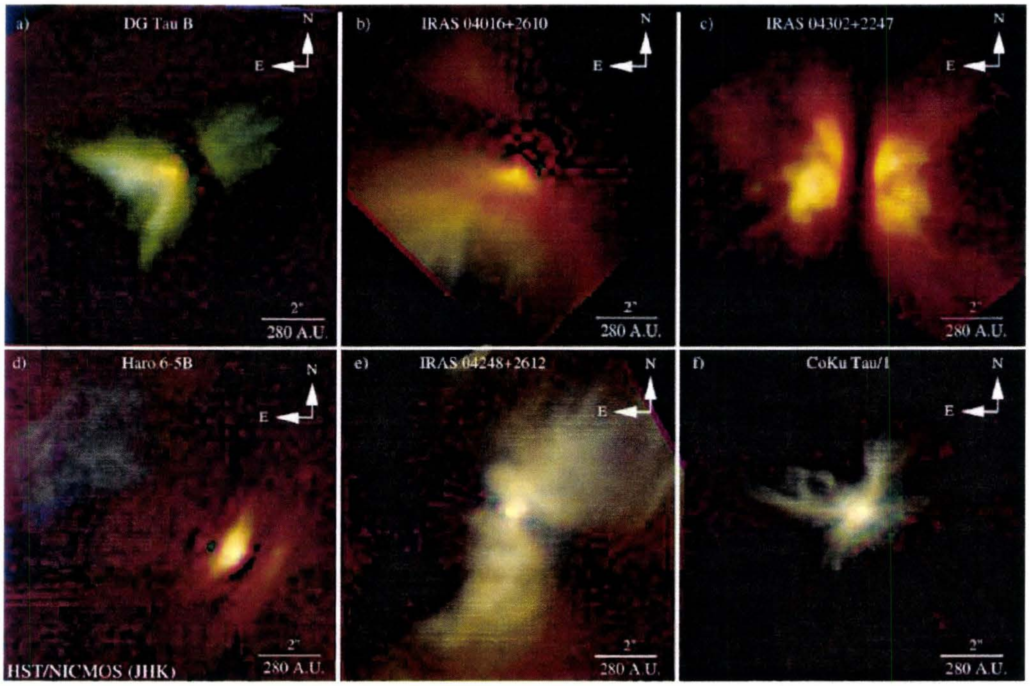

Figure 1.2 Images of disks around Taurus young stellar objects from *Hubble Space Telescope*.The scale appeared on each panel is 280 AU. Adapted from Padgett et al. (1999).

the boundary between the envelope and disk. Nevertheless, some numerical simulations of disk evolution have suggested that early disks that extend to over $\sim 10^3$ AU could be as massive as the protostar (Yorke & Bodenheimer, 1999; Lin & Pringle, 1990). As will be discussed in later sections of this thesis, the encounter probability is much higher for extended disks and therefore, I will concentrate on early stage of disks when the disk model is constructed in this study.

1.3.2 Structure of Protostellar Disk

After the initial rapid collapse stage, the dominant gas motion is close to Keplerian rotation in the disk plane (e.g. DM Tau in Guilloteau & Dutrey (1998)) and vertically the gas is nearly in hydrostatic equilibrium. The gas distribution can be approximately described in cylindrical coordinates as:

$$\rho(r, z) \sim \rho_0(r) exp(-z/H(r)). \tag{1.3}$$

Here H(r) is the disk scale height, which characterizes the thickness of the disk, and ρ_0 is the density in disk midplane. The integration of volume density $\rho(r, z)$ along vertical direction gives the surface density, $\Sigma(r)$, which can be described equivalently using scale height $H(r)$ as:

$$\Sigma(r) \sim 2\rho_0(r)H(r). \tag{1.4}$$

The radial surface density distribution is strongly influenced by the angular momentum transportation inside the disk and the interactions between disks. Theoretically, a power-law model is usually adopted for an isolated disk: $\Sigma(r) \propto r^p$ where p is between the range -0.75 to -1.5 for a standard model (Shakura & Sunyaev, 1973). However, the surface density is not well determined by observations, except for the direct imaging of silhouette disks, whose surface density profiles are best fitted by exponential functions and have a sharp truncated outer edge. This could be explained as a result of repeated encounters of disks which has originally power law distributions (Hall, 1997).

The scale height of the disk is also related to the radius. Assuming that the vertical scale, H, is much less than size of the disk, a back-of-the-envelope calculation of the vertical hydrostatic equation would give (Frank,King & Raine , 2002):

$$H(r) \simeq c_s \sqrt{\frac{r}{GM}} r. \tag{1.5}$$

It can be seen that from the above equation that the disk thickness is increasing with the radius — the disk is flared. As shown in Figure 1.3, when the disk is flared, the outer disk can receive radiation from the central object directly, and re-radiate more energy. This results in a greater excess at long wavelengths in the observed spectral energy distribution, as shown in Figure 1.4. According to the study by Chiang & Goldreich (1997), the SED produced by flared disks is consistent with observations (see Figure 8 in Chiang & Goldreich (1997) for details). The flared structure of the disk will be more obvious for an earlier disk since it is larger than the later ones. The finite scale height of the disk also affects disk stability. Modeling the disk correctly in the vertical direction is important in simulating the interaction and fragmentation of disks.

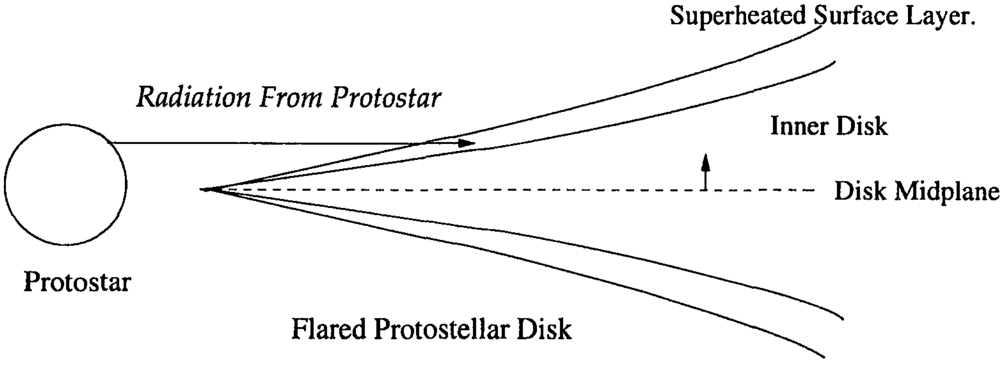

Figure 1.3 Geometry of a flared disk and its effect on radiative transfer. Radiation from the central object hits the surface layer due to the flared structure of the disk. The dust in the surface layer is superheated and the energy is re-emitted, which contributes to the IR excess in the SED.

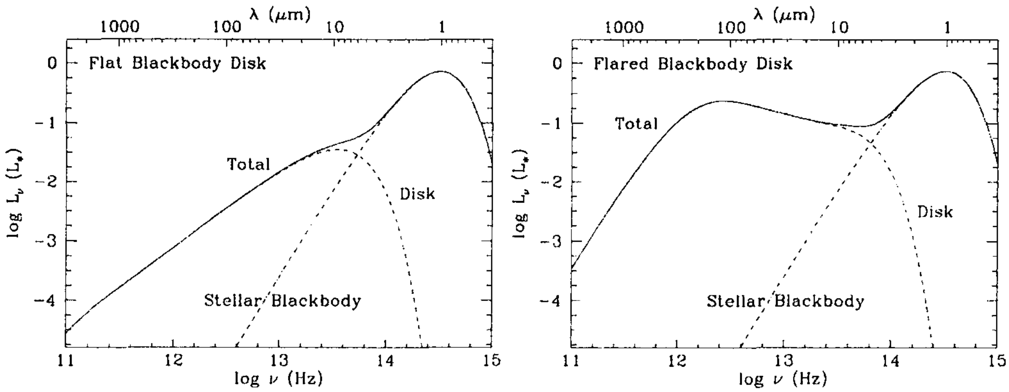

Figure 1.4 The difference in SED between flat and flared disks. The total luminosity is higher for a flared disk (right panel) than the flat one (left panel) due to the re-emission of superheated dust layer. Adapted from Chiang & Goldreich (1997), Figure 1 and Figure 2

1.3.3 Gravitational Instability and Fragmentation of Disks

In a protostellar disk, the gravitational force on gas is balanced by the thermal pressure, which describes the random motion of the gas, and the centrifugal force due to the rotation, so direct collapse is prevented. However, the balance does not exist for all kinds of perturbations. In some cases, small perturbations can grow exponentially, break the balance and thus develop into strong instabilities of the disk, referred to as gravitational instabilities. An unstable disk usually develops clear spiral arms, which assist the redistribution of angular momentum in the disk and the accretion of matter onto the protostar. Under certain circumstances, the density contrast of spiral arms can be amplified and eventually fragmentation can happen in the spirals and result in clumps with a small fraction of the original disk mass. Hence, gravitational instability of protostellar disks is a possible scenario for substellar object formation.

The condition for disk instability was first explored by Toomre (1964), who analyzed the stability of gaseous and stellar galactic disks under axisymmetric perturbations. By linearizing the fluid dynamical mass conservation equation, the Euler equation, the Poisson equation of gravity and the equation of state to the first order of the perturbation term, Toomre (1964) gives a parameter which characterizes the local stability of a two-dimensional thin disk defined as:

$$Q \equiv \frac{c_s \kappa}{\pi G \Sigma}. \tag{1.6}$$

In the above definition, c_s is the local sound speed, κ is the epicyclic frequency of the disk, which in a Keplerian disk is equal to the circular frequency

$\Omega \equiv v_\phi/r$, where v_ϕ is the magnitude of velocity in the tangential direction, G is Newton's gravitational constant and Σ is the surface density. In Toomre (1964), the critical value of Q is 1— that is to say, if local Q is below unity , the disk is locally unstable to a axisymmetric perturbations. $Q_{crit} > 1$ is called Toomre's stability criterion. The origin of this criterion can be seen from the definition of Q : since c_s describes the thermal motion of gas and κ characterizes the rotation of the disk, the product of c_s and κ in the definition is because neither thermal pressure nor rotation alone can stabilize the disk from gravitational instability, but the combination of the two can. Also, more massive disks are more likely to be unstable compared to lighter ones with similar temperature and rotation velocity since surface density appears in the denominator of the disk. For stellar disks, the definition of Q is slightly different from the one for gaseous disks in Equation 1.6, but the critical value of Q is also 1.

Note that the Toomre's criterion only determines if the disk will undergo gravitational instability, but instability does not neccessarily leads to fragmentation. It could only result in the development of spiral structure in the disk. Moreover, the criterion is calculated locally and applies for axisymmetric perturbations. The global stability criterion of disk fragmentation under axisymmetric or non-axisymmertic perturbation is hard to calculate analytically. However, modern numerical simulations of fragmentation of both galactic disks (Kim & Ostriker, 2001) and late-stage protostellar disks (Mayer et al., 2004) all show that Toomre Q parameter can still serve as a good indicator of the global behavior of the disks under non-axisymmeric perturbations, and the critical value for the disks for fragmentation is also close to unity. For example, Mayer et al. (2004) gives $Q_{crit} \sim 1.4$ for a thin protostellar disk to fragment under non-axisymmetric perturbations.

Although most of simulations deal with gravitational instability of two dimensional disks, in reality, disks have finite thickness. Especially, for an early, extensive protostellar disk, the scale height increases with disk radius roughly as $r^{3/2}$, so the outer part of the disk is very thick. Finite thickness affects the stability of the disk. In the work by Kim et al. (2002), the critical value Q for a disk to fragment was lowered from 1.3 (for a razor thin disk) to 0.75 when the finite thickness was taken into account, i.e., the disk was stabilized by finite thickness. Therefore, in reality the disk will be more stable than two-dimensional approximated disks.

Thermal regulation is very important to disk fragmentation even when the disk's Toomre Q is below the critical value. To fragment, the disk cooling time must be comparable to the dynamical time (Rice et al., 2003; Gammie, 2001). For an isolated protostellar or protoplanetary disk, gravitational instability may play an important role in star accretion (Yorke & Bodenheimer, 1999), but whether or not fragmentation can take place is determined by the cooling rate. For example, Rafikov (2005) found that fragmentation was unlikely to happen in a protoplanetary disk, assuming the disk was cooled by simple radiative transfer. However, in a dynamic environment it could be a different situation: interaction between disks would cause expansion of a disk and dynamically cool it, while shocking by physical impact may compress the gas to higher density and heat it. If cooling is effective and the cooling time is still comparable to dynamical timescale of the disk, fragmentation may happen and the clump may survive.

In both isolated or in dynamical interactions, it is expected that the Toomre Q will be an important parameter for the instability of protostellar disks, since Q is based on universal disk properties. The dependence of instability and fragmentation of early protostellar disks on Q, however, has not been thoroughly explored; especially when the effect of finite thickness is significant and when dynamical interaction between disks is present. This dependence is crucial to verifying the correct scenario of formation of substellar objects from protostellar disks. Therefore, the relationship between Q and the probability of fragmentation is one of the major investigations reported in the present work.

1.3.4 Disk Encounters in Dynamical Star Formation

The previous introductory sections concentrated on the formation and properties of protostellar disks which neglected interactions with other disks or stars. In reality, observations show that the major mode of star formation is clustered instead of isolated formation (Clarke et al., 2000). The cluster can be as large as bound groups containing more than a thousand stars or small ones which only have a few tens of stars. Some stellar clusters are embedded in molecular gas and can only be observed at infrared or longer wavelengths which indicates that they are very young and still undergoing the formation process. Observations of embedded and non-embedded clusters show various stellar densities. For example, the number density of stars in the Trapezium cluster is $10^4\ pc^{-3}$, while in the star forming region of L1630 in Orion B and the L1688 region of ρ Ophiuchi stellar density are of order $10^2\ pc^{-3}$ (Stahler & Palla , 2004). The velocity dispersions of clusters are of order a few km/s.

The origin and initial triggering of cluster formation is still a matter of debate. It is suggested that the initiators of cluster formation can be turbulence, self-gravity, and agglomeration with fragmentation (Elmegreen et al. (2000) and references therein). Many numerical simulations have also been done to address this question, and have shown that collapse and fragmentation of a turbulent molecular cloud can result in formation of a small cluster. In the work by Bate et al. (2003), the observed mass distribution is also reproduced down to the substellar regime. Moreover, at an early stage of formation, the original angular momentum of cloud leads to formation of multiple disks at the same time (Whitworth et al., 1995; Bate et al., 2003), which interact with each other dynamically in further evolution.

1.3.4.1 Disk Encounter Rates in Clusters

When extended disks coexist in young stellar clusters, the probability of a physical encounter is high. Watkins et al. (1998a) found from their studies that there is, on average, at least one encounter during a disk's lifetime. This is consistent with the similarity of the encounter and disk lifetimes. The timescale between encounters is defined as

$$t_{SE} \equiv \frac{1}{n_* \sigma v}. \tag{1.7}$$

Here n_* is the number density of protostars with disks, v is the velocity dispersion of the protostars, and σ is the encounter cross section. Adopting the cross section calculation from Hollenbach et al. (2000), gives

$$\sigma = \pi(3r_d)^2, \tag{1.8}$$

where r_d is the radius of the star. Rewriting equation 1.7 in terms of typical values of r_d ,n and v results in

$$t_{SE} \simeq 2 \times 10^5 year \left(\frac{n_*}{10^4 pc^{-3}}\right)^{-1} \left(\frac{v}{1km/s}\right)^{-1} \left(\frac{r_d}{1000AU}\right)^{-2}. \tag{1.9}$$

For an extended disk with radius ~ 1000 AU, a stellar density as high as the Trapezium cluster results in an encounter timescale of about 10^5 years. Although the typical disk lifetime is about 10^7 *years*, the lifetime of the extensive stage is much shorter–around 10^5 years (Yorke & Bodenheimer, 1999), comparable to the encounter timescale. In dense clusters, each disk will have at least one chance to encounter another disk. For low density clusters like the ones in region L1630, the rate is lower, but still possible, especially when the relative velocity between two disks is small and gravitational focusing is taking place.

1.3.4.2 Effect of Disk Encounters in Star and Substellar Object Formation

Disk encounter studies (sometimes including star-disk encounters) suggest that there is a non-negligible interaction rate of protostellar disks in clusters and such encounters make dynamical star formation different than quiescent formation in several ways. First, significant material can be stripped from the disk, which shortens the lifetime, steepens the surface density profile of the disk (McCaughrean & O'dell, 1996) and subsequently affects the course of accretion and planet formation. Second, the dissipation of energy in encounters may result in the capture of protostars and formation of binaries (Larson, 1990) with circumbinary disks. A third effect is that non-coplanar prograde encounters can twist the disk and generate tidal filamentary structures (Clarke & Pringle, 1993; Lin et al., 1998), where clumps may condense out and remain low mass as suggested in the work by Lin et al. (1998). Last, but not least, dynamical encounters may trigger the gravitational instability and fragmentation of a stable disk (Watkins et al., 1998a). Fragments forming from the last two processes tend to have substellar mass. The reason is that, compared to the molecular cloud, the density of the disk is much higher, and the Jeans Mass is lowered by several orders of magnitude. However, the clumps may migrate into inner dense parts of the disk and enhance the accretion of gas onto them. The interaction between close clumps, on the other hand, can cause the ejection of them out of the dense gaseous region and stop the accretion (Reipurth & Clarke, 2001). If the accretion rate is high enough, multiple stellar system may form (Watkins et al., 1998a). If not, substellar objects may form as either companions of stars or as free-floating objects.

The effects of a protostellar disk encounter could be different for different dynamical parameters. For instance, tidal tail structures could form in perpendicular encounters (Lin et al., 1998) while shock layer fragmentation could occur in coplanar encounters (Watkins et al., 1998a); the alignment of disk spin and orbit angular momentum could result in material dragging and spiral formation in the disk (Clarke & Pringle, 1993), while spin-orbit anti-alignment could produce severe dissipation of gas (Boffin et al., 1998). Pure tidal interaction between two disks could be very different than physical impact.

It is obvious from the array of possible outcomes described above that correctly modeling disk encounters in clusters is important to understanding observed disk shapes and lifetimes, formation of multiple stellar systems, and the formation of substellar objects and their mass distribution. Numerical simulations are essential here because of the non-linear nature of strong interactions. As demonstrated below, close attention should always be paid when simulating fragmentation because fragments can be artificially formed or destroyed as a result of numerical effects. In this work, I will concentrate on the instability and fragmentation developed during the physical impact of two extended stable disks, and the properties of fragments.

1.4 Numerical Modeling of Disk Encounters

There are three key requirements for numerically modeling encounters and fragmentation of protostellar disks:

1. Correctly model flared-disk structures to prevent artificial instability caused by the unresolved scale height.

2. Provide enough resolution to resolve the Jeans length (or Jeans mass), otherwise the fragmentation may depend on implementation of the numerical methods (Bate & Burkert , 1997).

3. Reasonably approximate the thermal conditions during the encounter, especially when heating by shocks is present and when the densities of the clumps reach the opacity limit.

The importance of the first condition is apparent from the discussion of disk structures. Previous work mostly dealt with two dimensional disks. Although fragmentation did happen in simulations, it was not necessarily related to the instability criterion of real disks. In this study, much effort will be put into constructing a more realistic model, including the effect of scale height, as well as exploring the instability criterion in dynamic environments.

Resolution is always important in numerical simulations, and an unresolved Jeans Mass is one of the biggest dangers in a numerical study of fragmentation (Bate & Burkert , 1997). Moreover, the Jeans Mass changes with local density, so whether or not it can be resolved *during* the fragmentation also matters. As demonstrated in the following chapters, artificial fragmentation happens when the resolution is too low. Most of previous work did not resolve the Jeans Mass because of limited computer resources several years ago. The work reported in the current study resolves the Jeans Mass until a late stage of fragmentation.

Efficient cooling is required for fragmentation via gravitational instability. In reality, gas in initial disks can be well approximated as locally isothermal, i.e., the temperature of the gas is determined solely by its distance from the star due to the strong influence of disk geometry on cooling rate. However, when fragmentation happens, the rapid rise of density makes the gas optically thick and the cooling rate by radiation is lowered. Secondary fragmentation inside the clump may therefore be prevented (Bate et al., 2003). The temperature in the clump rises quickly until the dissociation temperature is reached. The situation may be even more complicated when shocks occur due to the impact heating of the gas. Numerically, the ideal way to model this is to apply full radiative transfer in the simulation. Simple approximations of thermal conditions are currently used because of the difficulty in incorporating numerical radiative transfer. Isothermal and adiabatic conditions are two common approximations. The appropriateness of each of these choices can be verified by examining the cooling and heating rates.

1.5 Prior Work and Outline of This Work

Several studies have been undertaken on the topic of disk encounters. Most of the early works concentrated on disk truncation (Hall, 1997) or binary formation (Clarke & Pringle, 1993), but not disk fragmentation. Relatively recent work by Lin et al. (1998) and Watkins et al. (1998a) emphasized formation of substellar objects via disk fragmentation in encounters. The basic result of Watkins et al. (1998a) is that dynamical encounters can trigger fragmentation inside stable disks and the formation of substellar objects. The main result of Lin et al. (1998) is that filamentary structures induced by disk interactions can condense and form substellar mass clumps. Both studies used flat disk models and did not resolve (or only marginally resolved) the Jeans Mass. As a result, the fragments could be artificial. To date, there are no explorations in the roles of stability criteria of the disk. The resultant clumps were not well resolved in previous work, either. In the meantime, rapid observational developments have revealed more properties of substellar objects and these observations constrain theories of their formation. In this work I will present a numerical study of disk-disk encounters and the ensuing fragmentation using realistic disk models at much higher resolution. A large encounter parameter space will be explored, including the stability property of initial disks, the relative configuration of the two disks and the disk velocities. Analysis of resultant clumps, including the mass distribution, angular momentum and orbits, will be presented and compared to the observational data.

The structure of the thesis is as follows: Chapter 2 will introduce the methodology of the study, mainly consists of the numerical methods of simulations, the disk modeling and the construction of initial conditions. Chapter 3 will describe the main results of a series of simulations designed for exploring the encounter parameter space. Test simulations with different resolution and disk models will also be presented for comparison with other work. The results and their observational implications will be discussed in Chapter 4. Finally, Chapter 5 will summarize the study and give conclusions.

Bibliography

Adams, F. C., Shu, F. H., & Lada, C. J. 1988, ApJ, 326, 865

Bate, M. R., Bonnell, I. A., & Bromm, V. 2002, MNRAS, 332, L65

Bate, M. R., Bonnell, I. A., & Bromm, V. 2003, MNRAS, 339, 577

Bate, M. R., & Burkert, A. 1997, MNRAS, 288, 1060

Boffin, H. M. J., Watkins, S. J., Bhattal, A. S., Francis, N., & Whitworth, A. P. 1998, MNRAS, 300, 1189

Boss, A. P. 2001, ApJ, 563, 367

Chiang, E. I., & Goldreich, P. 1997, ApJ, 490, 368

Clarke, C. J., & Pringle, J. E. 1993, MNRAS, 261, 190

Clarke, C. J., Bonnell, I. A., & Hillenbrand, L. A. 2000, Protostars and Planets IV, 151

Elmegreen, B. G. 1999, ApJ, 522, 915

Elmegreen, B. G., Efremov, Y., Pudritz, R. E., & Zinnecker, H. 2000, Protostars and Planets IV, 179

Frank, J., King, A., & Raine, D. *Accretion Power in Astrophysics*, Third Edition, Cambridge University Press 2002

Gammie, C. F. 2001, ApJ, 553, 174

Guilloteau, S., & Dutrey, A. 1998, A&A, 339, 467

Halbwachs, J. L., Arenou, F., Mayor, M., Udry, S., & Queloz, D. 2000, A&A, 355, 581

Hall, S. M. 1997, MNRAS, 287, 148

Hambly, N. C., Hodgkin, S. T., Cossburn, M. R., & Jameson, R. F. 1999, MNRAS, 303, 835

Hollenbach, D. J., Yorke, H. W., & Johnstone, D. 2000, Protostars and Planets IV, 401

Kim, W.-T., & Ostriker, E. C. 2001, ApJ, 559, 70

Kim, W.-T., Ostriker, E. C., & Stone, J. M. 2002, ApJ, 581, 1080

Konigl, A., & Pudritz, R. E. 2000, Protostars and Planets IV, 759

Larson, R. B. 1990, ASSL Vol. 162: Physical Processes in Fragmentation and Star Formation, 389

Lin, D. N. C., Laughlin, G., Bodenheimer, P., & Rozyczka, M. 1998, Science, 281, 2025

Lin, D. N. C., & Pringle, J. E. 1990, ApJ, 358, 515

Luhman, K. L., Rieke, G. H., Briceno, C., Liebert, J., & Hartmann, L. 1998, ASP Conf. Ser. 154: Cool Stars, Stellar Systems, and the Sun, 154, 1887

Marcy, G. W., & Butler, R. P. 1998, ARA&A, 36, 57

Marcy, G. W., & Butler, R. P. 2000, PASP, 112, 137

Marcy, G. W., Cochran, W. D. & Mayor, M. in *Protostars and Planets IV*, Wanninggs,V., Boss, A. P., Russell, S. S., Eds., 2000, pp.1285-1311

Mayer, L., Wadsley, J., Quinn, T., & Stadel, J. 2004, ASP Conf. Ser. 321: Extrasolar Planets: Today and Tomorrow, 321, 290

Mayor, M., Queloz, D., & Udry, S. 1998, ASP Conf. Ser. 134: Brown Dwarfs and Extrasolar Planets, 134, 140

McCaughrean, M. J., Stapelfeldt, K. R., & Close, L. M. 2000, Protostars and Planets IV, 485

McCaughrean, M. J., & O'dell, C. R. 1996, AJ, 111, 1977

Mejia, A. C. 2004, Ph.D. Thesis,

Muench, A. A., Alves, J., Lada,C. J., and Lada, E. A. 2001, ApJ, 558, L51

Mundy, L. G., Looney, L. W., & Welch, W. J. 2000, Protostars and Planets IV, 355

Oppenheimer, B. R., Kulkarni, S. R. and Stauffer, J. R., in *Protostars and Planets IV*, Wanninggs,V., Boss, A. P., Russell, S. S., Eds., 2000, pp.1313-1338

Padgett, D. L., Brandner, W., Stapelfeldt, K. R., Strom, S. E., Terebey, S., & Koerner, D. 1999, AJ, 117, 1490

Padoan, P., & Nordlund, Å. 2004, ApJ, 617, 559

Perri, F., & Cameron, A. G. W. 1974, Icarus, 22, 416

Pickett, B. K., Mejía, A. C., Durisen, R. H., Cassen, P. M., Berry, D. K., & Link, R. P. 2003, ApJ, 590, 1060

Reipurth, B., & Clarke, C. 2001, AJ, 122, 432

Rice, W. K. M., Armitage, P. J., Bate, M. R., & Bonnell, I. A. 2003, MNRAS, 339, 1025

Shakura, N. I., & Sunyaev, R. A. 1973, IAU Symp. 55: X- and Gamma-Ray Astronomy, 55, 155

Stahler, S. W., & Palla, F. 2004, *The Formation of Stars* (2004 WILEY-VCH Verlag GmbH & Co. KGaA, Weinheim)

Toomre, A. 1964, ApJ, 139, 1217

Rafikov, R. R. 2005, ApJ, 621, L69

Watkins, S. J., Bhattal, A. S., Boffin, H. M. J., Francis, N., & Whitworth, A. P. 1998, MNRAS, 300, 1205

Whitworth, A. P., Chapman, S. J., Bhattal, A. S., Disney, M. J., Pongracic, H., & Turner, J. A. 1995, MNRAS, 277, 727

Yorke, H. W., & Bodenheimer, P. 1999, ApJ, 525, 330

Chapter 2

Methodology

2.1 Overview

In protostellar disk encounters, gravity is the driving force because the disks are very massive. Pressure also plays an important part since the disks are gaseous. A successful simulation must correctly calculate both forces. In this study I used the TreeSPH code GASOLINE (Wadsley et al., 2004) to simulate the encounter of two protostellar disks. The code implements tree algorithms to calculate gravity and Smoothed Particle Hydrodynamics (SPH) for gas dynamics. It is designed as a parallel code and scales well for up to 60 processors. Also, the code uses the multiple timestep technique to cover a large range of timescales in astrophysical problems, especially in fragmentation studies. The first part of this chapter gives a general introduction to both Tree and SPH methods and then briefly describe their implementation in GASOLINE.

Other important parts of the simulation are the model description and construction of protostellar disks: temperature and density profile, Q parameters, disk scale height, self gravity of gas, and velocity profiles of gas all have effects on the simulation results and obviously not all parameters listed are independent of each other. Generating a self-consistent model for the disk is essential. In the second part of this chapter, I present my choice of radial profiles of disk surface density and temperature, the construction of the vertical structure using the hydrostatic equilibrium condition, and the calculation of an initial velocity field which takes into account the disk's self-gravity. Finally, in the third part of the chapter, I describe the parameter space I explored and equation of state (EOS) I chose for simulating the encounters.

2.2 Numerical Methods for Simulating Protostellar Disk Encounters

2.2.1 Gravity

Simulation of astrophysical processes should always deal properly with the gravitational force. For discrete astronomical objects, when relativistic effects are not significant, the acceleration due to gravity of a certain object, labelled i, due to other objects, labelled j, is:

$$\vec{a_i} = \sum_{j \neq i} \frac{GM_j(\vec{r_i} - \vec{r_j})}{|\vec{r_i} - \vec{r_j}|^3}, \tag{2.1}$$

where G is Newton's gravitational constant, and $\vec{r}$ is the position of the object. Early N-body simulations usually calculated $\vec{a_i}$ directly from Equation 2.1. If there are N objects in the simulation, the total work for the direct approach is $\mathcal{O}(N^2)$. When the number of objects becomes large, which is the situation in modern astrophysical simulations, this approach is impractical. Therefore, many algorithms have been developed to reduce the order of the calculation. Among these are Particle-Mesh (PM) and Particle-Particle Particle-Mesh (P^3M), both of order $\mathcal{O}(N \log N)$ using Fast Fourier Transform (FFT).

The Hierarchical Tree method, first developed by Barnes & Hut (1986), is another widely-adopted algorithm. The idea is to express the gravitational potential using multipole expansion, and the higher multipoles fall off faster with distance than the monopole does. Thus the detailed distribution of remote masses is not as important as closer ones. A tree structure can be built by dividing the simulation box down to the scale that contains a certain small number of particles, with the root node corresponding to the whole box and every subsequent tree level corresponding to the scale after one division. When calculating forces for the closest set of objects (objects contained in the same box) the direct calculation in Equation 2.1 is applied. For remote objects, the gravitational potential is approximated by the first few terms of the multipole expansion without losing required accuracy. Since both tree building and force calculation are of order $\mathcal{O}(N \log N)$, the method dramatically lowers the computational costs of the calculation relative to direct approach. Compared to most grid-based algorithms, the Tree method has the advantage when dealing with clustered objects and so it is very appropriate for the study of fragmentation.

2.2.2 Gas

Most astrophysical objects are composed of highly-compressible gas, so it is also essential to include gas dynamics in calculations. There are two fundamentally different classes of methods in numerical gas dynamics: Eulerian and Lagrangian methods. In Eulerian methods, fluid properties such as density and pressure are obtained as functions of time at fixed positions in space and so it is suitable to use a fixed-mesh-based algorithm such as a finite difference or a finite element approach to solve the equations numerically. Since the methods are grid-based, the resolution is determined by the size of the grid but not the mass distribution. To resolve the fragmentation during simulations, the grid size needs to be very small for the whole simulation box. Therefore, it is very expensive to simulate fragmentation with Eulerian methods. Lagrangian methods, on the other hand, solve the fluid properties in a co-moving reference frame following the fluid flow and, because of this, the resolution follows the mass. For simulating fragmentation, where large scale density variation is present, Lagrangian methods are much less computationally expensive than Eulerian methods. Particle-based Lagrangian methods also have better performance in modeling rapidly rotating disks because they explicitly conserve angular momentum (Wadsley et al., 2004). In this study, a Lagrangian method is used in order to better model the protostellar disks and resolve smaller fragments.

Smooth Particle Hydrodynamics (SPH) is a popular Lagrangian particle method in astrophysical simulations. It was first developed by Lucy (1977) and Gingold & Monaghan (1977). The principle of the SPH method is to represent a continuous fluid field with a set of disordered discrete particles, and interpolate values at any point with a kernel function W. For example, the density at position $\vec{r}$ can be represented as a weighted summation of all discrete masses (Monaghan, 1992),

$$\rho(\vec{r}) = \sum_i m_i W(\vec{r} - \vec{r}_i, h). \tag{2.2}$$

W is a smooth function with properties:

$$\int W(\vec{r} - \vec{r'}, h) d\vec{r'} = 1, \tag{2.3}$$

and

$$\lim_{h \to 0} W(\vec{r} - \vec{r'}, h) = \delta(\vec{r} - \vec{r'}). \tag{2.4}$$

Here, h describes the characteristic length over which W falls off quickly and is called the smoothing length. In simulations, h can be different for different particles depending on their local spacing. The immediate advantage of SPH is that all spatial derivatives can be represented by derivatives of the kernel function, and as a result, all the partial differential equations in fluid mechanics become ordinary differential equations (Monaghan, 1992). This greatly simplifies numerical calculations in fluid dynamics. SPH is designed from first principles without introducing any grid. Therefore, it is very suitable to use SPH to simulate free-boundary and non-axisymmetric astrophysical processes.

2.2.3 Tree +SPH parallel code: GASOLINE

The SPH method is a natural ally of N-body gravity methods because both are particle based. GASOLINE is a parallel implementation which combines Tree gravity calculations with Smooth Particle Hydrodynamics. It was developed by Wadsley et al. (2004) and has been successfully used in various astrophysical simulations including simulations of cosmology, galaxy formation and planet formation. In this work I used GASOLINE to simulate protostellar disk encounters, so it is necessary to give a brief description of the code.

GASOLINE uses an $\mathcal{O}(N \log N)$ Tree algorithm to calculate the gravity between particles. Unlike the original method developed by Barnes & Hut (1986), it uses a spatial binary tree to represent the hierarchical mass distribution in order to reduce parallel communication. Construction of the tree is done by dividing the entire simulating box into smaller regions (nodes) until the leaf nodes are reached, within which there are only 8-10 particles. A leaf node is called a bucket. In the force calculation stage, for a certain particle i, forces by other particles in the same bucket B_i are calculated directly using Equation 2.1. For other buckets or upper nodes, an opening radius r_{open} originating in the center of mass of B_i is used as a criterion. Any buckets or nodes which do not intersect with r_{open} are not open, and forces are calculated approximately; otherwise, the nodes are considered to be open. For any nodes which are open, the intersection test is repeated on the children of those nodes until their leaf buckets are reached. All of the particles in the buckets are considered to be interacting directly with particle i.

Gravity-softening is used in GASOLINE in order to mimic a smooth distribution of gas and reduce the number of small-timestep calculations. A spline form similar to that implemented in the SPH kernel function is employed in softening the gravity and a softening length ϵ is defined such that when two particles i, j are more distant from each other than $\epsilon_i + \epsilon_j$, the interaction between them reverts to $1/r^2$.

The SPH method used in GASOLINE is a Lagrangian method, and therefore the advection terms in the fluid dynamic equation are implicit. After proper smoothing, density at any position i can be obtained immediately from Equation 2.2. The momentum equations and energy equations are (Wadsley et al., 2004)

$$\frac{d\vec{v_i}}{dt} = -\sum_{j=1}^{n} m_j(\frac{P_i}{\rho_i^2} + \frac{P_j}{\rho_j^2} + \Pi_{ij})\nabla_i W_{ij} \tag{2.5}$$

and

$$\frac{du_i}{dt} = \frac{P_i}{\rho_i^2}\sum_{j=1}^{n} m_j \vec{v_{ij}} \cdot \nabla_i W_{ij}, \tag{2.6}$$

where W_{ij}, v_i, u_i, ρ_i, P_i are the kernel function, velocity, internal energy, density, and pressure of particle i, respectively. The same symbols apply for particle j. Π_{ij} is the artificial viscosity term used to model entropy generation in shocks and to prevent unphysical interpretation of gas flows (Wadsley et al., 2004). Note that the original partial differential equations in gas dynamics have been converted to ordinary differential equations in time. From Equation 2.5 and Equation 2.6, the fluid quantities for every particles can be updated by simple integration.

To conserve energy and momentum during calculations, GASOLINE uses a symmetric smoothing kernel so that $W_{ij} = W_{ji}$

$$W_{ij} = \frac{1}{2}w(|\vec{r_i} - \vec{r_j}|/h_i) + \frac{1}{2}w(|\vec{r_i} - \vec{r_j}|/h_j), \tag{2.7}$$

where h_i and h_j are the smoothing lengths for particle i and j and $w(x)$ is a spline function defined by Monaghan (1992) which decreases to 0 when $x > 2$.

For a given particle i, smoothing is only performed over neighbor particles within $2h_i$, and neighbor-finding is essential for SPH calculations. The tree constructed to calculate gravitational forces can therefore be used to locate neighbors. This is very efficient because it is of order $\mathcal{O}(N \log N)$.

Radiative cooling exists in most astrophysical processes. Heating is also common as a result of release of gravitational energy, shocks of supersonic gas, and/or star formation feedback. GASOLINE incorporates star formation feedback and various cooling functions including isothermal, adiabatic, implicit energy integration, and hydrogen and helium cooling processes (Wadsley et al., 2004). The modular design of the cooling code makes it easier to modify or add new cooling functions without changing the main structure of the code. In this study, a local isothermal cooling function, in which the gas temperature is a fixed function of its position, was implemented and added into the published version of GASOLINE.

The integration in GASOLINE uses multiple timesteps in order to cover a large timescale in astrophysical problem such as fragmentation. The localized calculation for both Tree gravity and SPH makes GASOLINE easy to parallelize, and the code performs well when using large number of processors.

For every specific problem, essential parameters such as force accuracy r_{open}, smoothing length h_i, gravitational softening ϵ_i, and viscosity parameters can be given by the user in a parameter file. For integration, the extent of timestep splitting can also be defined by the user. Simple forms of cooling functions, such as those used in this study, can be written as a module plug-in to the main program.

2.3 Initial Conditions

Early protostellar disks embedded in molecular envelopes are complex systems: gas from the disk is accreting onto the star as it loses angular momentum as a result of angular momentum transport while the envelope is collapsing onto the disk; the forming star(s) radiate onto the disk, affecting the disk temperature and shape, which in turn affect the stability of disk; the dust component of the disk may have a different temperature than the gas; magnetic fields are important in the inner disk and bipolar jets may exist in order to carry the angular momentum away. Unfortunately, simulation of the full system is beyond the ability of current computational hardware, and certain approximations or assumptions must be made according to the specific situation in the problem under study.

In this study, some reasonable simplifications were also made.

- First, the disks were extended to have outer radii around $1000 AU$ and masses comparable to the star. This was because, early stage protostellar disks are more extended than later ones and the encounter rate for early, large disks is much higher. Many observations of IRAS sources (Ohashi et al., 1997) and simulations of collapsing molecular clouds (Yorke & Bodenheimer, 1999; Lin & Pringle, 1990) have indicated that early protostellar disks can be as large as several thousand AU.

- Second, accretion caused by long-term processes, such as effective viscosity due to turbulence, was not modeled in these simulations. Since the disk is extended, the timescale for accretion due to effective viscosity is about 10^7 years (cf. Hollenbach et al. (2000) Figure 1), which is significantly longer than the dynamical interaction time of $\sim 10^5$ years. It therefore made sense to assume that long-term accretion does not have much of an effect on disk evolution during the dynamical timescale. However, accretion due to the dynamical interaction was simulated in this study, because it is much more rapid and very important in disk evolution.

- Third, envelopes around disks were not included in the disk models. In typical star formation scenarios, after the rapid collapse stage and the formation of protostellar disks, the densities of the envelopes are much smaller than that of the disks, though the envelopes may still have substantial masses from the molecular cloud cores. It was reasonable to assume that the disks do not grow during the encounter and to exclude the envelopes from the model.

- Bipolar jets and stellar winds may occur in the inner boundary of protostellar disks, and they are very important for the systems to lose their angular momentum. However, since they only occur within a few AU of the star (Najita et al., 2000), which is distant from the encountering outer disks (hundreds of AU away in this study), they were also not modeled.

- The mass fraction of dust in an early disk is very low so it cannot significantly change the molecular weight of the gas. Presence of dust may facilitate cooling, but even without dust the cooling is still efficient, because the optical depth of an early, extended disk is much less than 1.

Hence, it is a good approximation to exclude the dust component and use an efficient cooling function instead of calculating the dust properties and radiative transfer.

Given the simplifications above, the remaining task was to construct the model. As mentioned in section 1.3.2, the formation of disk is quasi-static and the vertical structure of the disk can be well approximated by hydrostatic equilibrium, so Equation 1.3 applies. Also, since the timescale for accretion in the initial disk is long, gas is also nearly in equilibrium radially. Hence, the rotational velocity of gas can be calculated using the balance between the gravitational forces from the star and the disk, the radial pressure gradient, and the centrifugal force due to rotation. Given these conditions, one need only specify the density profile, and the temperature profile, the mass for each star and disk to construct a self-consistent model.

2.3.1 Radial Profiles of Protostellar Disks

2.3.1.1 Surface Density Profile

In this study, the surface density followed a power-law profile $\Sigma(r) = \Sigma_0 r^p$, but the values of p were different in different regions of the disk: the disk within 80 AU was considered to be the inner disk and its density is artificially lowered in the initial condition. The purpose of this was mainly to avoid very small timesteps at the beginning of computations. Note that the physical processes in the region 1 $AU < R < 80$ AU was still be correctly modeled during the simulation. After a certain period of relaxation, the inner disk surface density increased quickly and its profile was nearly flat ($p = 0$), which is consistent with the observational surface density profile in the inner radius of early disk-envelope system (Andre et al., 2000).

The region from 80 to 500 AU was of primary importance because the majority of the disk mass resided in this region. Therefore this was the annulus within which fragmentation was most likely to occur. The surface density profile in this region was $\Sigma(r) = \Sigma_0 r^{-1.5}$. This profile was chosen to be consistent with the radial profiles obtained by the numerical calculation of protostellar disk formation in the work by Yorke & Bodenheimer (1999). The coefficient Σ_0 was calculated by setting the total disk mass $M_d = 0.5 M_\odot$ and letting $\int_{R_{in}}^{R_{out}} \Sigma(r) 2\pi r dr = M_d$.

Steeper density profiles were used at radii greater than 500 AU, which was consistent with some observations of disk outer radii (e.g., McCaughrean et al., 2000) and also ensured that most of the disk mass was inside 500 AU.There were two power laws used in the outer disk: $p = -5$ from 500-700 AU and a much steeper $p = -15.0$ from 700-1500 AU. To avoid strong numerical transitions, the boundary between any two different profiles was smoothed by linear interpolation in the logarithmic space. Figure 2.1 shows the surface density profile. As demonstrated in the figure, the surface density was very low (about 0.1 $g\ cm^{-2}$) at 1000 AU although the total calculation covered 1500 AU.

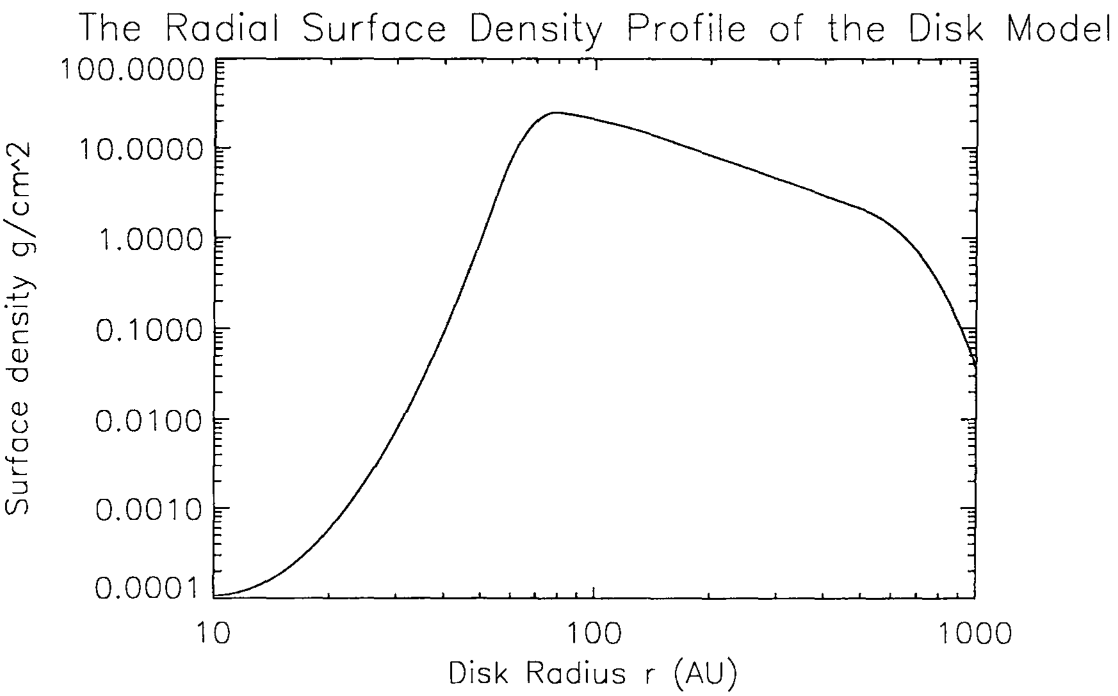

Figure 2.1 The logarithmic surface density profile for the initial protostellar disk. The powers used in region 0-10 AU, 80-500 AU, 500-700 AU and 700-1500 AU are 0, -1.5, -5, -15 respectively, the connections between different regions are smoothed and the region within 80 AU is truncated. The regions of $R < 10AU$ and $R > 1000AU$ are not plotted. The total mass of the disk is $0.6M_{\odot}$, corresponding to a very massive, early stage disk.

2.3.1.2 Temperature Profile

Previous disk encounter studies by Lin et al. (1998) and Watkins et al. (1998a) assumed that the disk initially has uniform temperature. This is not realistic if the radiation of central objects is taken into consideration. Assuming that the central objects has temperature T_* and radius R_*, and that the light hits the disk at angle α, the radiation flux received at a radius r where $r \gg R_*$ is $(\alpha/2)(R_*/r)^2\sigma T_*^4$. The flux emitted from the disk, assuming that the gas opacities are the same in all wavelengths, is of order $\sim \sigma T_d(r)^4$, where $T_d(r)$ is the effective temperature of the disk. Equating the two flux would give

$$T_d(r) \sim (\frac{\alpha}{2})^{1/4}(\frac{R_*}{r})^{1/2}T_* \propto r^{-1/2}. \tag{2.8}$$

Equation 2.8 shows that the temperature varies with radius as a power law function with power -0.5 at $r \gg R_*$. Obviously, it is a more realistic function than uniform temperature. This temperature profile has been used in other simulations of protoplanetary disk fragmentation (Mayer et al., 2004; Pickett et al., 2003). Therefore, it was also adopted in this study for disk radii within 500 AU. In the outer region (R > 500 AU) an ambient uniform temperature of around 10 K was used, which is a typical temperature in the envelope. Also, since the power-law temperature-radii relation with index -1/2 fails near the star and the inner disks were not realistically modeled, the temperature inside 10 AU was fixed with maximum T = 1000 K in order to prevent the divergence when $r \rightarrow 0$. Figure 2.2 shows a sample temperature profile.

The Toomre Q parameter, which is critical for characterizing the likelihood of fragmentation in a disk, depends on the sound speed c_s which in turn

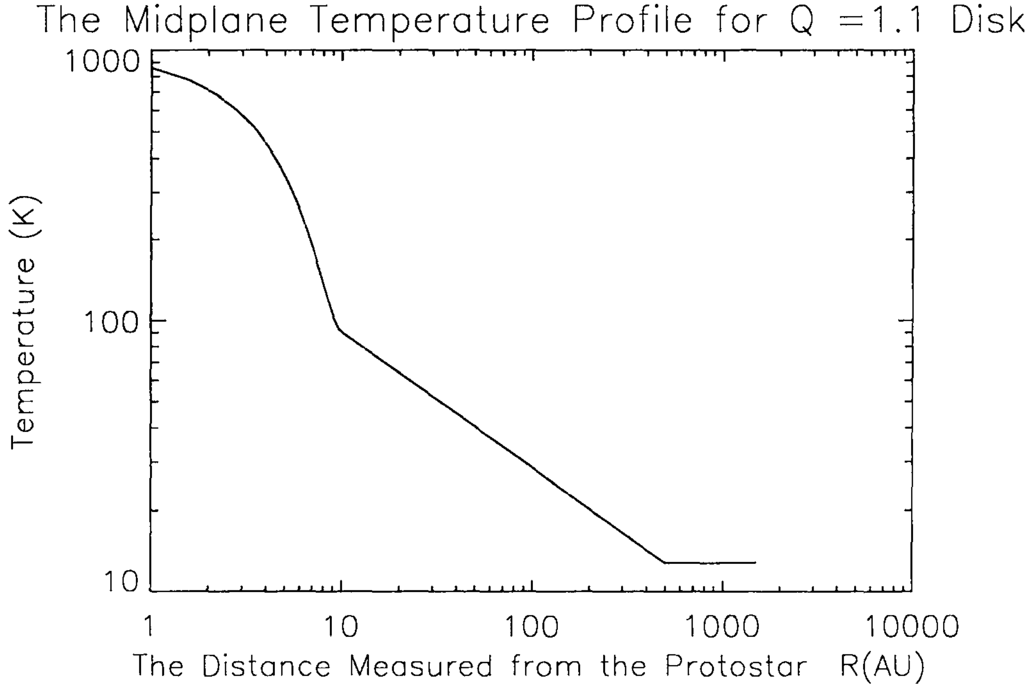

Figure 2.2 The midplane temperature profile plotted in logarithmic space for the initial protostellar disk with Q=1.1. The profile follows $T(r) = T_0 r^{-1/2}$ with r measured from the protostar.The temperature for $r < 10AU$ is fixed since the power law does not applied in the central region.

depends on the temperature. In this study, changing the minimum Q in the disk was done by modifying the ambient minimum temperature, i.e. shifting the $T(r)$ profile.

2.3.2 Generating a Self-consistent Disk Model

2.3.2.1 The Vertical Structure of the Disk

The vertical structure of each disk was constructed by assuming hydrostatic equilibrium in the vertical direction. Assuming the disk lies in x-y plane, the equilibrium can be expressed as

$$\frac{1}{\rho}\frac{\partial P}{\partial z} = \frac{\partial}{\partial z}\left[\frac{GM_*}{(r^2+z^2)^{1/2}}\right] + \frac{\partial \Phi_{disk}}{\partial z}, \tag{2.9}$$

where Φ_{disk} is the gravitational potential generated from the disk. The term on the left hand side is the pressure gradient, and terms on the right hand side are the gravitational force by the star and the disk, respectively. Writing the pressure in terms of density ρ, temperature T and molecular weight μ gives $P = \frac{\rho k_B T}{\mu m_H}$. Inserting P back into Equation 2.9 gives

$$\frac{k_B T}{\mu m_H}\frac{\partial \ln \rho}{\partial z} + \frac{k_B}{\mu m_H}\frac{\partial T}{\partial z} = \frac{\partial \Phi_{disk}}{\partial z} - \frac{GM_* z}{(r^2+z^2)^{3/2}}. \tag{2.10}$$

The self-gravity of the disk Φ_{disk} is obtained by solving Poisson's equation $\nabla^2\Phi = 4\pi G\rho$ by a multipole expansion technique (Binney & Tremaine, 1987). Briefly, assuming there is a distribution of point masses with spherical coordinates (r, θ, ϕ), each with the same mass m, the potential they generate at a specific coordinate (r_0, θ_0, ϕ_0) is

$$\Phi(r_0, \theta_0, \phi_0) = -4\pi G \sum_{l=0}^{\infty} \sum_{m=-l}^{l} \left[r_0^l \sum_{r>r_0} \frac{\sigma_{lm}}{r^{l-1}} + \frac{1}{r_0^{l+1}} \sum_{r<r_0} r^{l+2} \sigma_{lm} \right] Y_l^m(\theta_0, \phi_0) \tag{2.11}$$

with σ_{lm} defined as

$$\sigma_{lm} = \frac{m}{4\pi(2l+1)r^2} Y_l^{m*}(\theta, \phi). \tag{2.12}$$

Y_l^m is the spherical harmonic function and Y_l^{m*} is its complex conjugate. Note that the potential is accurate only when $l \to \infty$. However, in numerical calculations the summation has to be truncated. In this study 100 terms were summed so that the force errors were reduced to within 1 % for a test gravitation potential where an analytical expression exists. Also, the expression 2.12 is for discrete particle masses, but in the disk model only the total density ρ was calculated, so the mass m in Equation 2.12 should be replaced with $\rho 2\pi r dr dz$.

The last condition required to determine the density profile was the integration of the density along the vertical direction, which gives the surface density,

$$2 \int_0^{Z_{max}} \rho(r, z) dz = \sigma(r). \tag{2.13}$$

Here $z = 0$ indicates the midplane of the disk, and Z_{max} in this calculation is 1200 AU, large enough to include the flared disk. The factor of two comes from the two sides of the disk.

The calculation of $\rho(r, z)$ uses an iterative method. Radial temperature and surface density profiles are specified before the iteration as in previous sections.

Starting with a guessed midplane density, Equation 2.10 is integrated without the self gravity term and a vertical density distribution is obtained. The surface density can consequently be calculated by Equation 2.13. Comparing it with the specified surface density, the guessed midplane density is updated and a new iteration begins. This process is repeated until the surface density obtained from the integration of Equation 2.13 is the same as the specified one. Then a multipole expansion is used to find the self-gravity potential. The gradient of the potential is included in 2.10 in the next round of iterations described above, and a new density distribution is obtained which in turn changes the potential. The integration is repeated until the self-gravity potential converges, and a self-consistent disk model results. Figure 2.3 shows an example density distribution. Compared with the disk density contours from simulations of collapsing molecular cloud cores by Yorke & Bodenheimer (1999) (Figure 2.4), the density contours show similar structure: the disk is extended, the scale height increases with radius and is very flared (i.e., the $\log \rho = -20\ g/cm^3$ contour hits $z \sim 1000AU$ at the outer radius in this work and $z \sim 1500AU$ in their models).

2.3.2.2 Rotation Velocity and Toomre Q

Without the accretion and infall motion in the initial model, and assuming the disk is vertically in equilibrium, the gas velocity is dominated by rotation. The rotational velocity v_ϕ is calculated using:

$$\frac{\partial}{\partial r}\left[\frac{GM_*}{(r^2+z^2)^{1/2}}\right] + \frac{\partial \Phi_{disk}}{\partial r} - \frac{1}{\rho}\frac{\partial P}{\partial r} = \frac{v_\phi^2}{r}. \tag{2.14}$$

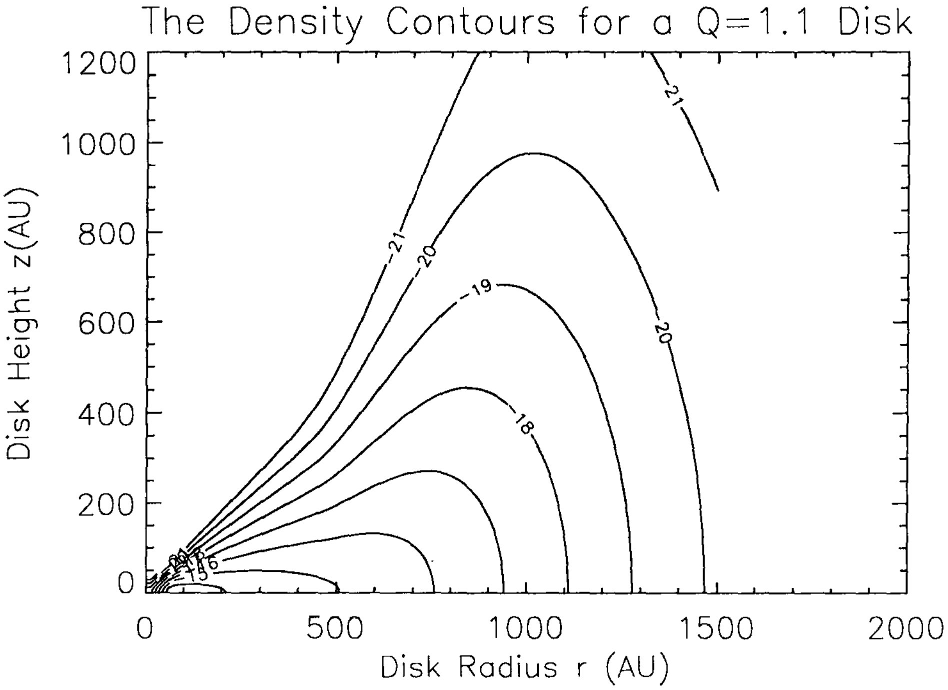

Figure 2.3 The density contour in logarithmic space for an initial protostellar disk with Q = 0.9. The contours are from $\log \rho = -13$ to $\log \rho = -21$ and separated by $\Delta \log \rho = 1.0$. The densities are in the units of g/cm^3. The total mass of the disk is 0.6 $M_\odot$.

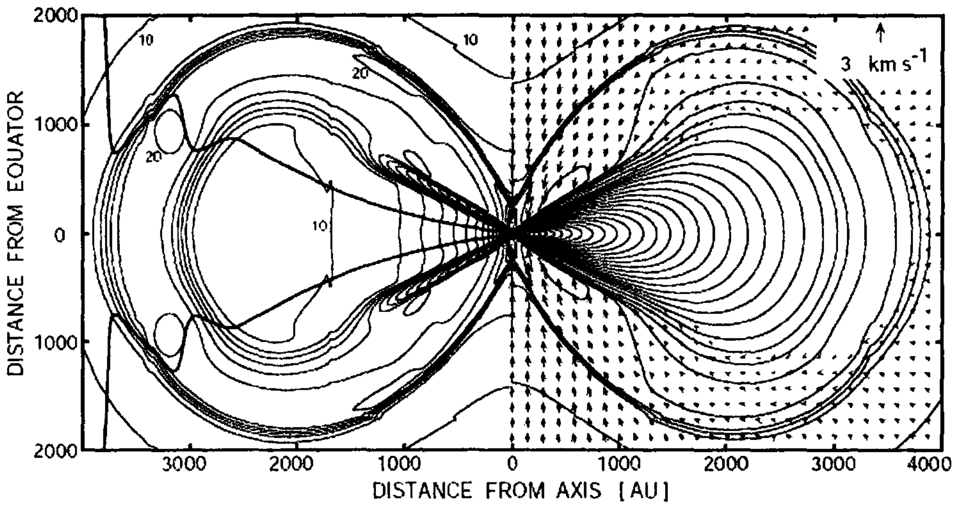

Figure 2.4 The density contours from the simulation of collapsing of a 2 $M_\odot$ molecular cloud core by Yorke & Bodenheimer (1999). The lowest density contour corresponds to $\log \rho = -20.2$ and the separation of contours are $\Delta \log \rho = 0.2$. The disk mass is approximately 0.8 $M_\odot$. The densities are in the units of g/cm_3. Adapt from Yorke & Bodenheimer (1999), Figure 3.

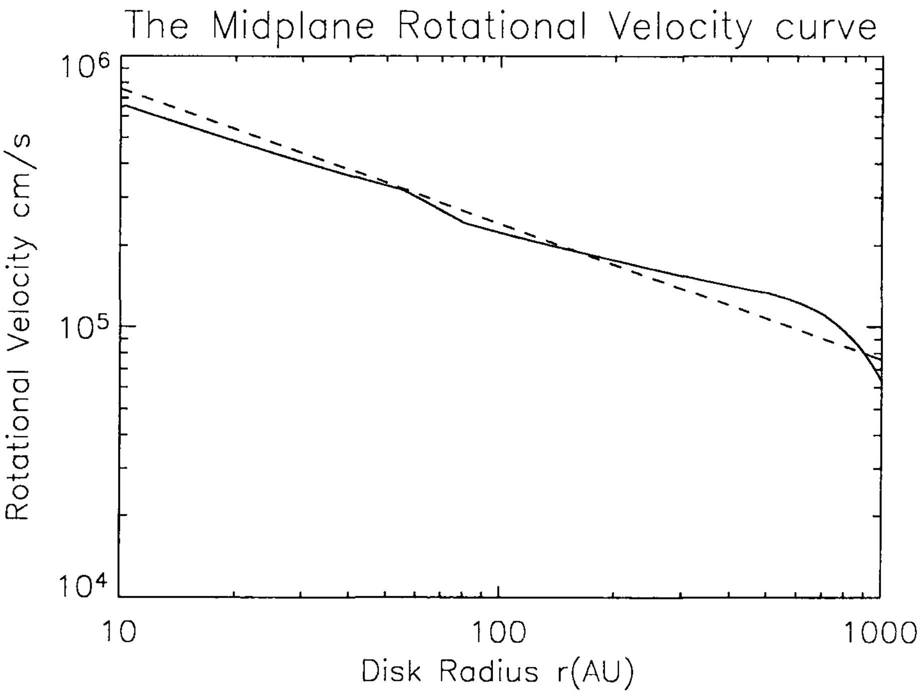

Figure 2.5 The midplane rotational velocity in the region of 10-1000 AU for a Q =1.1 protostellar disk (solid line) and a Keplerian rotation curve (dashed line).

Figure 2.5 shows the logarithmic plot of the midplane rotational velocity as a function of radius in the range 10 -1000 AU, and the power law $v = v_0 r^{-1/2}$ corresponding to Keplerian rotation for comparison. The presence of self gravity flattens the rotation curve, but the curve is still not significantly different from Keplerian rotation. The radial pressure gradient does not change the slope significantly, but the factor $1/\rho$ in the pressure term in above equation causes the velocity to drop when the density drops quickly in the outer disk.

Since the rotation is similar to Keplerian, when calculating Q, the calculated orbital frequency Ω is also similar to the epicyclic frequency κ, and the difference between the two is less than few percent. Therefore, it is appropriate to use the orbital frequency Ω instead of the epicyclic frequency κ in Equation 1.6. Figure 2.6 is a plot of Toomre Q as a function of radius. The minimum Q resides around 500 AU but remains almost constant in the range from 100 to 500 AU. Most single disk simulations (Mayer et al., 2004; Pickett et al., 2003) have shown that fragmentation happens in the disk region where Q is close to the minimum. In a physical encounter, when interaction between disks is so strong that the disk geometry and rotation velocity are significantly changed, the region of fragmentation may differ. However, Toomre's Q criterion is a good indication of global behavior of the disk, and so it is worth exploring the effect of the Q parameter on disk fragmentation in dynamical environments.

2.3.2.3 Modeling the Particle Disk

All of the calculations mentioned above are grid-based. In particular, density was one of the quantities in every fixed cell in space. The GASOLINE code, however, requires the input to be particle data— no grid is used and the density is represented by the distribution of particles. To convert the grid-based data to a particle disk, a quasi-random particle distribution was generated and the spacings between particles stretched or compressed according to the density calculated before. After the particle disk was generated, the evolution of the single isolated disk was simulated for about 10^4 years (the dynamical timescale for the gas within 500 AU), in order to eliminate numerical transients caused from the noise of initial particle distribution, to relax the initial profile in the inner disk, and to find the critical Toomre Q above

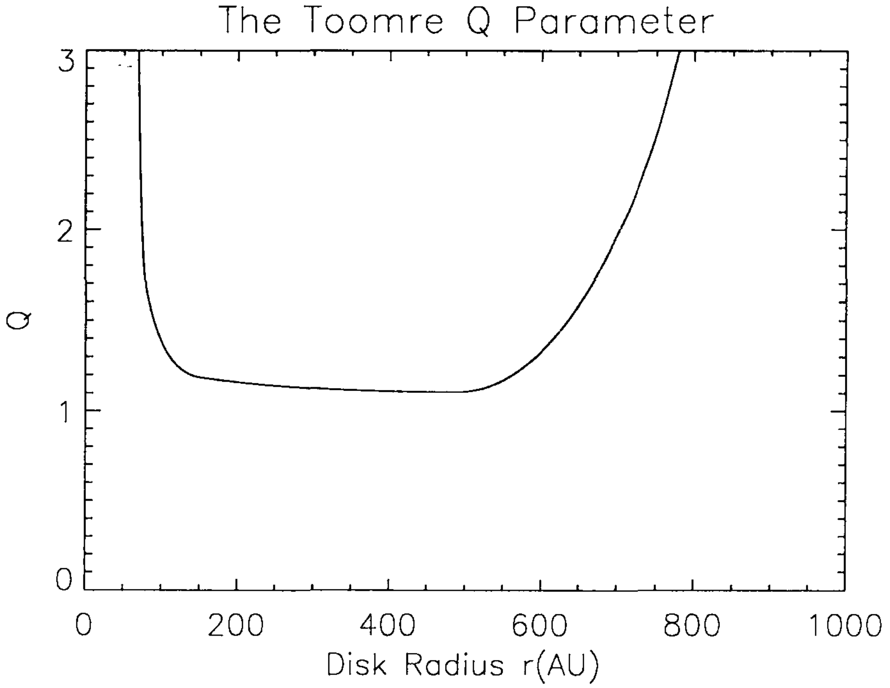

Figure 2.6 The Toomre Q parameter as a function of radius. The minimum Q=1.1 lies in the radius interval 100-500 AU.

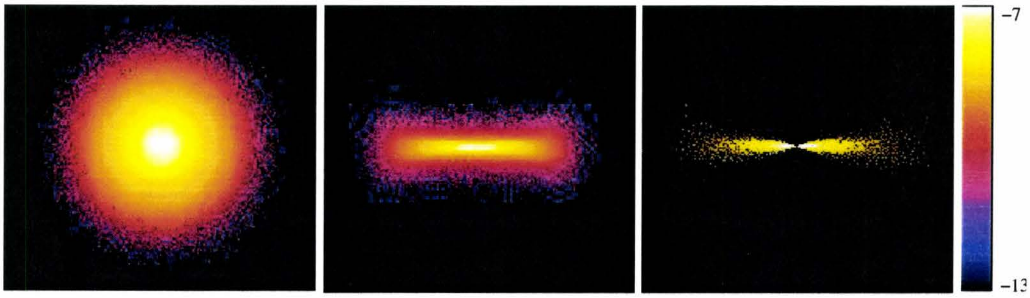

Figure 2.7 The initial protostellar disk represented by particles. *Left:* The disk plotted in x-y plane. *Middle:* The entire disk plotted in x-z plane. *Right:* A slice of the disk plotted in x-z plane, wiht the vertical flared structure clearly shown. The color bar shows the logarithm of density in code unit $M_\odot/AU^3$.

which the (isolated) disk is stable. Figure 2.7 gives an example of a particle disk of Q=1.1 after 9000 years of isolated simulation, with the colors showing the density in code units $M_\odot/AU^3$. The flared vertical structure is obvious in the third panel.

For a particle disk, density can be recalculated by smoothing with neighboring particles using Equation 2.2. Figure 2.8 shows the surface density profile (top) and the Q profile (bottom) of the particle disk in Figure 2.7. Compared to the grid-based data, density recalculated by particle smoothing is a little noisy, but it is still consistent with the surface density profile shown in Figure 2.8. Also, density inside 80 AU clearly increased due to the inward motion of gas, which makes the density profile more realistic. The minimum value of Q remains about 1.1, implying the disk is stable in this isolated environment.

Note that the particles used above for the gaseous disk were "gas particles", i.e., both SPH and gravity calculations were performed for these particles in the simulation. On the other hand, the central star was represented by a "star particle", for which only gravity was included. For gas particles, the simula-

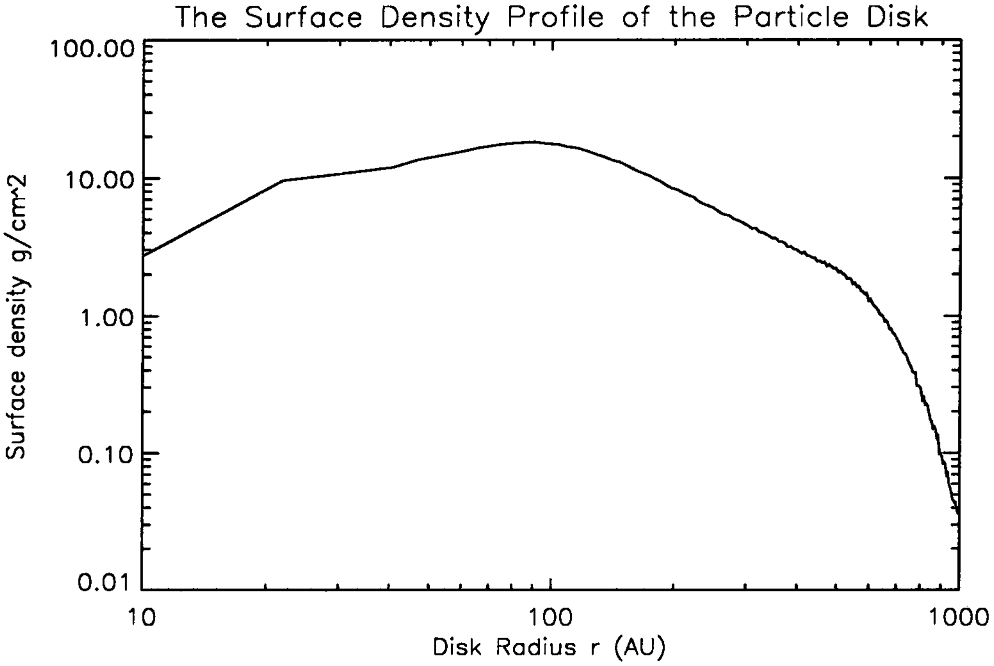

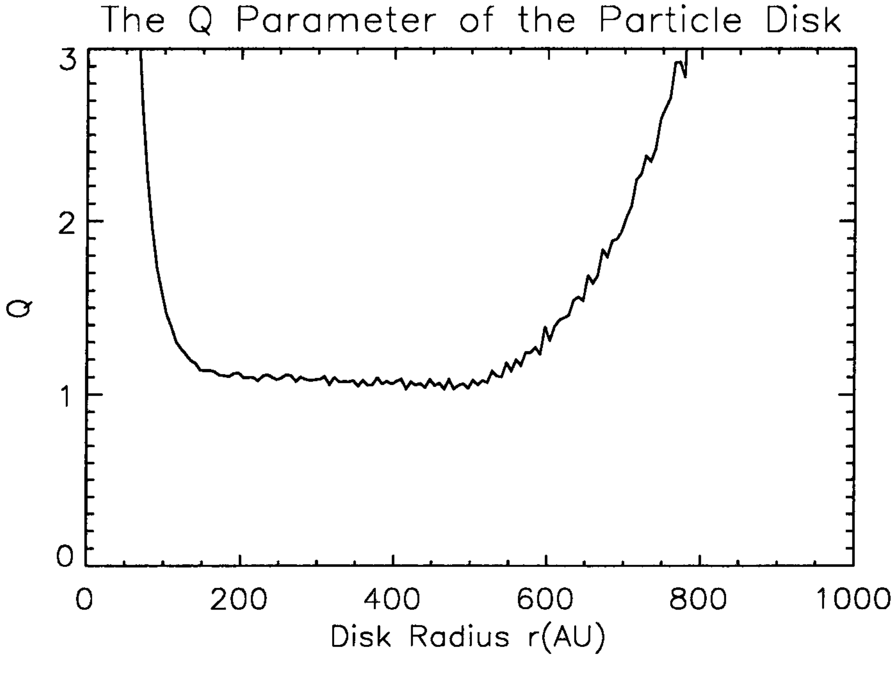

Figure 2.8 The density and Toomre Q profile recalculated from a stable disk. *Top*: The surface density profile. *Bottom*: The radial profile for Toomre Q.

tion used fixed numbers of neighbors $N_{neighbor} = 32$, and a fixed gravitationally softening length, ϵ, was used for every particle specified in the initial condition. In this study $\epsilon = 0.2\ AU$, which was about one-tenth of the smallest initial spacing. This means that when the density increased to 1000 times the initial maximum density, the gravitational force was still correct. For star particles, a softening of $\epsilon = 1.0\ AU$ was used. To avoid small timestep problems, stars were"sink particle" with radius 1.0 AU, i.e., all gas particles falling inside 1.0 AU were absorbed into the star with conservation of mass and angular momentum. The idea of sink particles was proposed and tested by Bate et al. (1995), who showed in his simulations that sink particles did not affect the overall results outside the sink region. Some local properties such as densities near the replaced regions are still notably changed. In this study, the interesting region was far away from the inner 1 AU disk so the presence of a sink particle within 1 AU was not expected to affect the results due to encounters and fragmentation. Nevertheless, since the incorporation of sink particles in GASOLINE had never been tested before, several simulations were carried out to ensure that their presence does not affect the behavior of the remote gas.

200,000 particles were used for a disk of total mass about 0.6 $M_{\odot}$. According to Bate & Burkert (1997), to prevent artificial fragmentation in SPH simulations, at least $2N_{neighbor}$ number of particles should be used to resolve the Jeans Mass. For the initial condition when the disk is optically thin and the highest density is about $10^{-7} g/cm^3$, 10^4 particles can satisfy this requirement. However, during fragmentation density will increase quickly. If cooling is still efficient, the Jeans mass will decrease by several orders of magnitude, and the requirement for resolution will increase rapidly. A particle number of 200,000 or more is able to satisfy the resolution condition when density increases by the factor of $10^3 - 10^4$ above the initial value. Studies of the effects of resolution on fragmentation are presented as part of the result in the next chapter.

2.4 Parameter Space and Equation of State

2.4.1 The Parameter Space Explored in This Study

After the initial condition for a stable disk was generated, a series of encounter initial conditions were produced. In every case the two disks were in the same orbital plane and had the same disk properties. Between cases, the following parameters differed:

- The Toomre Q parameter. Different values of Q were obtained by shifting the temperature profiles. Isolated disk simulations show that the disks are stable for $Q \geq 0.9$, so in the studies of encounters both disks initially had Q larger than or equal to 0.9.

- The initial velocity of each disk. The values are close to the velocity dispersion for stars in embedded clusters which has an order of a few km/s. In this study v = 0.4 km/s, 1.0 km/s, 2.0 km/s and 3.0 km/s were used. The two-disk system with each member having v = 0.4 km/s correspond to a bound system according to the initial disk separation.

- The orbit-spin correlation. In this work the term "prograde" is used for the cases in which the angles between spin and orbit vectors are less than or equal to $\pi/2$, and "retrograde" is used for cases in which the angles are greater than $\pi/2$ but less than or equal to π. In reality, the percentage of prograde and retrograde disks should be almost the same, so encounters between a prograde and a retrograde disk would be the most common case statistically. However, if the two disks had some correlation when they formed (e.g., formed from same molecular cloud core), the rate for two disks having same orbit-spin correlations can be high.

- The relative angle between two disk planes. There are generally two categories: "coplanar" and "non-coplanar", where "coplanar" denotes that the two disk planes have angle 0 or π, and "non-coplanar "denotes all the other cases. Angles of $\pi/4$ and $3\pi/4$ were used in general non-coplanar encounters in this study, except for one case of a perpendicular encounter, studied in order to compare results with the results by Lin et al. (1998).

The list above is the major parameter space which was explored. The detailed list of simulations with their parameters is given in next chapter before results are described.

2.4.2 The Equation of State

A local isothermal equation of state was used in most of the simulations. As stated in section 1.3.3, the meaning of local isothermal is that the temperature is a fixed function of radius, which in this study is the expression 2.8. When disks undergo encounters, for an arbitrary gas particle, the closer star is considered as the origin of the temperature profile. The local isothermal approximation is based on the assumption that cooling is so effective in the disks that the heating by sources other than star radiation, such as shocks, cannot raise the temperature significantly. For an initial disk, local isothermal is a good approximation, since the disk is extended and optically thin and radiation from the star is the only heating source. But during encounters, it is not clear if cooling is still effective, because both additional cooling, by dynamical expansion of the disks or turbulent motion of gas, and additional heating by shocks are present. Moreover, as argued by Bate et al. (2003), the rise of density due to fragmentation may change the clump-forming region to be optically thick and prevent fast cooling. Unfortunately, current computing ability cannot cope with all of the processes in one simulation. Considering that the disk geometry can enhance cooling, and the interaction between disks may cause disk expansion, this study assumed cooling is always effective and the locally isothermal condition was used. The assumption was tested, as explained in a later chapter, by comparing the heating rate in an adiabatic run and the cooling rate due to blackbody radiation.

Bibliography

Andre, P., Ward-Thompson, D., & Barsony, M. 2000, Protostars and Planets IV, 59

Barnes, J., & Hut, P. 1986, Nature, 324, 446

Bate, M. R., Bonnell, I. A., & Price, N. M. 1995, MNRAS, 277, 362

Bate, M. R., & Burkert, A. 1997, MNRAS, 288, 1060

Bate, M. R., Bonnell, I. A., & Bromm, V. 2003, MNRAS, 339, 577

Binney, J., &Tremaine, S., *Galactic Dynamics*, Princeton University Press, 1987

Boffin, H. M. J., Watkins, S. J., Bhattal, A. S., Francis, N., & Whitworth, A. P. 1998, MNRAS, 300, 1189

Gingold, R. A., & Monaghan, J. J. 1977, MNRAS, 181, 375

Hollenbach, D. J., Yorke, H. W., & Johnstone, D. 2000, Protostars and Planets IV, 401

Lin, D. N. C., & Pringle, J. E. 1990, ApJ, 358, 515

Lin, D. N. C., Laughlin, G., Bodenheimer, P., & Rozyczka, M. 1998, Science, 281, 2025

Lucy, L. B. 1977, AJ, 82, 1013

Mayer, L., Wadsley, J., Quinn, T., & Stadel, J. 2004, ASP Conf. Ser. 321: Extrasolar Planets: Today and Tomorrow, 321, 290

McCaughrean, M. J., Stapelfeldt, K. R., & Close, L. M. 2000, Protostars and Planets IV, 485

Monaghan, J. J. 1992, ARA&A, 30, 543

Najita, J. R., Edwards, S., Basri, G., & Carr, J. 2000, Protostars and Planets IV, 457

Ohashi, N., Hayashi, M., Ho, P. T. P., Momose, M., Tamura, M., Hirano, N., & Sargent, A. I. 1997, ApJ, 488, 317

Pickett, B. K., Mejía, A. C.,Durisen, R. H., Cassen, P. M., Berry, D. K., & Link, R. P. 2003, ApJ, 590, 1060

Wadsley, J. W., Stadel, J., & Quinn, T. 2004, New Astronomy, 9, 137

Watkins, S. J., Bhattal, A. S., Boffin, H. M. J., Francis, N., & Whitworth, A. P. 1998, MNRAS, 300, 1205

Watkins, S. J., Bhattal, A. S., Boffin, H. M. J., Francis, N., & Whitworth, A. P. 1998, MNRAS, 300, 1214

Yorke, H. W., & Bodenheimer, P. 1999, ApJ, 525, 330

Chapter 3

Simulations and Results

In this chapter, results of simulations of protostellar disk encounters with different parameters are presented. The first three sections focus on exploring the effects of Toomre Q parameter, disk configuration and encounter velocity, for which a series of simulations were carried out for comparison with each other. Then, a special case is presented, in which the encounter parameters were similar to those of the previous study by Lin et al. (1998) and the main goal was to follow the evolution of the extended tidal structures induced by the encounter and compare the result with that of Lin et al. (1998). Following this are test simulations of disks with different resolutions and vertical structures. Then a study of heating and cooling rates at different stages during the encounter is presented in order to demonstrate whether or not the local isothermal equation of state is a good approximation.

3.1 Simulations of Disk Encounters with Different Toomre Q

3.1.1 Initial Sets and Parameters

Although the minimum value of Toomre Q of the disk is an important parameter in isolated disk fragmentation, the effects of Toomre Q on fragmentation during encounters have not been explored. This section focuses on carrying out a series of two-disk encounters with different initial Q values. In this study, the initial sets of two disks had Q = 0.9, 1.1 and 1.3 respectively. And since the critical Q for an isolated disk is $Q_{crit} = 0.9$, the disks were all stable against fragmentation in the initial conditions. As illustrated in Figure 3.1, both disks had spin anti-alignment to the orbital plane, i.e., the disks were retrograde rotating and the encounter was coplanar. According to the work by Watkins et al. (1998a,b), in this configuration the system loses more energy than all the other encounters and is easiest to fragment. So it is appropriate to use retrograde-retrograde coplanar encounters to explore the maximum allowed Q for the disk to fragment in a dynamical environment. The disks were initially separated by 5800 AU and had velocity 0.4 km/s, corresponding to a marginally bound system. The impact parameter was set to be 1000 AU, which means that the material in the outer half of the disk radius underwent physical impact. The impact parameter will usually be reduced in actual encounters, especially for slow ones, because of the gravitational focusing effect (cf. Figure 3.1). The names of encounters and their parameters are listed in Table 3.1

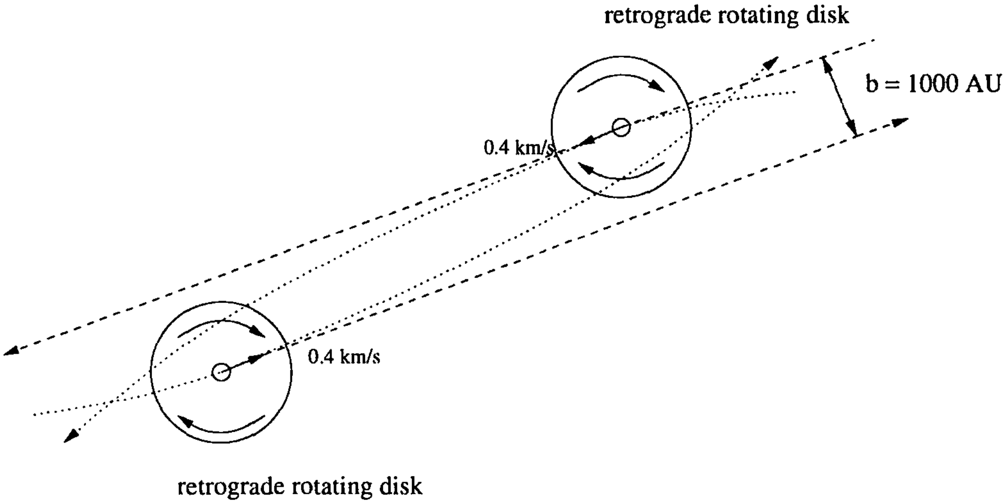

Figure 3.1 The initial configuration of the retrograde-retrograde coplanar encounters. *Dashed line:* the trajectories of the stars if gravitational focusing is not considered. *Dotted line:* the trajectories of the stars when gravitational attraction is included.

Case	Name	Q	Velocity (km/s)	Spin-orbit relation	Relative angle ϕ
1	Q09_rrco_4e4	0.9	0.4	rr	0
2	Q11_rrco_4e4	1.1			
3	Q13_rrco_4e4	1.3			

Table 3.1 Simulation parameters in studying the effects of Toomre Q. In all of the runs the two retrograde disks are coplanar. Here "rr" denotes retrograde-retrograde. The velocity of each disk is 0.4 km/s, corresponding to a marginally bound system.

3.1.2 Results of Retrograde-Retrograde Coplanar Encounters with Different Q

The Q = 0.9 retrograde-retrograde coplanar disk encounters are shown in Figure 3.2 and Figure 3.3. When the two disks approached each other, they were dynamically heated and the outer disks started expanding (Figure 3.2, panel 2). Since the rotational motion of the gas in disks was supersonic, when the physical impact began, a shock layer was quickly created. Gas was compressed in the layer and a sharp density transition between the shock and the environment was created. At the same time, pressure forces between disks produced outflows along the encounter section (Figure 3.2, panel 3,4). As the encounter continued, the gravitational coupling between the disks and the orbit became significant, and because of the spin-orbit anti-alignment configuration, the disks lost their angular momenta. As a result, accretion was enhanced and the density of inner disk increased. Due to the gas viscosity, the shock layer was then bent, connecting the two inner disks (hereafter the term "inner disk" means the inner interacting region with a radius of few hundred AU, but not the very inner boundary between star and the disk), and started trailing with the orbit (Figure 3.2, panel 5; Figure 3.3, panel 1). Because of the retrograde configuration of both disks, the density of shock layer kept increasing until it finally fragmented at $t = 24,000$ years (Figure 3.3, panel 2, 3). Meanwhile, the layer broke because the disks were moving apart. Moreover, the presence of the shock layer also triggered strong gravitational instabilities of the inner disks with $R < 200\ AU$, and the disks quickly developed spiral structures, followed by the inner-disk fragmentation (Figure 3.3, panel 4,5). At the end of simulation there were 8 fragments, and all of them were less than the mass limit of hydrogen burning ($\sim 0.075 M_{\odot}$), i.e., they were in the substellar region. Further evolution could not be simulated because of the small timestep in the fragments, but their orbits could roughly be estimated. The properties of the fragments are discussed in the following chapters.

The encounters of Q = 1.1 disks underwent physical processes similar to those of the Q = 0.9 encounter, e.g., the gas dissipation in the outer disks, the shock layer formation, the enhanced inner-disk accretion due to the spin-

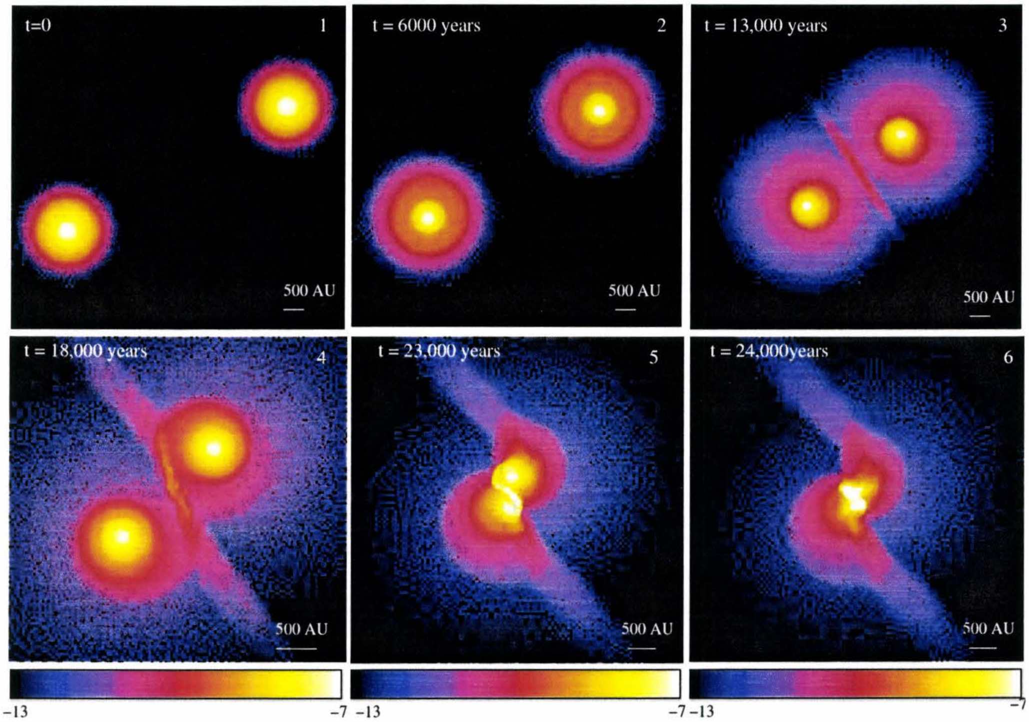

Figure 3.2 Q = 0.9 retrograde-retrograde coplanar disk encounter with velocity 0.4 km/s . The panels with label 1 to 6 are snapshots of the simulation output at timesteps 0, 6000, 13000, 18000, 23000, 24000 years, respectively. Color bars beneath the snapshots indicate the density ranges, which in this case are the same for all panels–from 10^{-13} $M_{\odot}/AU^3$ to 10^{-7} $M_{\odot}/AU^3$. The disks are clockwise rotating in all panels.

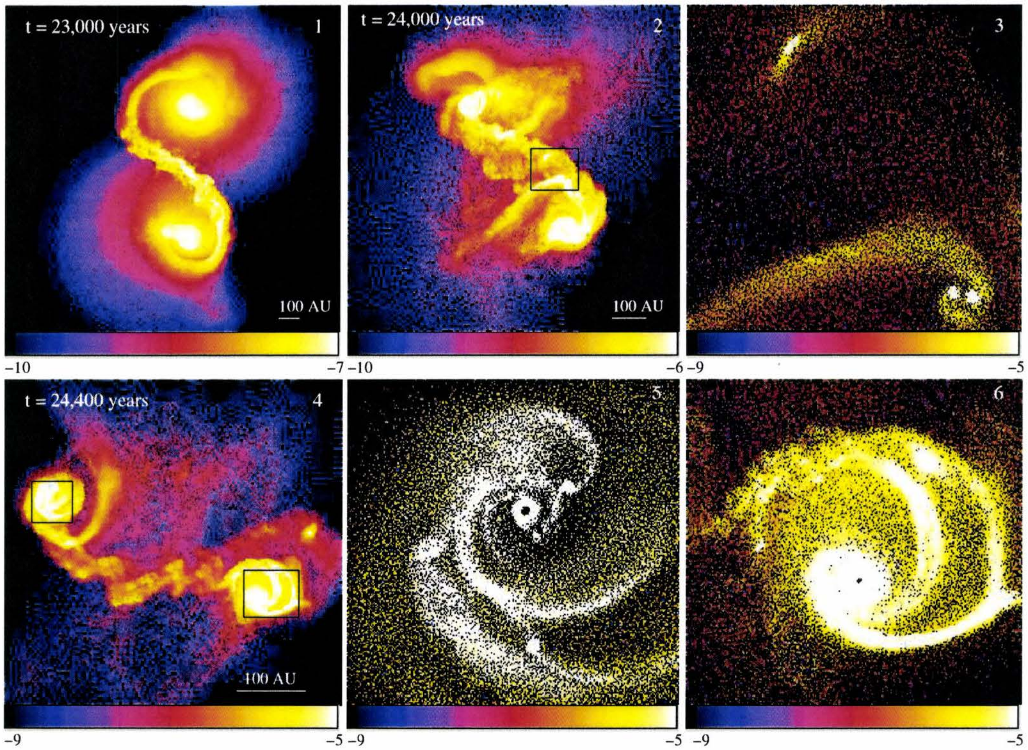

Figure 3.3 Fragmentation in the Q = 0.9 retrograde-retrograde coplanar disk encounter with velocity 0.4 km/s. Panel 1, 2 and 4 are the inner high density region at timesteps 23000, 24000 and 24400, respectively. Panel 3 is the zoom-in picture of the box in panel 2, which shows the fragmentation from the compressed gas in the shock layer and from a spiral arm of one of the disks. Panels 5 and 6 are the left and right inner disks of panel 4, respectively, both of which show the inner-disk spirals and fragments. Each panel has its own density, indicated by the color bars (in code units $M_\odot/AU^3$).

orbit interaction, the density growth the shock layer due to the retrograde rotation of the disks. However, unlike the gas in the Q = 0.9 encounter, the compressed gas in the shock layer did not fragment by itself; instead, as shown in Figure 3.4 (panel 5), it broke and dissipated when two disks were moving apart. Gravitational instabilities were still triggered in the inner disks. But compared to the Q = 0.9 disks in the previous simulation, the spiral structure growth was slower. As a result, by the end of simulation, only one of the two disks had fragmented and formed one clump at about 20 *AU* from the star. The other disk had merely spiral structures (Figure 3.4, panel 6).

The general picture of the Q = 1.3 coplanar encounter can been seen in Figure 3.5. A shock layer still formed due to the physical impact of materials in the disks, and as the encounter continued, it connected the two inner disks, but the density contrast between the shock and the disk was slight comparing to the lower Q cases. Moreover, the shock layer did not fragment or trigger the inner disk fragmentation, but enhanced the dissipation of the inner disk and, as a result, the disks were almost completely destroyed after 24000 years. The two stars captured each other and formed a binary system with a separation of about 20 AU, much smaller than the separation of the initial orbits. The remaining gas then formed a small circumbinary disk in which spiral structures were developed. However, the structures did not grow in density as in other cases. And by the end of simulation (t = 31000 years) there were no clumps formed.

It can be seen from previous three simulations that there are several processes in common for retrograde-retrograde disk encounters. Firstly, the outer

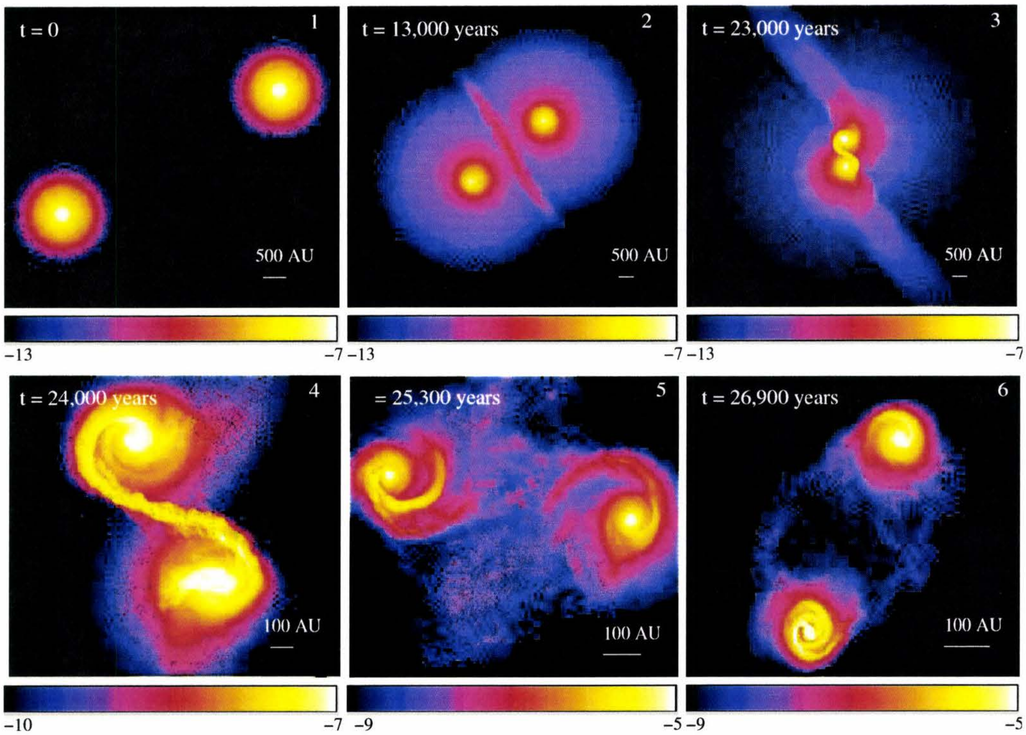

Figure 3.4 Q = 1.1 retrograde-retrograde coplanar encounter with velocity 0.4 km/s. The panels labeled with 1-3 are snapshots of the whole simulation box viewed top-down at timesteps 0, 13000 and 23000 years, respectively. The bottom 3 panels are snapshots of the inner region evolution during the encounter at timesteps 24000, 25300 and 26900 years, respectively. The lower left disk in panel 6 has one fragment at $\sim 20AU$ from the star. The disks are rotating clockwise. Color bars indicate the density ranges in the panels in code units $M_{\odot}/AU^3$ in logarithmic space.

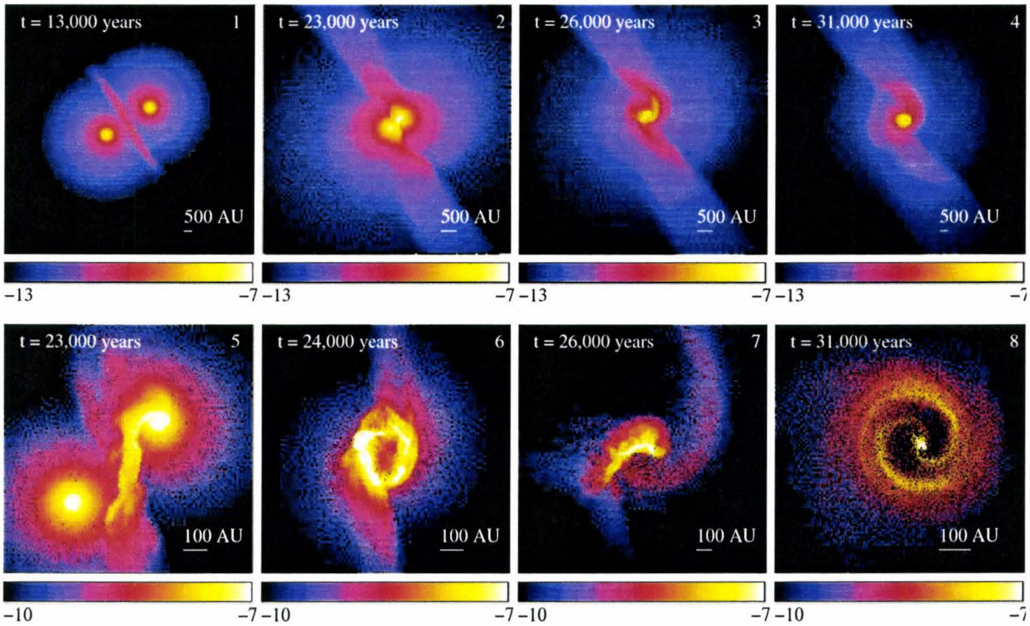

Figure 3.5 Q = 1.3 retrograde-retrograde coplanar encounter with velocity 0.4 km/s. The upper 4 frames show the whole simulation box at timesteps, from left to right, 13000, 23000, 26000 and 31000 years. The lower four frames show the inner disk evolution at timesteps, from left to right, 23000, 24000, 26000 and 31000 years. The disks are face on in all of the frames and rotating clockwise. The color bar under each frame indicates the density in code units ($M_\odot/AU^3$) in logarithmic space.

disks dissipate significantly due to the dynamical heating in the encounter, and do not fragment during the impact. Secondly, the spin-orbit interaction enhances the accretion of gas onto the inner disks (R $\sim$ few hundred AU). Thirdly, the formation and growth of a shock layer between the two disks is very significant and plays an important part in the fragmentation: the fragments form from either the condensation of the shock layer itself as in the Q = 0.9 case, or from the gravitational instabilities of inner disks induced by the presence of the shocks, as in both the Q = 0.9 and Q = 1.1 cases. Finally, the tidal interaction does not have destructive effects on the disks. Although the inner disks are slightly distorted near periastron (Figure 3.3, panel 1), no tidal tails are formed during encounters and carry out disk mass as described in the encounter simulations in Lin et al. (1998). This is because of the retrograde disk configuration, as discussed in detail in the next section.

Most simulations had to be stopped soon after fragments formed. But the brief picture of the retrograde coplanar encounters is clear: a shock layer of compressed gas forms during the encounter and can fragment by itself; the outer disks are destroyed by the impact, while the inner disks can either undergo dynamical accretion and fragmentation, or be completely destroyed and then help to form a close binary system. Also, it is obvious that disks with increasing Q have decreasing numbers of fragments. The encounter with disks with the lowest Q had eight clumps, from both the shock layer and disk fragmentation; the medium Q disk encounter had one clump forming only from inner disk instability; the highest Q encounter had no clumps at the end of simulation. This is different from the previous studies by Watkins et al. (1998a), who simulated the retrograde coplanar encounter of disks with Q =

2.4 but obtained many clumps. This discrepancy is primarily because of the differences in resolution and disk modeling. More quantitative analysis and discussion will be carried out in the next chapter.

3.2 Simulations of Disk Encounters with Different Configurations

The configuration of two disks, as described before, includes the orbit-spin relation and the relative angle (ϕ) between two disk planes. Studies of both protostellar disk encounters (Lin et al., 1998) and the merger of two disk galaxies (Binney & Tremaine, 1987) show that the spin-orbit relation is vital to the growth of gravitational "tidal tail" structures. For protostellar disk encounters, these structures can condense and form substellar objects (Lin et al., 1998), and in galaxy mergers they can form dwarf galaxies (Binney & Tremaine, 1987). Also, when the behavior of gas is taken into account, for different spin-orbit configurations the rates of energy dissipation may be different. For example, the study of Watkins et al. (1998a,b) suggested that the configuration of two retrograde disks is the most energy dissipative. The present section presents simulations of protostellar disk encounters with all possible configurations—prograde-prograde, prograde-retrograde and retrograde-retrograde, and studies the effects of spin-orbit relation on disk fragmentation.

Generally speaking, the relative angle between two approaching protostellar disks is not zero, i.e., the encounter is not coplanar, though the study by Whitworth et al. (1995) suggests that the possibility of coplanar is high if the disks form in same environment. For non-coplanar encounters, the two disks are actually "cutting through" each other instead of undergoing a "head on" impact, and if the spin of one disk is in the orbital plane (x-y plane), the rotational motion of gas for the other disk contains a vertical (z) component, i.e., the interaction is not confined to the disk plane. Therefore, to obtain the right gas behavior in the vertical direction during the encounter, a good disk model is essential. In this section, simulations of non-coplanar encounters with different spin-orbit relations are also presented.

3.2.1 Initial Condition and Parameters

The disk velocities of the simulations in this section have the same value, 1.0 km/s, similar to the velocity dispersion of embedded cluster (Stahler & Palla, 2004). Note that the two-disk systems are unbound this time. The disks all have Toomre Q = 0.9, since the study is focused on fragmentation, and from previous sections the Q=0.9 encounter is the easiest case for disk fragmentation. The impact parameter b is 1000 AU in all simulations in this section. The parameters are listed in Table 3.2, with "rr", "pp" and "pr" denoting retrograde-retrograde, prograde-prograde and prograde-retrograde, respectively.

Case	Name	Q	Velocity (km/s)	Spin-orbit relation	Relative angle ϕ
4	Q09_rrco_1e5	0.9	1.0	rr	0
5	Q09_ppco_1e5			pp	0
6	Q09_pp45_1e5			pp	$\pi/4$
7	Q09_rr45_1e5			rr	$\pi/4$
8	Q09_pr45_1e5			pr	$3\pi/4$

Table 3.2 Simulations of protostellar disk encounters with different configurations. All runs have disks with Toomre Q = 0.9 and velocity 1.0 km/s.

3.2.2 Coplanar Encounters

3.2.2.1 Retrograde-Retrograde Coplanar Encounters

The nature of retrograde coplanar encounters has been described in the previous section. The only difference between case 4 in this section and the case 1 in the previous one is the velocity. Because of this, Figure 3.6 shows similar snapshots to Figure 3.2 and Figure 3.3. The basic processes in this kind of encounter include the dissipation of the outer disks, the accretion of the inner disks, the formation and rapid density growth of a shock layer and the spiral instability and fragmentation of the inner disk within about 200 AU. Also, though the strong impacts stripped a large portion of mass from the disk, the region which did not undergo physical impact still keeps a disk shape (Figure 3.6, Panel 7). The main differences between the fast encounter (case 4) and slow encounter (case 1) are: firstly, the shock layer does not fragment when the two disks are moving apart, and secondly, the number of fragments in the inner disk is reduced. These differences were not seen in previous protostellar encounter simulations. However, this section will concentrate on encounter configurations, and the differences caused by velocities will not be explored here but be postponed to a later section where more simulations with different velocities are carried out.

3.2.2.2 Prograde-Prograde Coplanar Encounters

In the prograde-prograde coplanar encounter as shown in Figure 3.7, when the two disks were moving closer, the outer disk expanded. And as soon as the physical impact began, a shock layer of compressed gas formed as in the retrograde cases. The layer was also trailing with the orbit. However, because of the prograde configuration, the density growth of this shock layer only took place in a confined region instead of in an "S" shaped belt connecting the two inner disks as in the retrograde encounters (compare Figure 3.7 panel 7 with Figure 3.6 panel 5). The layer fragmented soon after the two disk started moving apart (the box region in panel 8 of Figure 3.7). Meanwhile, gravitational interaction between the disks distorted the inner disk region severely even though the inner part did not undergo physical impact. The fast growth of tidal tails of the disks can be clearly seen in Figure 3.7 (panel 8, 9, 10, the left disk). By the end of the simulation, one disk had developed two extended filamentary structures and the other was still developing a tail opposite to the encounter direction. The tidal tails extended to about 1000 AU and had density comparable to the inner disks. The tidal tails carried a lot of angular momentum from the disks and therefore the clumps formed from the shocks obtained large spins and underwent a secondary fragmentation at a timestep of 13,400 years. Since this simulations was stopped early, neither the inner

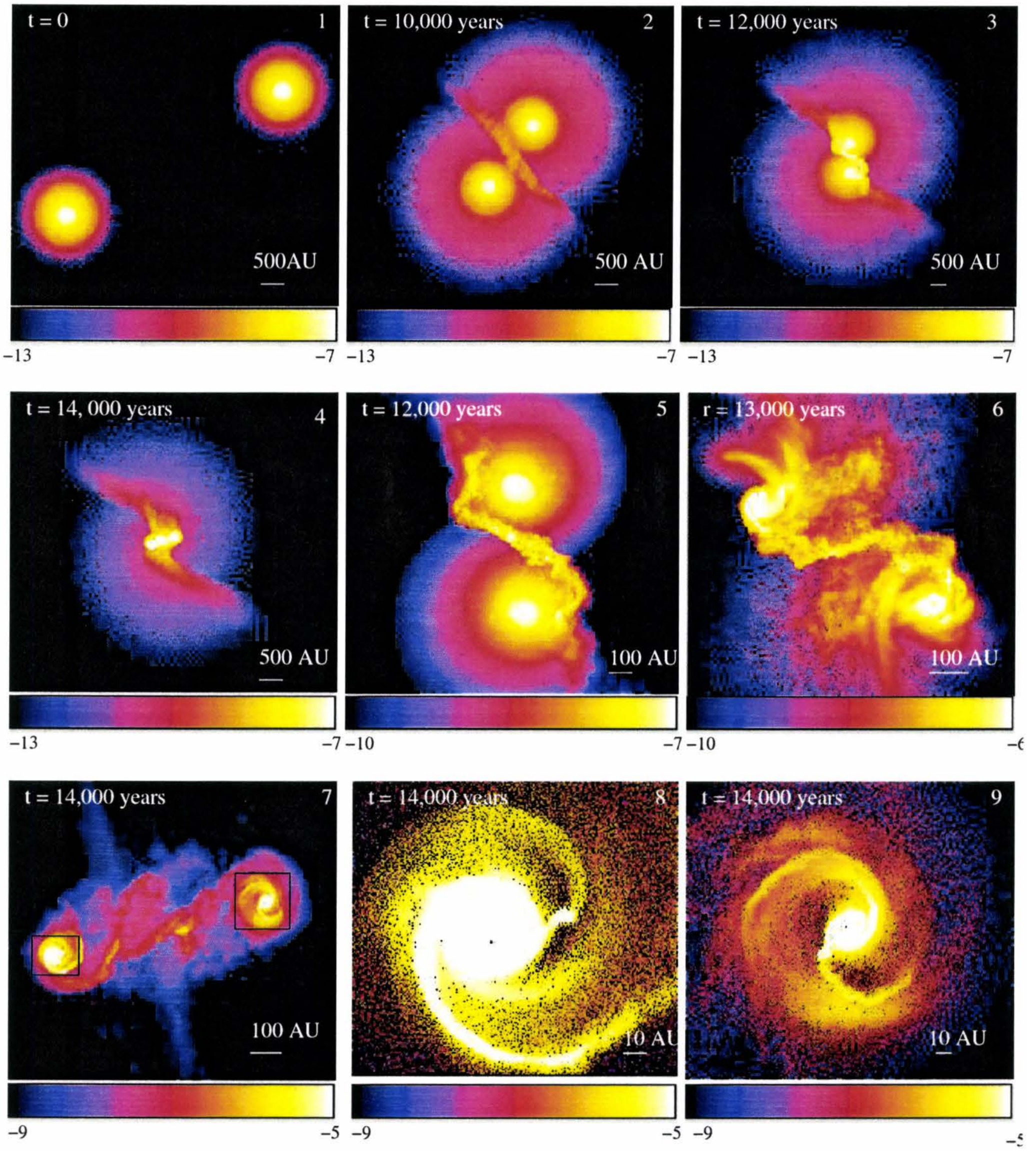

Figure 3.6 Retrograde-retrograde coplanar encounter with velocity 1.0 km/s. The first 4 panels labeled with 1-4 are the overall pictures viewed top down at timesteps 0, 10000, 12000 and 14000 years, respectively. The disks are rotating clockwise. The following 3 panels labeled with 5 to 7 are snapshots of inner dense region at timesteps 12000, 13000 and 14000 years, respectively. The last two panels are zoom-in pictures of the box showed in panel 7, with label 8 and 9 respectively corresponding to the left and right box in panel 7. The color bar beneath each panel shows the density scale in logarithmic space in code units $M_{\odot}/AU^3$. Note that for the inner region the density ranges are changed in order to clearly show the spiral structures and fragments.

disk nor the tidal tail fragmented at the end. However, it can be expected that, as the tidal structures carry out angular momentum, the inner disk will become more unstable. The total number of fragments was 7 at the end of the simulation, and all the clumps formed from the fragmentation of the shock layer.

3.2.3 Non-Coplanar Encounters

3.2.3.1 Retrograde-Retrograde $\phi = \pi/4$

The retrograde-retrograde non-coplanar encounter with relative angle $\phi = \pi/4$ is shown in Figure 3.8 and Figure 3.9. Compressed gas still formed when the impact began, but since the two disk planes were moving through each other the density increase of the shock region was not as strong as in the coplanar encounters. And it did not have time to became dense enough to fragment before the two disks were moving apart (Figure 3.9, panel 3). Also, as indicated in panel 1 and 2 in Figure 3.9, gas in the outer part of the tilted disk was dispersing more severely than in the coplanar disk. As a result, more angular momentum was carried out from the tilted disk. It therefore accreted more mass in the inner region and became denser. The encounter triggered spiral structures in both inner disks (with $R < 200$ AU), and both of them fragmented. By the end of the simulation, each disk had formed one self-bound clump, however, the tilted, denser disk had clearly stronger structures and thus it was expected to be easier to form more fragments. Again, as in coplanar

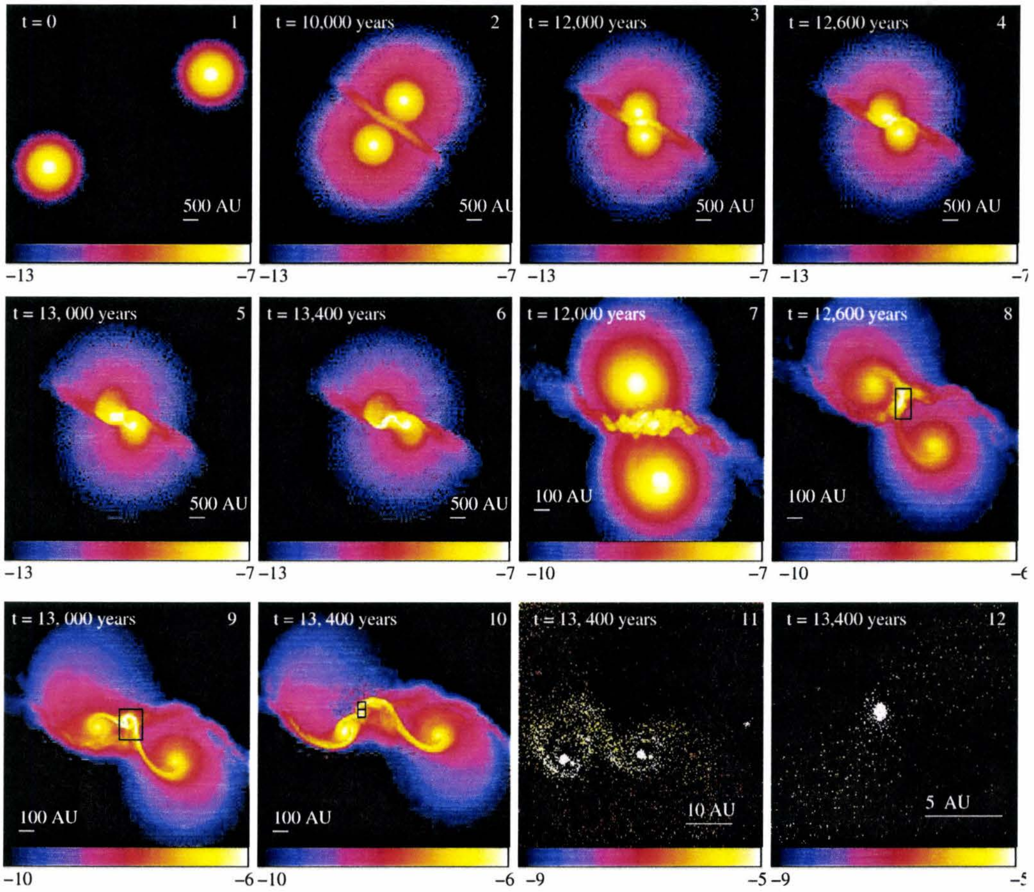

Figure 3.7 Prograde-prograde coplanar disk encounter. All the panels are snapshots from the simulation viewed top-down and the disks are all spinning counter-clockwise. Panel 1 to 6 are overall pictures of the encounter at timesteps 0, 10000, 12000, 12600, 13000 and 13400 years, respectively. Panel 7 to 10 show the inner disk evolution at timesteps 12000, 12600, 13000 and 13400, respectively. The boxes in these panels indicate the regions of fragmentation. The last two panels, with label 11 and 12, correspond to the fragmentation in the bottom and top boxes in panel 10. The color bar under each panel indicates the logarithmic density scale of that panel in code units $M_{\odot}/AU^3$

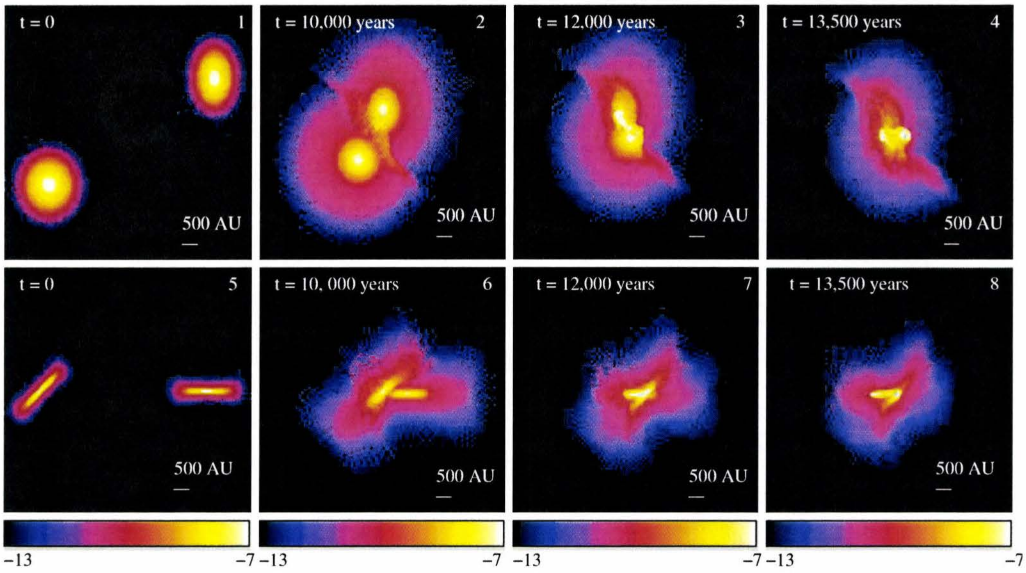

Figure 3.8 Retrograde-retrograde encounters with relative angle $\pi/4$. The top four panels are the snapshot of the whole simulation box viewing along the z-axis at timesteps 0, 10000, 12000 and 13500 years, respectively. The disks are rotating clockwise in the panels. The bottom four panels are the simulations at the same timesteps but viewing along the y-axis. The color bar under each panel shows the density scale in code units $M_{\odot}/AU^3$ in logarithmic space.

retrograde encounters, the disks were truncated by the physical impact, but the inner regions (within $\sim 200\ AU$) retained a disk shape.

3.2.3.2 Prograde-Prograde $\phi = \pi/4$

The non-coplanar prograde-prograde encounter is depicted by Figure 3.10 and Figure 3.11. Again, the non-coplanar configuration prevented the compressed gas becoming a dense shock "layer" and fragmenting as in coplanar cases. Instead, when the disks passed the periastron and starting moving away from each other, each disk developed two tidal tails extending in opposite directions due to the gravitational interaction. The tails along the encounter

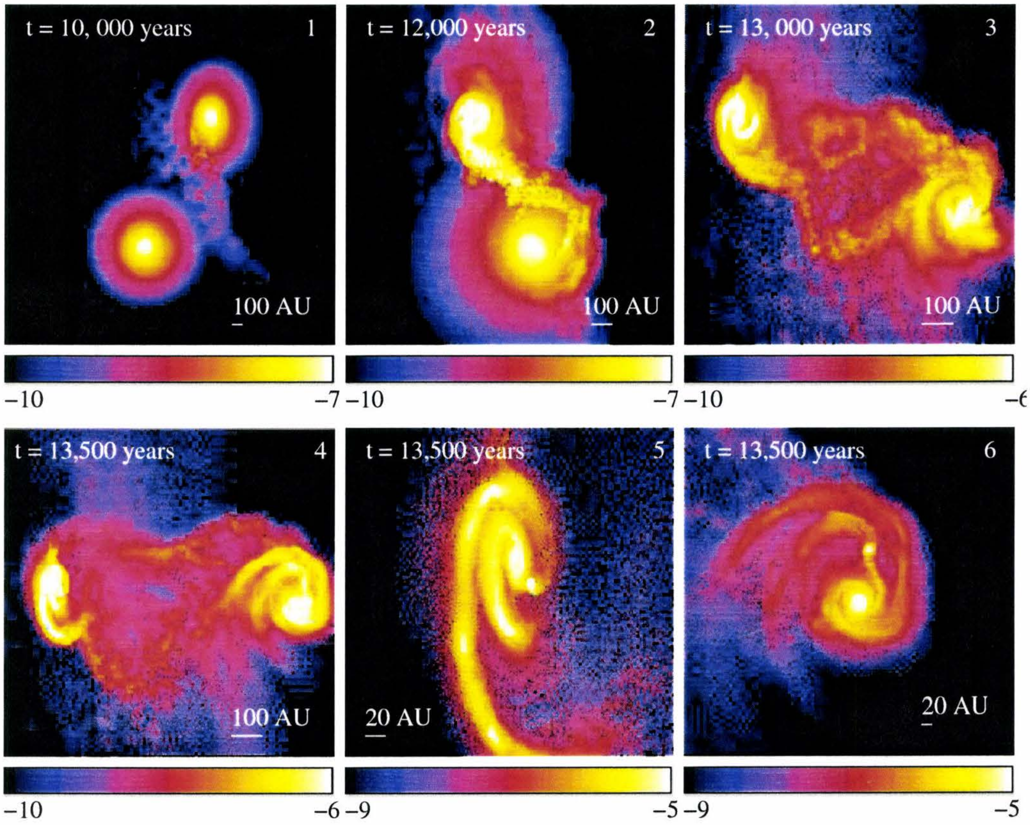

Figure 3.9 The inner disk evolution and fragmentation for retrograde-retrograde encounters with relative angle $\pi/4$. Panels labeled with 1-4 show the inner disks regions at the timesteps 10000, 12000, 13000 and 13500 years. Panel 5 and 6 show the fragmentation of each disk at the end of the simulation. Color bars indicate the density scales in code units ($M_{\odot}/AU^3$) in logarithmic space.

direction connected two disks (Figure 3.11, panel 3), grew in size and fragmented (Figure 3.10, panel 3; Figure 3.11, panel 4). One of the tidal tails of the disk within the orbit plane extended to about a thousand AU opposite to the encounter direction but the corresponding one in the tiled disk only extended to 500-600 AU. Later, spiral instabilities were triggered in both inner disks, and the tilted disk firstly fragmented. The reason is similar to the one in retrograde case, namely the encounters are more disruptive to the tilted disk, so the tilted disk accretes more mass in the inner region and becomes more unstable. Note that the overall density of the inner region in a prograde encounter is less than in a retrograde one at a similar timestep (e.g., compare Figure 3.9 panel 4 to Figure 3.11 panel 4), because in the prograde encounter a significant portion of disk mass is distributed in the tidal tails, and the spin-orbit relation is constructive and the interaction does not necessarily decrease the spin angular momentum. Also, in a prograde encounter the inner disk fragments at a later timestep than in the retrograde one (e.g., t = 15000 years in this case vs. t = 13500 years in the previous one). By the end of the simulation there were 3 clumps, two from fragmentation of the disk and one from the condensation of the tidal tail. The disks were strongly distorted after the encounter.

3.2.3.3 Prograde-Retrograde $\phi = 3\pi/4$

In the non-coplanar prograde -retrograde encounter, the strong impact disturbed the material in both disks and compressed the gas in the impact region. But still, there were no fragments formed directly from the shock

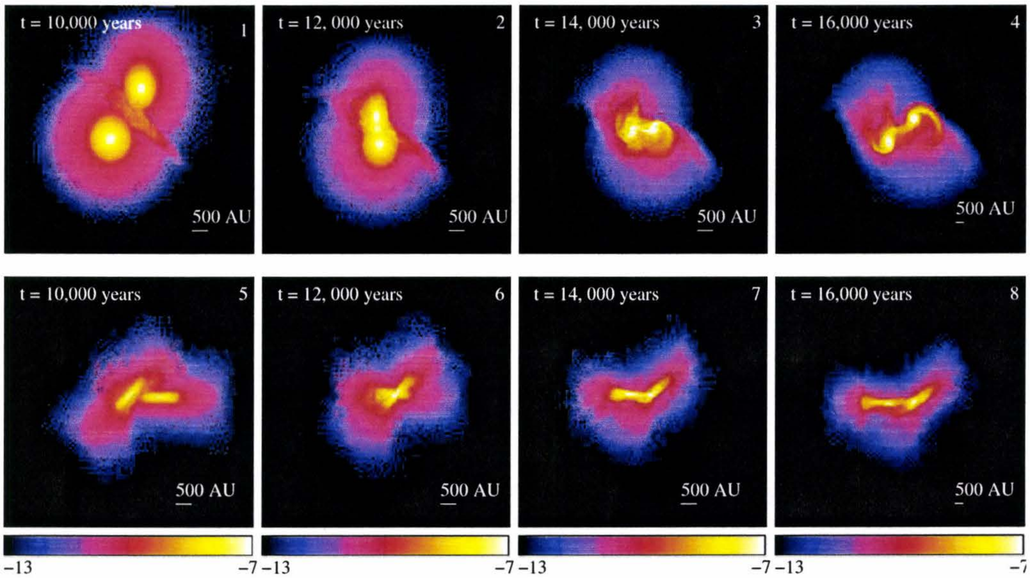

Figure 3.10 Prograde-prograde encounters with relative angle $\pi/4$. The top four panels are the snapshot of the whole simulation viewing along the z-axis at timesteps 10000, 12000, 14000 and 16000 years, respectively. The disks are rotating counter-clockwise in the panels. The bottom four panels are the simulations at the same timesteps but viewing along the y-axis. Color bars show the density scales in code units ($M_{\odot}/AU^3$) in logarithmic space.

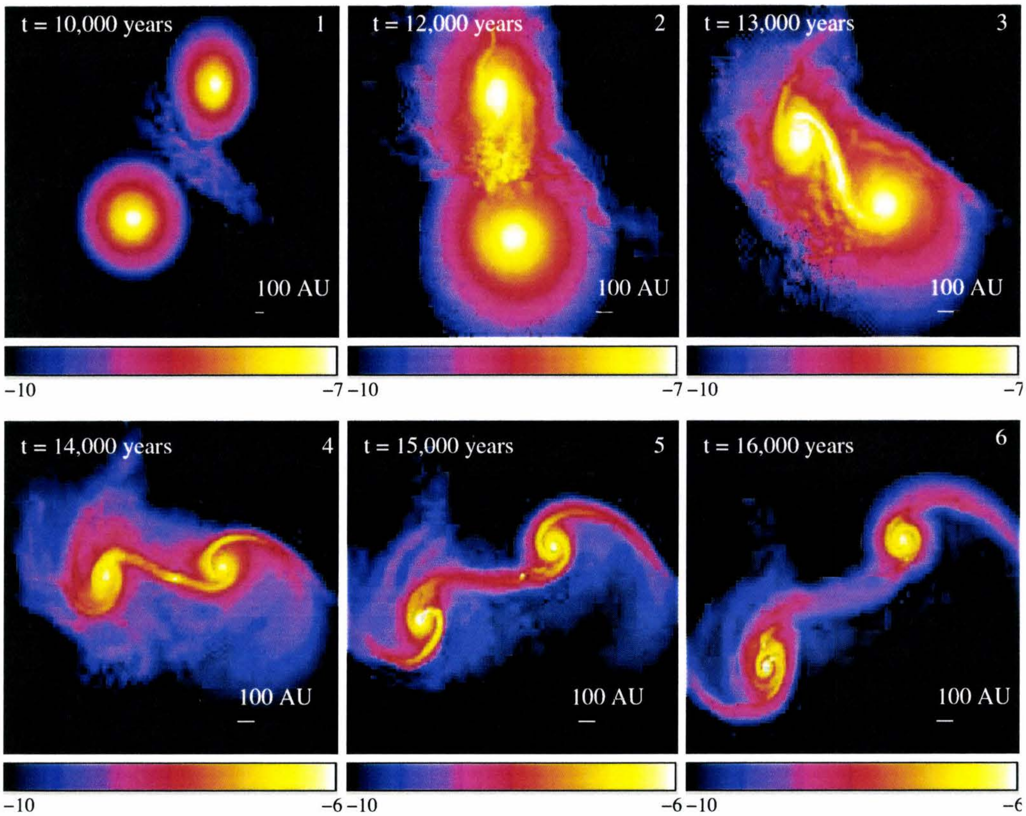

Figure 3.11 The inner disk evolution and fragmentation for Q = 0.9 prograde-prograde encounter with relative angle $\pi/4$. Panels labeled with 1-6 show the inner-disk regions at the timesteps 10000, 12000, 13000, 14000, 15000 and 16000 years. Fragmentation began at t = 14000 years. Color bars indicate the density scales in code units ($M_{\odot}/AU^3$) in logarithmic space.

region. As shown in Figure 3.12 and Figure 3.13, while the outer part of the disks dissipated due to the impact, the inner disks within about 200 to 300 AU kept accreting mass and became dense. With decreasing spin angular momentum, the retrograde disk accreted faster than the prograde one. As the two disks passed periastron, the tilted, prograde rotating disk developed large tidal tails which extended to 500-600 AU by the end of the simulation, while the retrograde rotating disk was simply truncated, its spirals did not grow outwards and the disk distortion was smaller. The denser, retrograde rotating disk then fragmented and formed two clumps with substellar masses at the end of the simulation.

The above simulations indicate that configurations make a significant difference in disk encounters. Firstly, prograde disks usually develop extended tidal tail structures during the encounters. The tidal tail can fragment itself and/or trigger the fragmentation of the inner disks (both happened in the prograde-prograde non-coplanar case). The inner disks are strongly distorted in the prograde configuration and have lower density than retrograde cases. For retrograde disks the encounter dissipates the outer disks while enhancing the accretion onto the inner disks. The inner disks surviving from the impacts are only weakly distorted, but compared with prograde rotating disks they have higher densities and are easier to fragment. Secondly, in coplanar encounters shock layers usually form, and their density growth depends on the spin-orbit relationship and the velocities of encounters. The shock layers can sometimes fragment (as in case 1 and 5) but in most cases they trigger disk instabilities (e.g., case 4). On the other hand, in non-coplanar encounters shocks neither form layers nor fragment. The clumps are from the condensation of

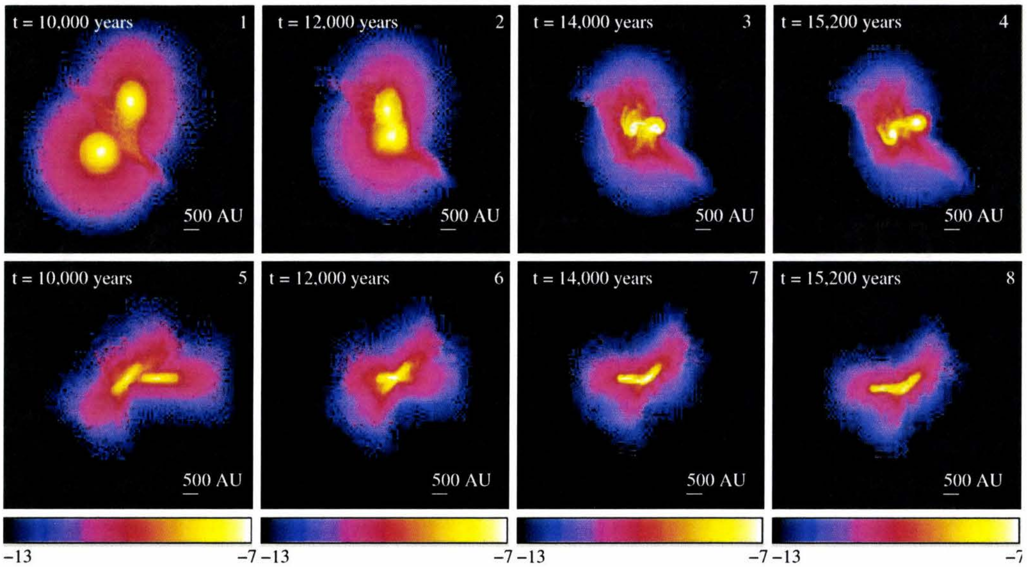

Figure 3.12 Prograde-retrograde encounter with relative angle $3\pi/4$. The top four panels are snapshots of the whole simulation viewing along the z-axis at timesteps 10000, 12000, 14000 and 15200 years, respectively. In these panels, the disk which is tilted and moving from top right to bottom left is prograde, counter-clockwise rotating disk. The one which lies in the same plane with the orbit is a retrograde, clockwise rotating disk. The bottom four panels are the simulations at the same timesteps but viewed against y-axis. Color bars give the density scales in code units $(M_{\odot}/AU_3)$ in logarithmic space.

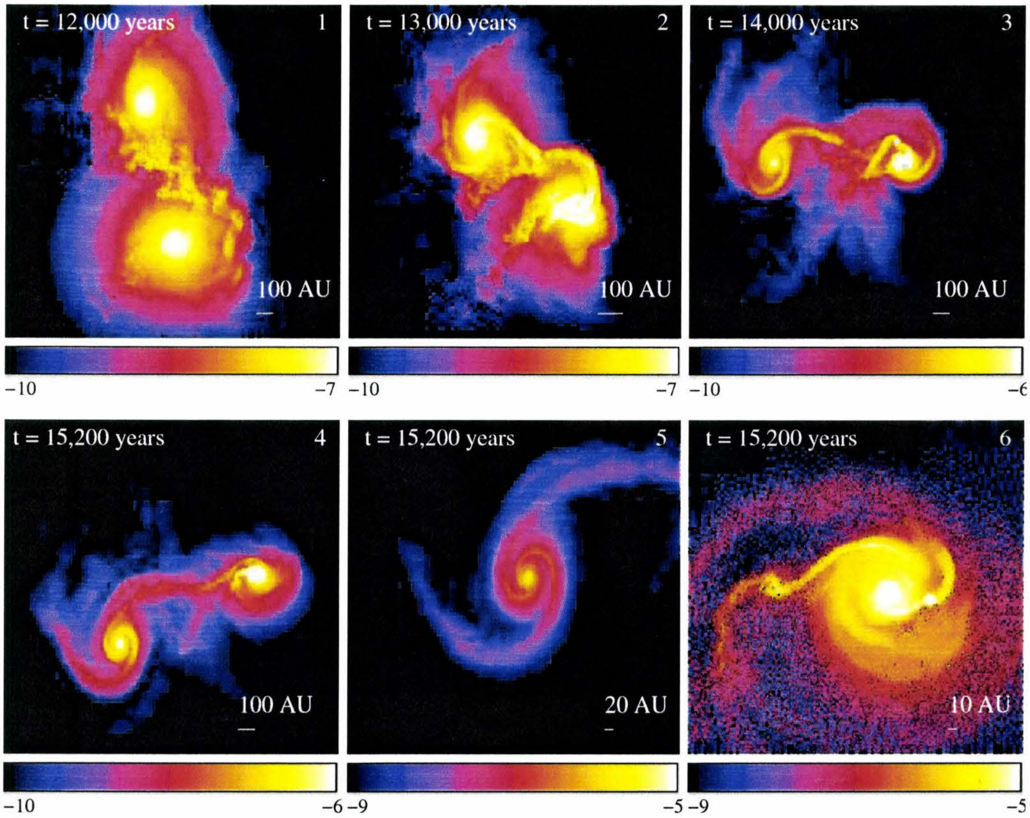

Figure 3.13 The inner disk evolution and fragmentation for the prograde-retrograde encounters with relative angle $\pi/4$. Panels 1-4 show the inner disk regions at timesteps 12000, 13000, 14000 and 15200 years. The last two panels indicate the differences between the prograde disk (panel 5) and the retrograde disk (panel 6). Fragmentation happened in the retrograde disk at the end of the simulation. Color bars give the density scales in code units $(M_{\odot}/AU_3)$ in logarithmic space.

tidal tails or gravitational instabilities in the inner disks. Thirdly, disks which are not in the same plane as the orbits are more disrupted in the encounter and easier to fragment than the disks with same spin directions but lie in the orbit planes.

The exploration of disk configurations in encounters reveals various mechanisms of fragmentation. The fragments formed by different mechanisms may have different properties, e.g., mass, orientation and orbit. More discussions will be carried out in next chapter after the velocity parameter is explored.

3.3 Simulations of Disk Encounters with Different Velocities

The velocity of the encounter determines the timescale of the mutual interaction of the two disks, and the interaction between the orbit and disk spin, so it is important in disk fragmentation. In this section the effects of velocity will be explored through simulations of encounters with velocities 0.4 km/s, 1.0 km/s, 2.0 km/s and 3.0 km/s, respectively. In the encounters with 0.4 km/s the two protostars are marginally bound to each other. Since differently configurations of the disks result in different physical processes during the encounter, it is necessary to use different configured encounters to study how velocity affects the fragmentation. In this study we chose the configurations of "prograde-prograde non-coplanar" and "retrograde-retrograde coplanar", because these two cases broadly represent the differences between prograde and retrograde disks, and between coplanar and non-coplanar encounters. The parameters are listed in Table 3.3.

Case	Name	Q	Velocity (km/s)	Spin-orbit relation	Relative angle ϕ
9	Q09_pp45_4e4	0.9	0.4	pp	$\pi/4$
6	Q09_pp45_1e5		1.0	pp	$\pi/4$
10	Q09_pp45_2e5		2.0	pp	$\pi/4$
11	Q09_pp45_3e5		3.0	pp	$\pi/4$
1	Q09_rrco_4e4		0.4	rr	0
4	Q09_rrco_1e5		1.0	rr	0
12	Q09_rrco_2e5		2.0	rr	0
13	Q09_rrco_3e5		3.0	rr	0

Table 3.3 Simulations of protostellar disk encounters with different velocities. All of the disks have Toomre Q = 0.9. Several runs are coincide with runs in previous sections, and they are indicated by using the same case number as before (case 1, 4 and 6).

Since some of the cases have been studied in previous sections when exploring other parameters, this section will only describe the new ones, but the comparisons may refer to previous figures.

3.3.1 Prograde Non-Coplanar Encounters with Different Velocities

The prograde-prograde $\phi = \pi/4$ encounter with velocity 0.4 km/s is depicted in Figure 3.14. The frames show the inner region evolution during the encounter. The tidal tail structures were triggered by gravitational interaction when the disks approached close to the periastron. Very soon after the tails were triggered, the stars captured each other and formed a close binary system. The tidal tails then wrapped around the binary, extending outwards with time and carrying out extra angular momentum from the system. The densities of the tidal tails were decreasing with time due to the growth in size of the structures. Finally, when the outer structures dissipated to very low density, a circumbinary disk with radius about 500 AU formed. The disk quickly underwent gravitational instability and fragmented. The final separation of the stars was about 90 AU, significantly smaller than the one in the initial condition.

The medium-velocity (v = 1.0 km/s) prograde-prograde encounter was simulated in the study of encounter configurations (case 6). As described in Section 3.2.3.2 and Figure 3.10, the encounter mainly produced large tidal structures. The ones connecting two inner disks fragmented, while the ones extending opposite to the encounter direction grew in size and decreased their density. The instability was then triggered by the tidal structures in the titled disk, which fragmented and produced two clumps at the end of the simulation.

The simulation of the fast prograde-prograde non-coplanar encounter with velocity 1km/s is shown in Figure 3.15. The disks were stripped of their outer parts by the fast impact and quickly moved apart from each other. Despite the high velocity, tidal tails still formed when the disks passed periastron. Again, they were extending outwards with time and decreasing in density. However, in this case the disks were moving too fast for the tails (which connected the disks) to condense before the gas dissipated. Also, different from the slower encounters, the spiral structure in the remaining inner disks did not fragment. Instead, the density contrast decreased with time (Figure 3.15 panel 7, 8 and 9), i.e., the inner disks were stabilized. Therefore, at the end of the simulation, when the two stars were already 10^4 AU apart, there was no fragmentation.

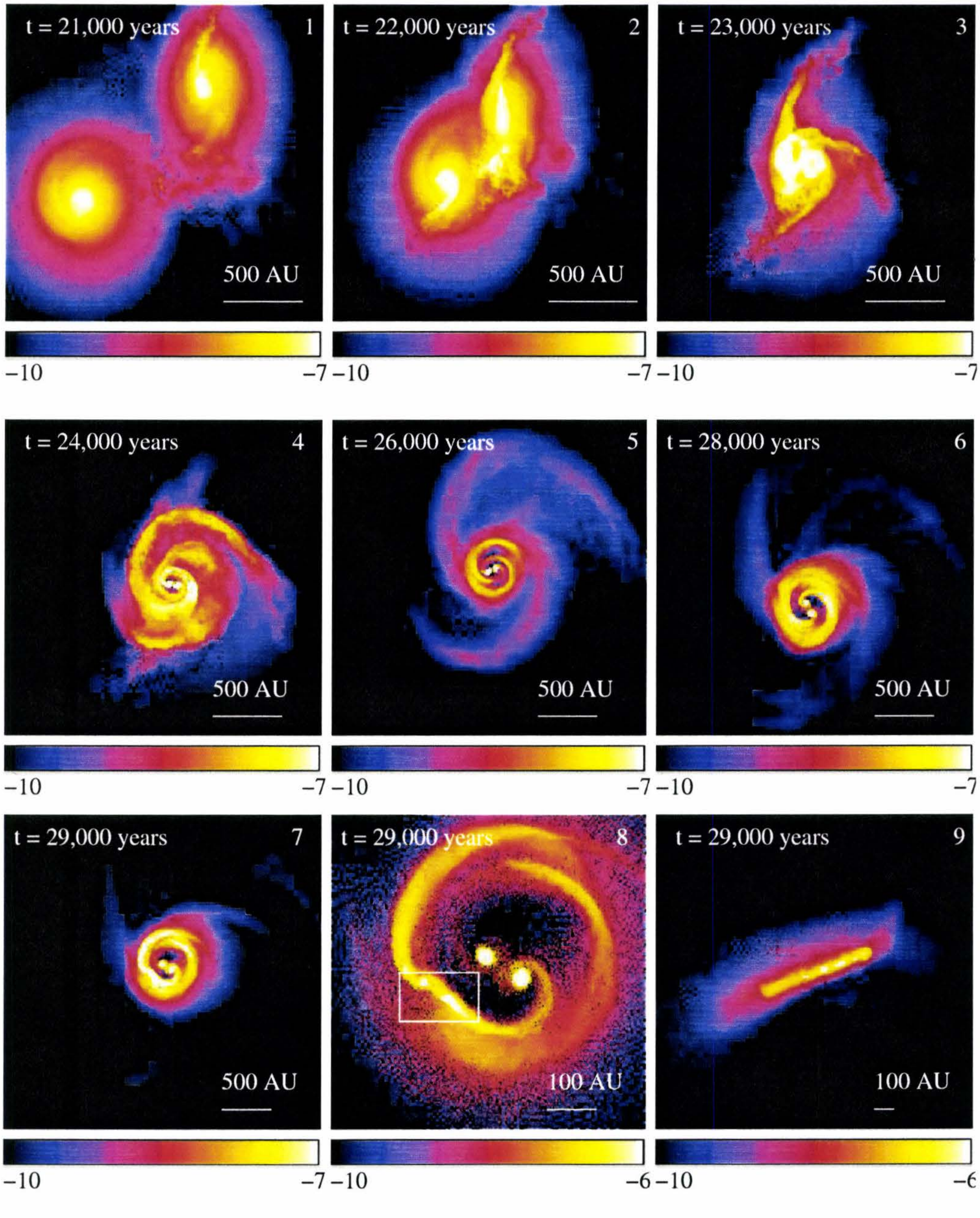

Figure 3.14 Prograde-prograde disk encounter with velocity 0.4 km/s. Panels 1-7 describe the inner disk evolution, the formation of the binary system and fragmentation of the circumbinary disk. Panel 8 shows the fragmentation region at the end of simulation. Panel 9 is the edge-on final disk. The angle between the circumbinary disk and the original orbit plane is clearly less than $\pi/4$. The color bar under each panel indicates the density range in code units in logarithmic space.

The even faster encounter with velocity 3.0 km/s was very similar to this one and also did not produce any fragments.

3.3.2 Retrograde Coplanar Encounters with Different Velocities

Retrograde-retrograde coplanar encounters with velocities 0.4 km/s and 1.0 km/s have been studied in exploring the effects of disks' Toomre Q parameter and the initial configuration of the encounter. The main results of these two encounters are: for the slower one, a shock layer of compressed gas formed, rotated with the disk, connected the inner regions of two disks and increased its density until fragmentation. The accretion of the inner disks was enhanced due to the interaction of anti-aligned spins and orbits. When the disks were moving away from each other the shock layer broke and spiral instabilities were triggered in the inner disks that produced a lot of fragments. There were 8 fragments formed by the end of the simulation, out of which there were 7 formed from inner disk instabilities. As for the encounter with velocity 1 km/s, the physical processes were very similar. However, the shock did not fragment when the two disks were moving apart, and both the 2 clumps at the end of simulation were contributions of inner disk fragmentation.

The fast retrograde-retrograde coplanar encounter with velocity 2.0 km/s can be seen in Figure 3.16. Again the shock layer formed and triggered instabilities in the disks, which had already been stripped most of their masses during the fast encounter. One of the disks fragmented by the end of simulation and formed 3 clumps. The other had spiral structures with growing density, so it is also expected to fragment. As in the v = 1.0 km/s encounter,

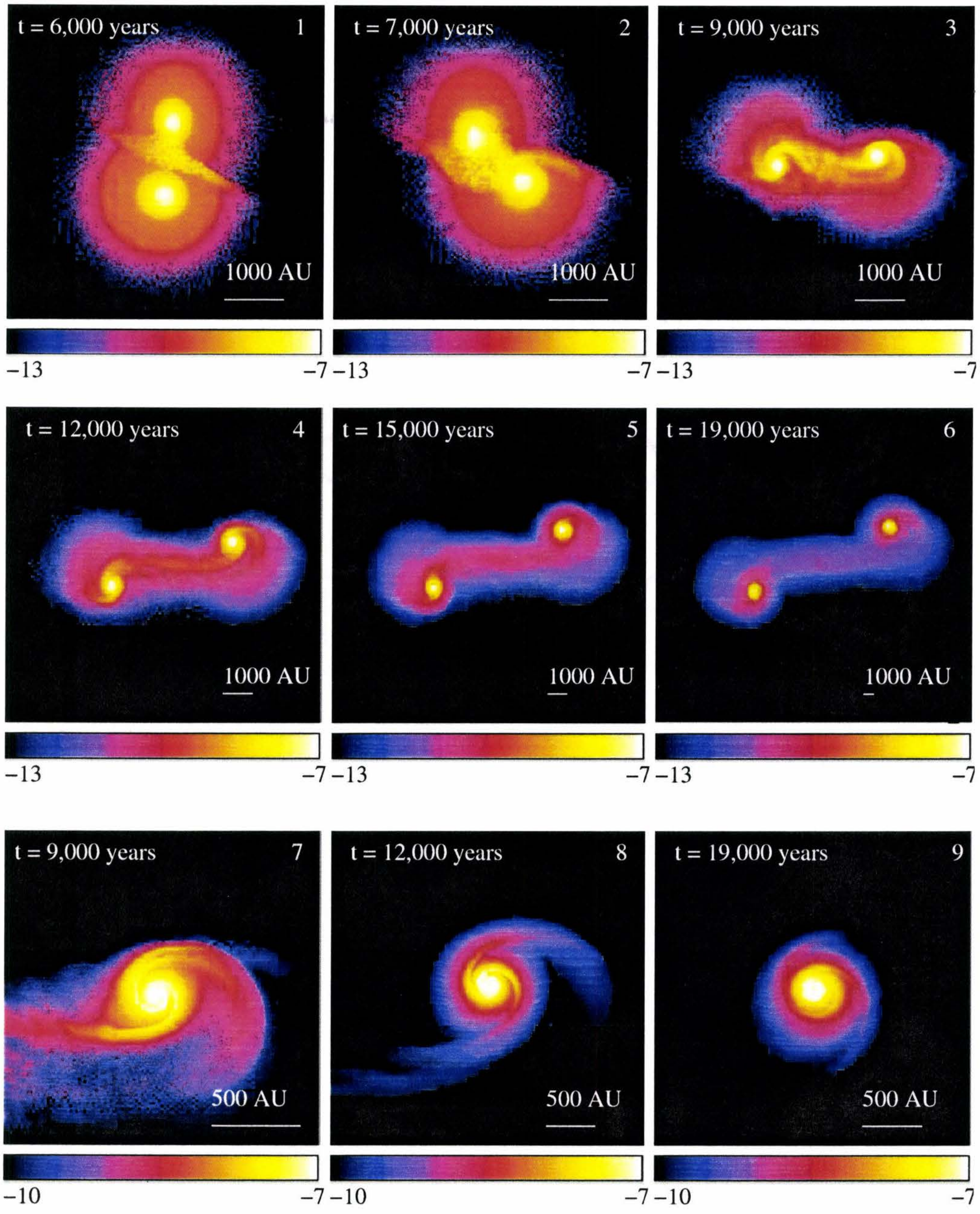

Figure 3.15 Prograde-prograde disk encounter with velocity 2.0 km/s. Frame 1 to 6 are snapshots of the simulation at timesteps 6000, 7000, 9000, 12000, 15000 and 19000 years, respectively. Panel 8 to 9 show the growth and dissipation of tidal structures associated with the disk which moves from left to right. The other disk behaved similarly. The disks were stabilized and there were no sign of fragmentation at the end of the simulation. The color bar under each panel indicates the density range in code units in logarithmic space.

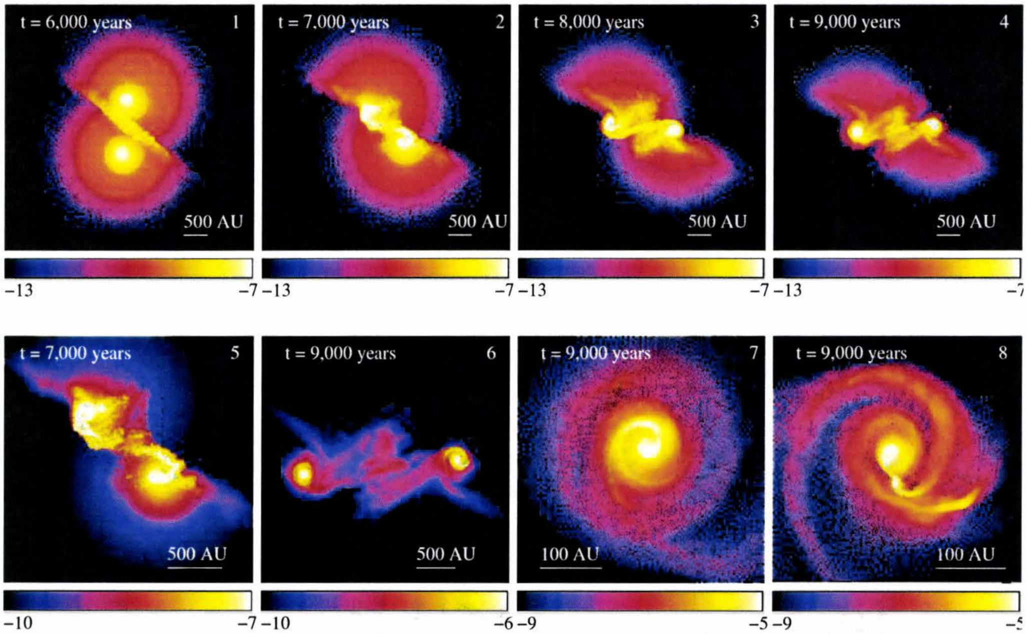

Figure 3.16 Retrograde-retrograde coplanar disk encounter with velocity 2.0 km/s. Frame 1 to 4 are snapshots of the simulation viewed top-down at timesteps 6000, 7000, 8000 and 9000 years, respectively. Panel 5 to 6 show the inner dense regions during and after the fast impact. The sizes of the disks were greatly reduced as in all the retrograde encounters at the end of the simulation. Panel 7 and 8 show the left and right inner disks in panel 6 in different zooming scales. Fragmentation happened in the right disk, which is shown in Panel 8. The color bar under each panel indicates the density range of that panel in code units in logarithmic space.

the shock layer itself did not fragment. Therefore, at the stopping time of the simulation, all clumps were produced by disk instabilities.

The most fast retrograde -retrograde coplanar encounter underwent similar physical processes as in the 2.0 km/s encounter. The only difference was, while the disks also had spiral structures, the density of the structures did not grow with time. At the end of simulation, there were no clump formed.

The above simulations show a broad trend of decreasing number of fragments with increasing encounter velocities. Especially, fragmentation of the tidal tails or shock layers only happened in slow encounters. Spiral instabilities were always triggered in the inner disk, but not all the disks fragmented. For retrograde-retrograde encounters, disk fragmentation happened in first three cases but not the one with the highest velocity. But no matter whether fragmented or not, the disks were always destabilized, because the coupling between spins and orbits reduced the disks' spin angular momenta and enhanced the accretion of the inner disks. For prograde-prograde encounters, on the other hand, the inner disks were stabilized when encounters were relatively fast, since the orbit-spin interaction could increase the spin angular momenta of the disks. The extra angular momenta were carried out by dissipation of the tidal tails, and strong inner-disk accretion did not take place. Therefore, only the relatively slow (0.4 km/s and 1.0 km/s) prograde-prograde encounters induced fragmentation.

3.4 Evolution of the Tidal Structure in a Perpendicular Encounter

It can be seen from the studies of disk configurations that prograde rotating disks can produce large tidal tails. In the simulation by Lin et al. (1998), fragmentation happened near the tip of the outwards-extending tidal tail and formed a substellar mass clump. For a better comparison between this study and the work by Lin et al. (1998), a special simulation case with parameters close to their work was designed. The parameters are listed in Table 3.4.

Case	Name	Q	Velocity (km/s)	Spin-orbit relation	Relative angle ϕ
14	Q09_pp90_4e4	0.9	0.4	pp	$\pi/2$

Table 3.4 The parameters for the prograde-prograde perpendicular encounter. The value of relative angle, spin-orbit relation and velocity are chosen to be close to the parameters in Lin et al. (1998).

Moreover, in order to to follow the evolution of tidal tail longer, any fragment which forms in the inner disk region will be replaced by a big gas particle with the total clump mass. The big particle sits at the clump's center of mass and has its center-of-mass velocity. This replacement solves the small timescale problem in the fragments and makes it possible for the simulation to continue after the first fragmentation. It significantly affects the evolution in the nearby regions of the clumps, but not the outer tidal structure since it extends far away from the dense part of the disk.

Figure 3.17 shows the snapshots of the late stage of the simulation. Similar to Figure 1 of Lin et al. (1998), the disk which shares the plane with the orbit developed a long filamentary structure, while the one perpendicular to the orbit had much shorter tails and fragmented soon. This is consistent with the results in Section 3.2.3 that non-coplanar disks are easier for structure growth and fragmentation during an encounter. The fragments were continuously replaced by big gas particles to prevent the short timestep problem. But as shown in the last panel in Figure 3.17, the tidal tail structure just dissipated and no fragment formed from it. The discrepancy between this study and the work by Lin et al. (1998) will be discussed in detail in next chapter.

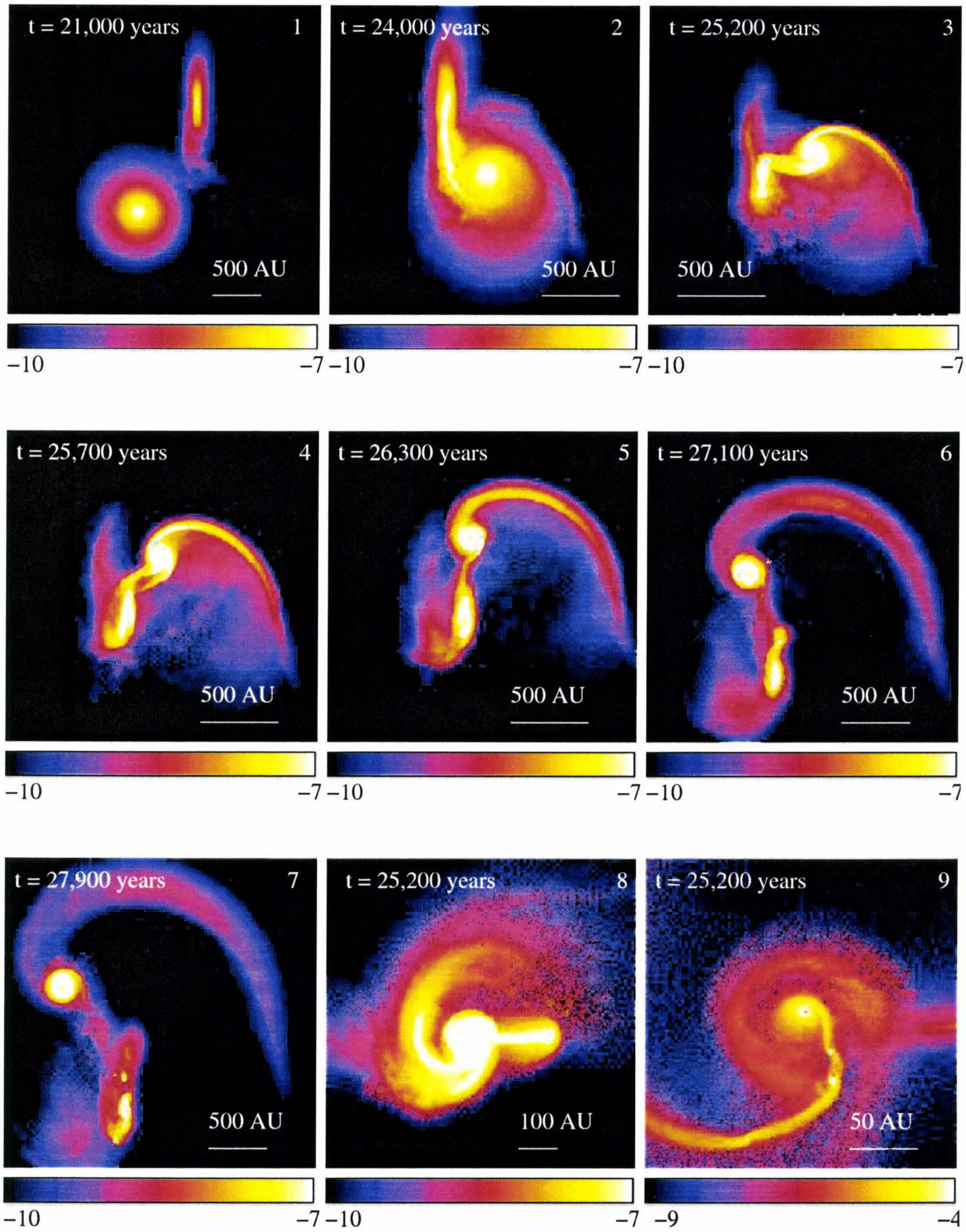

Figure 3.17 The prograde-prograde perpendicular encounter and the evolution of the extended tidal tail. Panel 1 to 7 are the snapshots viewing along z-axis at 21000, 24000, 25200, 25700, 26300, 27100 and 27900 years, respectively. First fragmentation took place at 25200 years. The followed snapshots all have at least one new clump replacement(s). The last two panels show the fragmented disk at 25200 years and the pictures are viewed along x axis.

3.5 Simulations with Different Resolutions and Disk Models

As emphasized in the introduction, high resolution and correct disk modeling are essential in simulating the fragmentation in protostellar disk encounters. In this section simulations of disk evolution with same parameters but different resolutions or initial disk models will be presented, and the results will be compared.

3.5.1 Isolated Disk Simulations

The first comparison was carried out using isolated disk simulations: three Q = 1.3 disks were simulated in isolation. The first disk was modeled with a single layer of 2000 particles. The second one used 20000 particles, but the disk still had no vertical structure. And the third one was similar to the disk initial condition in this study, in which 200000 particles were used and the flared vertical structure was resolved. The results are shown in Figure 3.18. The disks in first two cases (panel 1 and 2) both underwent strong disk instabilities and fragmented before 10000 years' evolution, but the third one did not develop any spirals and kept stable after evolving more than 20000 years (panel 3). The results demonstrate that even without an impact, a stable disk can appear to be very unstable if it is not well modeled or the resolution requirement is not satisfied.

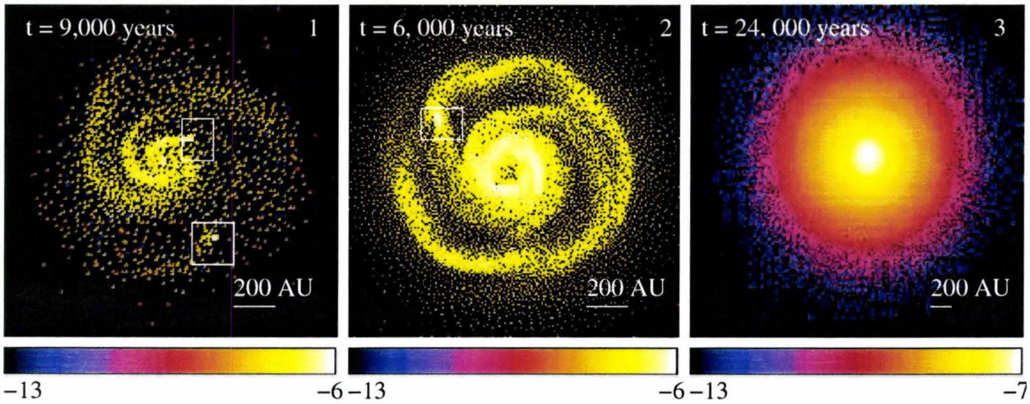

Figure 3.18 Isolated disk simulations with different disk models and resolutions. All the disks have Q = 1.3. Panel 1, 2 and 3 correspond to timesteps 9000, 6000 and 24000 years in each simulation. The number of particles used to model the disk in panel 1-3 is 2000, 20000, and 200000, respectively. The disks are razor-thin in the first two panels. Fragmentation regions are indicated by boxes. The color bar beneath each panel represents the density range in code units $M_{\odot}/AU^3$.

3.5.2 Simulations of Dynamical Interacting Disks

Two simulations were carried out to study the effects of resolution and disk modeling on dynamical interacting disks. Again Q = 1.3 disks were used. Both encounters were prograde-prograde coplanar and had impact parameter 500 AU, the initial velocity was 0.4 km/s. This initial set of parameters were chosen in order to close to one of the simulations (case dd01) in Watkins et al. (1998a) so that the result can be used to directly compare to their simulation results in next chapter. In the first simulation the disks were modeled with a single layer of 2000 particles, while in the second one disks were vertically resolved and modeled with 200000 particles. Figure 3.19 shows the simulation results. For the high resolution simulation (panel 3 and 4) the encounter had no fragmentation, but in the low resolution simulation a clump formed from

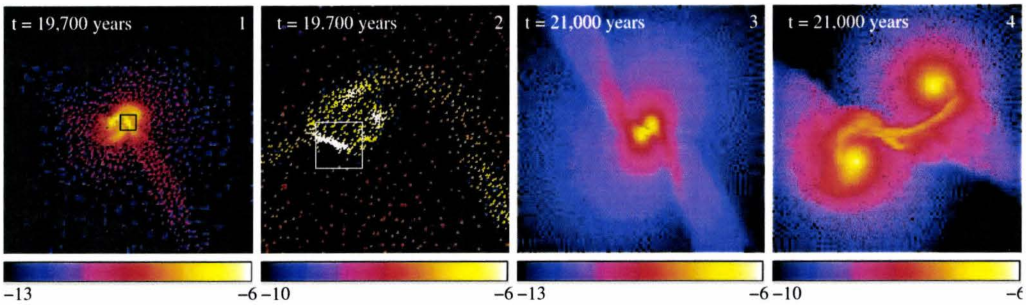

Figure 3.19 Disk encounter simulations with different disk models and resolutions. All the disks have Q = 1.3. The number of particles used to model the disk in panel 1 and 2 is 2000, while for 3 and 4 are 200000. The second and fourth panel shows the fragmentation region (or the inner region) for panel 1 and 3, respectively. The disk is razor-thin in the low resolution case. The color bar beneath each panel represents the density range in code units $M_\odot/AU^3$.

the shock layer fragmentation at about 100 AU from one of the stars (the boxed region in panel 2) at timestep 19700 years.

3.6 Heating and Cooling Rates

As described in Chapter 2, the simulations use a local isothermal equation of state (EOS), i.e., the temperature is a fixed function of position. This EOS requires that the disks have very efficient cooling, which is usually satisfied when the gas are optically thin. Taking $\tau_{crit} = 1$ as the critical optical depth beyond which the gas are optically thick, and assuming the gas opacity (for H_2) is $\kappa = 0.01\ cm^2/g$ at all wavelengths, the critical density between optical thin and thick gas can be estimated using

$$\tau = \kappa\Sigma, \tag{3.1}$$

where Σ is the disk surface density. Assuming $\Sigma \sim \rho H$, with H the disk scale height, equation 3.1 can also be written as $\tau \sim \kappa\rho H$. From Equation 3.1

the critical surface density can be obtained: $\Sigma_{crit} = 100.0\ g/cm^2$. With an assumption that the disk scale height is one tenth of the disk size, i.e., about 100 AU, the critical density can be calculated and it is $\rho_{crit} \sim 10^{-13}\ g/cm^3$. For the initial disk the critical surface density (or density) is not reached, since the peak surface density is less than 30.0 g/cm^2 (cf. Figure 2.1). However, during the encounter, significant amounts of gas are accreted onto the inner disk. If there are shock layers present the density would be even higher. Therefore, the inner disks are no longer optically thin. The cooling of the optically thick region is effectively by blackbody radiation. If the heating rate greatly exceeds the cooling rate then the local isothermal condition will be broken.

To verify the isothermal condition during the encounter, comparisons between cooling and heating rates were carried out at two different stages during the course of the encounter. In the first one the disks were moving close but had not undergone physical impact (6000 years in case 1), and the gas can be considered as optically thin. In the second case the disks were about to fragment (23000 years in case 1), in which both accretion and shock layer were very strong, and the gas of the inner region was optically thick. In the latter case, the highest density was above the critical density by two orders of magnitude ($\rho_{max} \sim 10^{-11}\ g/cm^3$). The calculations of heating and cooling rates were only in the inner region where $\rho > \rho_{crit}$.

The heating rates in both cases were calculated by running short test simulations with adiabatic equations of state (i.e., without cooling), obtaining the increments in thermal energies ΔE due to shocks, and dividing it by the simulation time Δt. The increase in thermal energy during a short adiabatic simulation can be calculated by

$$\Delta E = \frac{5}{2}k_B N_f T_f - \frac{5}{2}k_B N_i T_i, \tag{3.2}$$

where "i" denotes the initial stage and "f" denotes final stage of the short test simulation, k_B is the Boltzmann constant and N is the number of particles. A factor of 5/2 is used because, in previous assumptions, the disk models consist only of molecular hydrogen.

For optically thin case, the cooling rate can be estimated by

$$L_{thin} = \int_0^{\infty} 4\pi\rho\kappa_\nu B_\nu V d\nu, \tag{3.3}$$

where V is the volume of gas and B_ν is the Plank distribution of blackbody radiation. Assume the gas opacity κ is a constant for all frequency (grey opacity) and $\kappa = 0.01\ cm^2/g$, the above equation becomes

$$L_{thin} = 4\pi m\kappa\sigma T^4, \tag{3.4}$$

where m is the total mass of gas and σ is the Stephen-Boltzmann constant.

For optical thick gas, the cooling rate is simply calculated by blackbody radiation, i.e.,

$$L_{thick} = \sigma T^4 A, \tag{3.5}$$

where A is the area of the optical thick region.

The results for these comparisons are as follows. For the disks before impact, the heating rate was $(\frac{\Delta E}{\Delta t})_{thin} = 1.5 \times 10^{31}\ erg/s$ and cooling rate was $L_{thin} = 7.1 \times 10^{32}\ erg/s$. For the later stage when fragmentation was about to take place, the heating rate in the inner optically thick region was $(\frac{\Delta E}{\Delta t})_{thick} = 7.2 \times 10^{33}\ erg/s$ and cooling rate from blackbody radiation was $L_{thick} = 4.6 \times 10^{33}\ erg/s$. The values reflect that the heating rate rose quickly when the impact began and the gas became optically thick, but was still comparable to the cooling rate. So the local isothermal condition is still an acceptable EOS even during the physical impacts. More discussion on this will be continued in the next chapter.

Bibliography

Binney, J., & Tremaine, S., *Galactic Dynamics*, Princeton University Press, 1987

Lin, D. N. C., Laughlin, G., Bodenheimer, P., & Rozyczka, M. 1998, Science, 281, 2025

Stahler, S. W., & Palla, F. 2004, *The Formation of Stars* (2004 WILEY-VCH Verlag GmbH & Co. KGaA, Weinheim)

Watkins, S. J., Bhattal, A. S., Boffin, H. M. J., Francis, N., & Whitworth, A. P. 1998, MNRAS, 300, 1205

Watkins, S. J., Bhattal, A. S., Boffin, H. M. J., Francis, N., & Whitworth, A. P. 1998, MNRAS, 300, 1214

Whitworth, A. P., Chapman, S. J., Bhattal, A. S., Disney, M. J., Pongracic, H., & Turner, J. A. 1995, MNRAS, 277, 727

Chapter 4

Discussion and Implications

4.1 Effects of Toomre Q, Encounter Configurations and Velocities on Disk Fragmentation

4.1.1 Toomre Q

The first series of simulations in Chapter 3 revealed a clear trend towards decreasing degree of fragmentation with increasing value of initial minimum Toomre Q. From this trend one can expect that a disk with initial minimum Q higher than or equal to 1.3 would not fragment even if it underwent a strong impact. That is, in a dynamical interacting disk, there also exists a value of initial Toomre Q beyond which the disks can not fragment. As we will see in Section 4.2, this result is different from the previous studies of protostellar disk encounters, but it is not surprising: gas in a hotter but less massive disk would be easier to dissipate because of the higher thermal random motion and lower gravitational bounding energy.

Note that the values of Toomre Q parameters in the initial conditions only characterize the disk stability properties in the initial disks. During the encounter, the value Toomre Q evolves. Therefore, to explain the relation between disk fragmentation and the evolution of Toomre Q parameter, it is worth examining the Q parameters at the stages in which the disks are about to fragment. Since the outer disks are destroyed by physical impact and most fragmentation happens within disk radius 150 AU in the three encounters (case 1, 2, and 3), in this study only inner regions of the disks with $R < 150AU$ are included in the calculations. Figure 4.1 gives the radial profiles of Q parameters for initially Q_{ini} = 0.9, 1.1 and 1.3 disks at timestep 23000, 24600 and 23000 years, respectively. As discussed in Chapter 3, coplanar encounters produce shock layers which then connect the inner regions of the two interacting disks. In Figure 4.1, the presence of the shock layer in each case is broadly reflected by a dip in each plot of Q(r), because it increases the surface density in a confined region (Figure 3.3). Note that the dip does not reflect the width of the shock layer because the shock layer exists not as a ring with a certain radius but as a spiral which covers several radii of the disk. For initial Q = 0.9 disk the shock lies outside 150 AU so the dip in the curve is not obvious. From the figure, it is clear that for the disks with initial Q_{ini} = 0.9 and 1.1 (solid and dashed lines), the values of Q are lowered below 0.9 during the encounter, while for the Q_{ini} = 1.3 disk (dot-dashed line), the inner disk keeps Q > 0.9 though the high density region related to the shock layer in the disk has lowered local Q parameter significantly. Therefore, the real fragmentation criterion for an interacting disk is still around 0.9, similar to that of the isolated

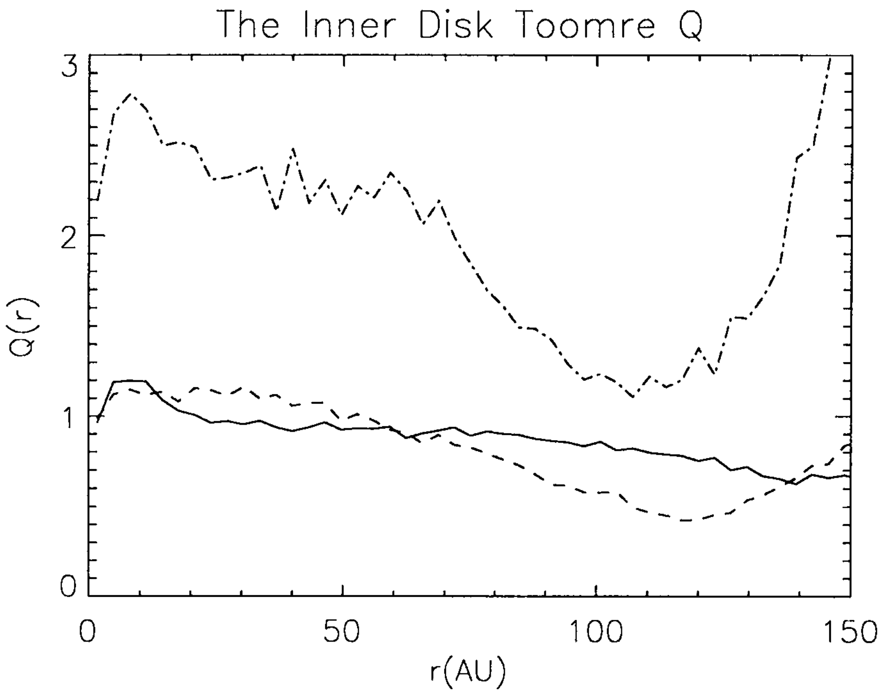

Figure 4.1 The radial profiles of the Toomre Q values in the inner disks during the retrograde-retrograde encounters (case 1, 2, and 3. *Solid line*: The initial condition has minimum $Q_{ini} = 0.9$, the plot is obtained at timestep 23000 years, and the shock layer lies out of 150 AU at this timestep. *Dashed line*: The initial condition has minimum $Q_{ini} = 1.1$, the plot is obtained at timestep 24600 years. *Dotted-dashed line*: The initial condition has minimum $Q_{ini} = 1.3$, the curve is obtained at timestep 23000 years.

disk. The encounter can lower the initial value of Q and destabilize the disk, which makes it possible for a $Q_{ini} > 0.9$ disk to fragment.

The evolution of Toomre Q in the inner disk can be explained as follows: In slow retrograde - retrograde encounter, disk material is dissipated due to dynamical heating as well as the pressure force along the impact section, but meanwhile it is also accreted onto the inner disk because of the loss of spin angular momentum during the encounter. Competition between these inward and outward motions determines the surface density and the evolution of the Toomre Q parameter of the inner disk. For a hotter disk the dissipation is faster than the accretion, and the inner disk density decreases, which means that the Toomre Q is increased. Therefore, a hot disk can be stabilized instead of being destabilized during the encounter. This can be seen in the $Q_{ini} = 1.3$ case in Figure 4.1, the average Q value is increased to around 2-3 after 23000 years of interaction.

Shock layers in the inner disks are also vital in disk fragmentation, because they significantly increase the surface densities in certain regions and hence decrease the values of Q. In the $Q_{ini} = 1.1$ case, it was the shock layer that reduced the inner disk Q value below the critical Q and induced disk fragmentation. For the marginal stable Q = 0.9 case, as shown in Figure 4.1, though shocks are not present within 150 AU, the increase in surface density by accretion has already lowered the Q in this region under 0.9. The inner disk therefore fragments quickly and forms many small clumps as demonstrated in Figure 3.3.

The above discussion concentrated on disk instability and fragmentation during the encounter. There is another mode of fragmentation to be considered. In the initial Q = 0.9 case the shock layer itself fragmented, but it did not happen in other two cases. In the shock layers, the competition between density growth and gas dissipation also exists: when the disks were close to the periastron, the disks' retrograde rotation helped develop a convergent velocity pattern between the disks, so the shock layer quickly increased its density. When the disks move apart, however, the shock layer broke and dissipated.

For locally isothermal gas, the Jeans Mass is the critical mass scale in fragmentation. Referring to Equation 1.1, the Jeans Mass M_J is proportional to c_s^3, but the sound speed c_s is proportional to square root of temperature, thus $M_J \propto T^{3/2}$. Therefore, with same density, gas is easier to collapse in a cooler disk because the critical mass scale is smaller. In the competition environments described before, the hotter shock layer in disks with $Q_{ini} = 1.1$ and 1.3 did not grow dense enough to form a clump before it dissipated, because the Jeans Mass is higher.

The disk with $Q_{ini} = 1.1$ corresponds to a disk with temperature $T \approx 13K$, slightly higher than the temperature of molecular cloud core $T \sim 10K$ (Stahler & Palla , 2004). For early extended disks which are still embedded in the envelope, the temperature should be close to the molecular cloud core if cooling is effective. Thus, the requirement $Q_{ini} \lesssim 1.1$ for a disk to fragment implies that the protostellar disks have good possibilities of fragment during encounters with other disks. However, for late stage disks which have higher temperature and less surface density, the probability of encounter induced fragmentation will be reduced.

4.1.2 Disk Configuration

Different configurations result in different evolution of disks and fragmentation mechanisms. Since basic process of each disk encounter case was described in last chapter, here I will only shortly summarize the differences and focus on the reasons of these differences.

4.1.2.1 Prograde Disk vs. Retrograde Disk

The difference between the behavior of prograde rotating disks and retrograde rotating disks are readily seen in the simulations. For retrograde ones, the encounters mainly enhance the inner disks accretion until the disks become unstable and fragment. The outer disks are truncated and the gas dissipates due to the strong physical impact. The interaction between the orbit and the disk spins does not cause large distortion of the disks, but always destabilizes the disks because of the initial destructive spin-orbit relation. Fragmentation is mostly due to the instabilities of inner disks, relevant to the decrease of Toomre Q parameters as analyzed in previous sections.

For prograde rotating disks, while physical impacts also destroy the outer part of the disks, the inner disks evolve in a different way. The prograde disks strongly respond to any perturbers by developing large "tidal tail" structures, no matter whether the perturbers are prograde or retrograde. (As shown in the simulations, the tidal tails developed in the prograde rotating disk in both "prograde-prograde" and "prograde-retrograde" encounters.) Usually each disk develops two tails, the one along the direction of the encounter connects to the tail from another disk, while the other extends outwards to up to thousands of AUs. The tails then grow in size and dissipate, inducing fragmentation by two different means. Firstly, if the disks' speed is not too fast, the growth of tails which connects two disks can compress the gas between two disks until it fragments. Secondly and more commonly, the tidal tails carry significant amount of angular momentum from the system, and thus induce spiral instabilities and fragmentation of the disks. Different from retrograde ones, the prograde disks do not accrete much gas during the encounters, but are usually severely distorted by the tidal tails. Moreover, because with the prograde configuration the spin and orbit vectors are constructive to each other, the disks are not always destabilized. In a fast encounter case, when the orbit has large angular momentum, the inner disks are in fact stabilized by the encounter, even if the tidal tails can carry part of the angular momentum from the system. Therefore, compared to retrograde disks, the prograde ones are more difficult to fragment, as demonstrated in the "prograde-retrograde" encounter case.

The development of tidal tail structures around a perturbed prograde disk is not a new phenomenon. It also happens in the prograde star-disk encounters (Clarke & Pringle, 1993) and the mergers of prograde-prograde galactic disks (Toomre & Toomre, 1972). The reason for this phenomenon can be explained by spin-orbit resonance. When the spin frequency at certain radius $\omega_{spin}(r) = \sqrt{GM/r_3}$ is equal to the orbit angular velocity, the material in the ring of that radius is in resonance and, as described in Binney & Tremaine (1987), for a retrograde disk, the material is "pulled alternatively inward and outward", so the net distortion is small; while for a prograde disk, the resonant material is "continuously pulled either inward or outward", hence the net response is large.

An interesting result related to the configuration is the formation of binary systems by star captures during the encounter. In Larson (1990), the author proposed that star-disk encounters may result in star captures and binary formation. But later work by Clarke & Pringle (1993) found that captures were not efficient in the star-disk encounters. Watkins et al. (1998a,b) then found in their simulations that disk-disk encounters could enhance the capture rates due to energy dissipation during the impacts. In the present work, there are two cases out of fourteen simulations in which star capture happened–the $Q = 1.3$ retrograde-retrograde coplanar encounter and the $Q = 0.9$ prograde-prograde non-coplanar encounter. The initial velocity of encounter is slow in both cases ($v = 0.4\ km/s$). In the former case (Figure 3.5) the disks are hotter and hence have a relatively high gas dissipation rate, and it is the dissipated gas that carries out the energy and angular momentum and induces the star capture. The latter case (Figure 3.14), on the other hand, produces large tidal structures which carry out most of redundant angular momentum. Though the retrograde encounter produces a closer binary system, the prograde encounter provides a more efficient way for binary formation: the binary formed within merely hundreds of years (panel 3 to panel 4 in Figure 3.14), much faster compared to the retrograde encounter which took about 4000 years.

4.1.2.2 Coplanar vs. Non-Coplanar

It is now clear that coplanar encounters are very likely to produce strong shock layers regardless the disk configuration. As will be discussed in detail in Section 4.4.3.1, fragments formed from the compressed shock layers usually have high velocities (even in the vertical direction) and are not bound to the star. Hence they are likely to become field substellar objects. In the non-coplanar cases the compressed-gas regions still form, but are not confined to layers, and there is no fragmentation related to shocks.

Case	Name	Velocity (km/s)	Number of Clumps	Fragmentation Mechanism
9	Q09_pp45_4e4	0.4	1	Circumbinary Disk Fragmentation
6	Q09_pp45_1e5	1.0	3	Tidal Tail + Disk Fragmentation
10	Q09_pp45_2e5	2.0	0	
11	Q09_pp45_3e5	3.0	0	
1	Q09_rrco_4e4	0.4	8	Shock Layer + Disk Fragmentation
4	Q09_rrco_1e5	1.0	2	Disk Fragmentation
12	Q09_rrco_2e5	2.0	2	Disk Fragmentation
13	Q09_rrco_3e5	3.0	0	

Table 4.1 Number of fragments in simulations with different encounter velocities.

Also, as shown in the simulations, in non-coplanar encounter cases, the disks which are not within the orbit plane are more unstable and easier to fragment. This can be seen most obviously in the prograde-prograde perpendicular encounter: there were 4 clumps formed in the disk which was perpendicular to the orbit plane, but none formed in the other. In reality, non-coplanar disk encounters are the majority of the encounters, and it is very possible that neither of the disk planes coincide with the orbit plane. Since in this study at least one of the disks is in the orbit plane, it can be expected that in reality the number of fragments would be larger.

4.1.3 Encounter Velocity

The third series of simulations in the previous chapter showed that the number of fragments changes with the encounter velocity. The numbers of fragments by the end of the simulations are listed in Table 4.1.

In this series, the slow prograde-prograde encounter (case 9) is a special case, since the stars captured each other quickly after periastron and produced a very close binary system. In all other encounters, the two stars were moving away after the impacts and most of them still possessed small disks with radii about a few hundred AU. Despite this difference, a broad trend towards smaller numbers of clumps with increasing encounter velocities is still clear in Table 4.1. Fragmentation of tidal structures (prograde-prograde non-coplanar encounter) and the shock layers (retrograde-retrograde coplanar encounter) only happened in the slow cases with $v \leq 1.0\ km/s$. This is because, for both tidal structures and shock layers there exists a competition between local density growth and gas dispersion, and it requires a certain time for any of these structures to grow dense enough and fragment. So, when the two disks move apart fast, the structures will dissipate before any condensation can happen.

The number of clumps from disk fragmentation also decreases in fast encounters, and there is no fragmentation for either prograde or retrograde configurations when the velocities are as high as 3.0 km/s. Disk fragmentation is a highly non-linear process and it is hard to exactly predict how many clumps will form. However, the disk instabilities are triggered by the encounter, and the timescale of the encounter determines the timescale of the disks under effective spin-orbit and disk-disk interaction. Thus it is helpful to compare the timescale of encounter and a disk's dynamical timescale at certain radius, i.e., the orbital time for gas material in the disk at that radius. The encounter timescale can be defined as:

$$t_{encounter} = \frac{D_{eff}}{v}, \tag{4.1}$$

where D_{eff} is the distance of the encounter trajectory where the physical impact between disks took place, and v is the velocity of the star-disk system during the impact. Assuming that the stars move with a constant speed during the physical impact, and taking the impact speed the same as the initial disk speed and D_{eff} approximately twice the disk diameter (i.e., 4000 AU), the estimated numerical values of encounter timescales for v = 0.4, 1.0, 2.0, and 3.0 km/s encounters are 4.7×10^4, 1.9×10^4, 1.0×10^4 and 6.3×10^3 years, respectively.

The disk dynamical timescale at each radius can be estimated as the orbital period of the gas material at that radius, i.e.,

$$t_{dyn} = \frac{2\pi r}{\sqrt{\frac{GM_*}{r}}}. \tag{4.2}$$

Here G is Newton's Gravitational Constant and M_* is the mass of the star. The orbit motion of gas has been assumed to be Keplerian since it is a good approximation for most inner disks. The radius is taken to be 400 AU in estimating the value of t_{dyn}, because during most encounters the disk material outside this radius underwent physical impact and dissipated. Using $M_* = 0.5M_\odot$, the dynamical timescale is 1.1×10^4 years. Comparing to the value of the encounter timescale in each case, it shows that only when $t_{encounter} \gtrsim t_{dyn}$ is satisfied, strong fragmentation of disks can be triggered. In other words, interaction in fast encounters does not last long enough to effect the disk structure evolution.

Equation 4.2 and the timescale constraint for disk fragmentation implies that it would be easier to induce disk fragmentation for encounters with smaller impact parameters, since inner disks have shorter dynamical timescale. However, as discussed in the first chapter, the frequency of small impact parameter encounters ("head on" encounters) is very small. In the real world, the velocity dispersions of deeply embedded early groups of protostellar disks are not completely determined. For star clusters or groups, the velocity dispersions are about several km/s. For example, Taurus-Auriga stars have velocity dispersion 2-3 km/s (Stahler & Palla , 2004). The velocity dispersion should also differ with environments. For example, dense clusters would generally have higher velocity dispersions than small loose star groups. Since mutual interactions of stars and disks during the star formation process usually increase the velocity dispersion (Bate et al., 2003), it could be expected that velocities of early embedded objects are lower than fully-formed stars. So, it is reasonable to assume that the dispersions of early groups are around 1 km/s. Moreover, the encounter velocity is the relative velocity between the two disks, and it can be significantly less than the velocity dispersion if the disks are moving in a same direction. Therefore, there are still many possibilities for the impacts of protostellar disks to induce fragmentation.

4.2 Comparisons with Other Work

4.2.1 Previous Studies of Protostellar Disk Encounters

Previous studies by Watkins et al. (1998a,b) carried out a series of protostellar disk encounters with different configurations and impact parameters. In their work the disks were also massive (0.5 $M_{\odot}$) and extended (1000 AU), but had higher initial Toomre Q parameter: Q = 2.4. The simulation also used SPH method for gas dynamics and N-body for gravity calculations, and disks were modeled with single layers of 2000 particles. An isothermal equation of state with a uniform temperature was applied during the whole simulation. Both coplanar and non-coplanar encounters were studied. In the coplanar encounter simulations, the shock layers fragmented soon after the impacts began. Later, disk instabilities were triggered and more fragments formed quickly regardless of the spin-orbit configuration. In non-coplanar cases, shocks did not form but disk instabilities and fragmentation were still triggered by the encounters.

While also producing fragments during the encounter, the results of the current study differed from the previous one by Watkins et al. (1998a,b) in two key aspects. First and foremost, fragmentation was prevented as Toomre Q increased in this study, and did not happen when initial Q was merely 1.3, but in previous studies the encounter produced large numbers of clumps when the disk Q parameter was 2.4. Secondly, in the coplanar encounters in this study, fragmentation of the shock layer did not take place until the layer obtained a significant amount of mass, while in previous studies it fragmented soon after it formed, and the shock layer fragmentation contributed significant numbers of clumps in every coplanar cases.

Another SPH simulation of a disk-disk encounter was carried out by Lin et al. (1998). In their study, the two disk spins were perpendicular to each other but both had prograde rotation, and one of them was in the orbit plane. The system was initially bound. Their disks were smaller (around 250 AU) than the ones in this study, but still massive (0.4 $M_{\odot}$). The inner 100 AU disk, together with the star, was represented by a single particle. The outer disk from 100 AU to 250 AU was modeled with 8000 gas particles. An adiabatic equation of state was used for $R < 250\ AU$ measured from the star, but for the region beyond 250 AU an isothermal EOS was applied. The disk lying in the orbit plane produced a large tidal structure, which extended outwards to about 1000 AU. Condensation then happened in the structure and formed a clump with 7 Jupiter Masses (0.007 $M_{\odot}$). The gas in the rest of the tail had a divergent velocity pattern and was likely to dissipate and leave the clump with substellar mass.

Comparing to the work by Lin et al. (1998), the prograde encounters in current study also had very large tidal tails which grew in size and extended outwards. However, fragments formed mostly from the inner disk or the tidal structures connecting two disks (as in case 6), but not from the outer extended tidal tails. As shown in the simulation results in Chapter 3, especially in the perpendicular encounter in Section 3.4, the density of the tidal tail structures in prograde disks was continuously decreasing with time (e.g., Figure 3.10, 3.12, 3.15), and finally became very low. (The density can be lowered by two orders of magnitude, as in Figure 3.17). The dissipation of tidal tails did not seem to change much by the special perpendicular configuration.

4.2.2 Effects of Resolution and Disk Scale Height on Fragmentation

The discrepancies between this study and previous ones may result from more than one reason. For example, the adiabatic equation of state (EOS) used in the inner disk in the work by Lin et al. (1998) may have prevented the fragmentation in that region. Another possibility is that the low resolution enhanced the shock layer fragmentation, as in the study by Watkins et al. (1998a). In this section, discussion will focus on the effects of the resolution on fragmentation and the importance of resolving the disk scale height. The validity of EOS before and during the encounter will be discussed in next section.

Studies by Bate & Burkert (1997) suggest that resolving the Jeans Mass is vital to correctly model fragmentation. For SPH simulations, a minimum number of particles $N \sim 2N_{neighbor}$ is required to resolve the local Jeans Mass, where $N_{neighbor}$ is the number of neighboring particles in SPH simulation. If this requirement is not satisfied, the fragmentation will be artificially enhanced or prevented, depending on the implementation of SPH in the code. As calculated in Chapter 2, for the initial conditions in this study, about 10^4 particles are required to resolve the the Jeans Mass down to the smallest scale (i.e., the region where the density is the highest). As the simulation of the encounter goes on, the formation of the shock layer, the inner-disk accetion, and the tidal structures all increase the local density and hence decrease the local Jeans Mass. Thus, higher resolution becomes necessary to follow these processes. Moreover, when fragmentation happens, the local density can suddenly increase by several orders of magnitude. For example, one of the clumps in case 6 has mass 0.07 solar masses but has size less than 1 AU, assuming the clump to be spherical gives mean density around 10^{-8} g/cm^2, which is 10^5 times larger than the highest density in the initial condition. Therefore, to correctly follow the encounter and fragmentation, the resolution requirement should significantly higher than the initial condition requirement. The resolution in previous studies, however, either did not meet the requirement (2000 particles), as in Watkins et al. (1998a,b), or marginally met the requirement for the initial condition (8000 particles), as in Lin et al. (1998). Thus, it is very likely that some of their fragmentation occurred artificially.

The other factor which can affect the disk instability and fragmentation is the modeling of the vertical disk structure. As concluded in the work by (Kim et al., 2002), disk models with resolved finite scale heights are more stable than 2D disk models. Since real disks always have finite scale heights, the simulations which do not model the vertical structures of the disks may also destabilized the disks artificially. Moreover, during the encounters, regardless of whether they are coplanar or non-coplanar, the gas motions are not always confined to the disk plane. Hence, correctly modeling the disk thickness becomes very important in obtaining the right behavior of the gas with vertical velocity components. Last but not least, as discussed in Chapter 2, SPH is fundamentally a 3D scheme. Therefore, the forces calculated in SPH for a 2D disk can be incorrect from the beginning of the simulation. The above three reasons were the motivation for the efforts in constructing the vertical disk model in this study.

The simulations in Section 3.5 were designed to demonstrate the effects of the above two factors. As shown in the calculation of Jeans Mass, for a disk as large as this study, 10^4 particles are required to resolve the Jeans Mass in the initial condition. So 2000 particles simply can not resolve the Jeans Mass from the beginning, hence it is not surprising that the first simulation of isolated disk evolution in section 3.5.1 produces two artificial fragments in less than one dynamical timescale. The use of 20000 particles marginally satisfied the resolution requirement. However, since the razor thin disk model is more unstable than the one with resolved finite thickness, the second simulation in Section 3.5.1 also results in fragmentation in a Q = 1.3 disk. This explains why disks which have Toomre Q as high as 2.4 can produce lot of fragments.

The simulations of disk fragmentation in dynamical encounters in Section 3.5.2 indicates that disks modeled with low resolution without resolving the scale heights will induce fast fragmentation of shock layers. Though not identical, the result of fast shock layer fragmentation is similar to the ones in Watkins et al. (1998a) (compare panel 1 in Figure 3.19 and the second panel in Figure 1 of Watkins et al. (1998a)).

4.3 The Heating and Cooling During the Encounter

All the simulations in this study used the locally isothermal equation of state, which greatly simplified the numerical calculations. The test simulations in Section 3.6 show that the local isothermal EOS is a good approximation before the disk impact, since the cooling rate at this stage is larger than the heating rate by a factor of ten. However, the situation is different for the later stage when the disk is about to fragment. At the late stage, strong accretion has made the disk optically thick. The highest density is $\sim 10^{-11}$ g/cm^3, exceeding the critical density by two orders of magnitude. A shock layer has formed and strong spirals have also developed in the disk and the heating rate in this optically thick region hence increases rapidly. Nevertheless, the cooling rate calculated by assuming blackbody radiation is still comparable to the heating rate, indicating that the locally isothermal condition is still acceptable.

The study of cooling and heating rates chose a retrograde coplanar encounter as the test simulation case for two reasons: firstly, a retrograde encounter usually induces more accretion onto the inner disks than a prograde one, so that the disk density quickly rises above the critical density $\rho_{crit} \sim 10^{-13}$ $g\ cm^{-3}$, and the gas becomes optically thick. Secondly, the coplanar configuration induces formation of shock layers which heat the disk significantly. Thus, the retrograde coplanar configuration should have a relatively higher heating rate compared to others. Therefore, if the locally isothermal condition is valid for the retrograde coplanar encounter, it will also valid in other encounters.

This comparison is back-of-the-envelope because many factors such as the disk geometry and the existence of dust can all affect the cooling rate significantly. The inclusion of these factors and the exploration of the thermal regulation of the disks will be part of future work.

4.4 The Properties of Resultant Fragments and Observational Implications

Except for high Q disks and fast encounters, most simulations in this study produced fragments. The fragments can form from shock layers (case 1 and 5), tidal structures (case 6) and disk instabilities (all the cases except the ones which do not fragment at all). Since disk encounters happen in a much shorter timescale compared to the lifetime of stars or substellar objects, they are rarely observed in the real world. Thus the compact objects formed from the encounter may be of more interests in observational studies than the encounters themselves. Numerical simulations, on the other hand, can not follow the encounters after the clump formation because the timescale coverage from the collapse of the gas material to the full formation of the object is too large for current computers to handle. Therefore, the analysis of clumps and their further evolution is very important in connecting the theoretical models to the observational data. This section will focus on studies of fragments, their statistical and morphological properties, their further evolution, and the related observational implications.

The sample used in analyzing the fragments evolutions consists of all the clumps formed in $Q = 0.9$ disk encounters. There are 32 fragments in total. The basic properties of each fragment such as mass, size, spin orientation and orbit eccentricity etc., are listed in Table 4.2.

ID	Encounter	Mass (M_J)	Size (AU)	Spin orientation (Degree)	Bound y/n	Eccentricity	Semi-Major Axis (AU)
1	rrco_4e4	32.5	0.26	166.2	y	0.36	13.8
2		31.3	0.28	171.3	y	0.18	4.7
3		10.2	0.69	122.5	y	0.52	19.1
4		19.9	1.35	102.6	n		
5		14.3	0.45	171.6	n		
6		12.3	0.40	176.2	y	0.64	98.6
7		9.6	0.89	168.6	y	0.03	26.8
8		5.4	10.53	174.1	y	0.91	879.3
9	rrco_1e5	61.6	2.47	170.7	y	0.55	57.0
10		10.4	1.75	174.0	y	0.41	44.5
11	rrco_2e5	30.0	0.51	178.3	n		
12		27.5	0.45	177.6	y	0.78	24.9
13	ppco_1e5	73.5	0.27	8.9	n		
14		25.4	0.22	13.5	n		
15		32.6	0.35	12.4	n		
16		6.8	0.23	40.4	n		
17		15.7	0.21	13.7	n		
18		2.5	0.14	13.5	n		
19		5.5	0.54	18.7	n		
20	pp45_4e4	19.2	6.65	30.9	y	0.43	123.2
21	pp45_1e5	69.6	0.31	121.8	y	0.07	86.9
22		19.2	2.50	69.4	y	0.90	532.4
23		8.9	9.08	72.3	y	0.44	307.3
24	pr45_1e5	21.7	0.43	165.6	y	0.73	64.2
25		18.5	0.45	168.6	n		
26		23.7	2.03	164.7	y	0.31	51.5
27	rr45_1e5	21.1	2.74	126.5	y	0.26	42.3
28		11.9	5.87	166.8	y	0.26	70.0
29	pp90_4e4	17.1	0.98	73.1	y	0.54	53.9
30		12.3	1.28	59.4	y	0.92	32.8
31		1.85	0.50	107.9	n		
32		8.27	11.85	90.6	y	0.21	154.4

Table 4.2 Some properties of the fragments. The “Spin orientation” means the angle between the spin of the clump and the encounter orbit plane. Here “Bound” means the clump is bound to the star. For all the bound clumps the eccentricities and semi-major axes of their orbits are listed.

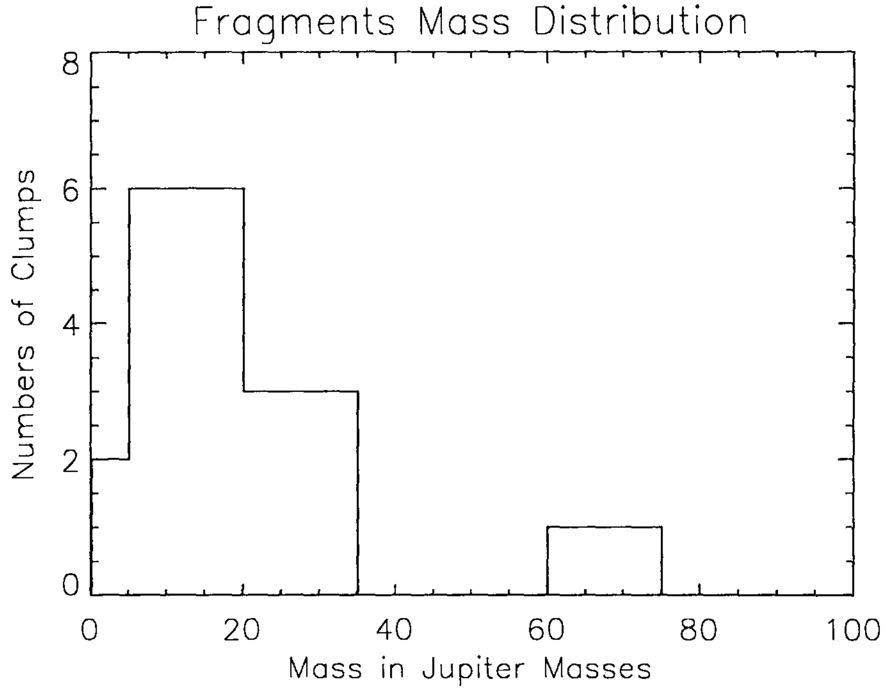

Figure 4.2 The mass distribution of resultant fragments from all the simulations. The binsize is 5 Jupiter Masses (0.005 $M_{\odot}$).

4.4.1 The Mass and Mass Distribution of the Fragments

The mass range of the fragments is from 0.0019 $M_{\odot}$ to 0.073 $M_{\odot}$. The mass of the most massive clump is still below the hydrogen burning limit 0.075 $M_{\odot}$, i.e., the fragments are all in the substellar region. Any fragment which survives in the further evolution and does not accrete significant mass will then become a substellar object (a brown dwarf or a planet). The mass distribution of the clumps with bin size 5 Jupiter Masses (0.005 $M_{\odot}$) is plotted in Figure 4.2.

The plot shows that generally the number of fragments decreases with increasing mass, which is broadly consistent with the trend in the substellar initial mass function. For example, observations of brown dwarfs in Pleiades

(Figure 4.3) show that the initial mass function from stellar to substellar region can be well represented with a power law of $dN/dm \sim m^{-\alpha}$, with an index $\alpha = 1.0$ (Martin et al., 1998). Note that the range of their plot covers both substellar and stellar regions and does not have data below 30 M_J. The mass range in this work, however, favors the low mass end below 30 M_J and does not reach the stellar region. Nevertheless, the linear χ^2 fit (dashed line in Figure 4.4) also gives index -1.0 ($\chi^2 = 0.056$). The fit does not include the first two bins which have mass less than 10 M_J, because the simulations are likely to underestimate the number of clumps in this region due to the softening of gravity.

The lack of population in 35-60 M_J is a notable feature in Figure 4.2. The total distribution is separated into two regions-low mass region (0-30 M_J) and high mass region (60-75 M_J). The physical reason for this gap is not clear. It could be related to fragmentation mechanisms of the clumps, since the 3 high mass brown dwarfs are all from encounters in which shock layers or tidal structures are very strong (case 4, 5, and 6). It could also result from the low number statistics of this study. A larger sample is necessary to address this question.

Also, in Figure 4.2 the mass distribution peaks around 10 M_J and decreases at the Jovian mass region. However, observations have discovered a large number of extrasolar planets with masses around M_J or less (e.g., Wright et al., 2005). This discrepancy may indicate that scenarios other than fragmentation contribute more to the planetary object formation. But it can also result from the numerical gravitational softening. As described in Chapter 2, in

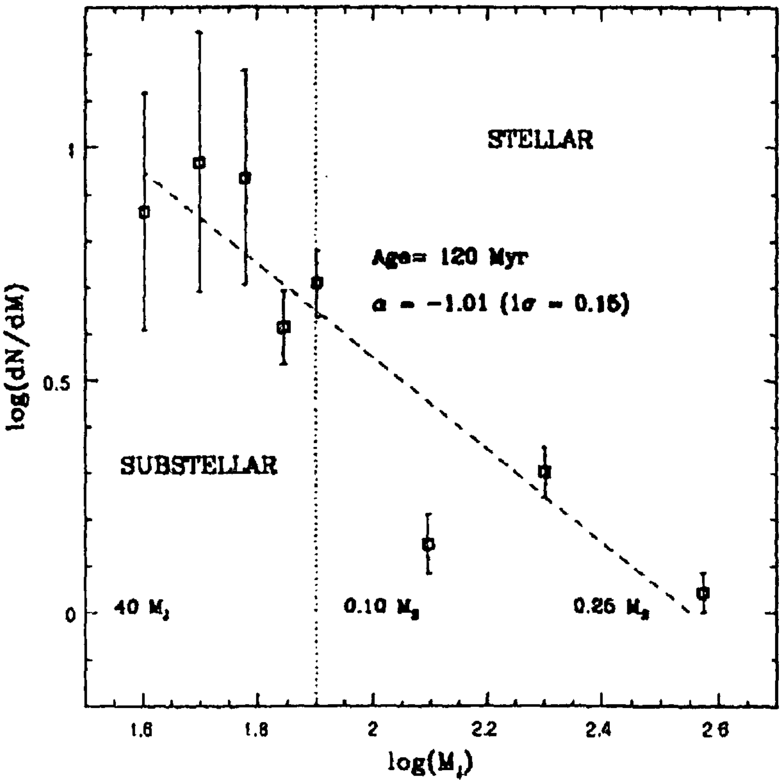

Figure 4.3 The initial mass function in Pleiades from stellar to substellar regime. The dashed line is a power law with an index $\alpha = 1.0$. Adapted from Martin et al. (1998), Figure 2.

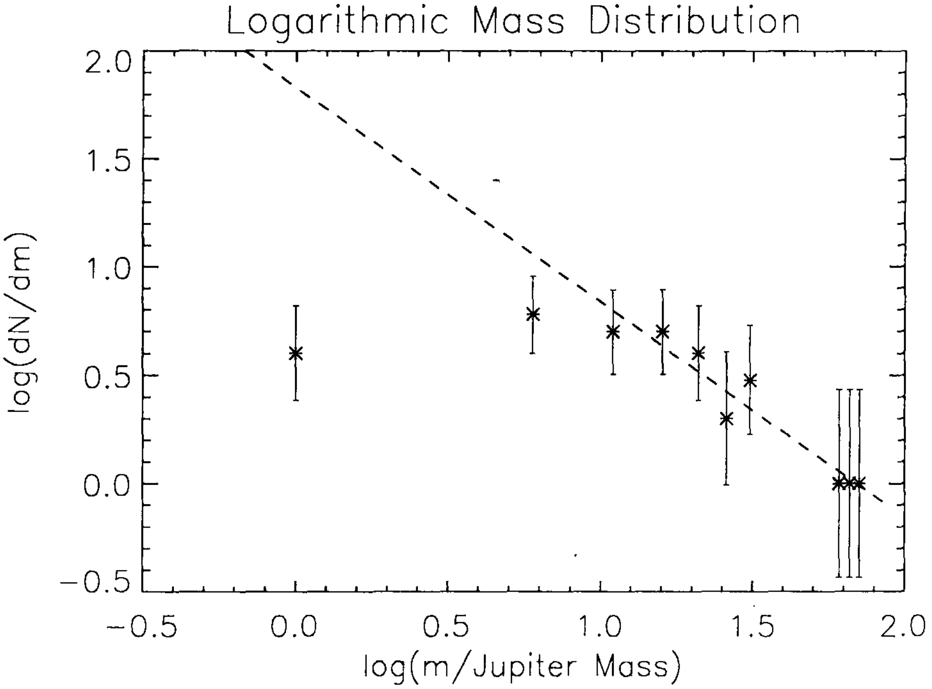

Figure 4.4 The logarithmic mass distribution of the fragments, $\log(dN/dm)$ versus $\log(m)$. The error bars were calculated using $\sigma = 1/\sqrt{dN/dm}$ and propagated to logarithmic space. The masses are in units of M_J. The dashed line shows the χ^2 linear-fit of the data, with the first two data points excluded. The slope is -1.0, i.e., $dN/dm \sim m^{-1.0}$. This is the same as the initial mass function in the substellar-stellar boundary in Pleiades cluster (Martin et al., 1998).

the simulation the gravity is softened by a spline function at radius $R \leq 0.2 AU$. Because of this, the gravitational forces between very close particles are artificially reduced, and clumping in small regions may be eliminated. Hence, the gravitational softening may have artificially prevented small mass formation.

4.4.2 The Shape of the Fragments and Observational Implications

The typical shape of the resultant clumps from the encounters is shown in Figure 4.5. The fragments are not spherical dense objects as one usually imagines, but have highly flattened, disk-like shapes. The sizes of clumps listed in Table 4.2 are actually the radii of the disks, and the disks' heights are approximately 1/10 of their radii. The formation of disk-like clumps is consistent with recent observations, which found that $\sim 65\% \pm 15\%$ of the brown dwarfs exhibit IR excess , indicating disks around them (Muench et al., 2001).

The values of disk sizes listed in Table 4.2 show that most of the disks are small, since only about 1/3 of the disks are larger than 1.0 AU and only 2 out of 32 clumps have disks larger than 10.0 AU. This result explains why the study of stellar cluster formation by Bate et al. (2003) did not obtain many brown dwarfs with disks, because their minimum resolvable length scale was 10 AU. However, Bate et al. (2003) argues that the viscous timescale for a disk with $R \ll 10\ AU$ is very small hence the disk is unlikely to be observed.

The fragments possess large angular momenta, especially those with relatively big disks. Assuming that the angular momenta of the clumps are con-

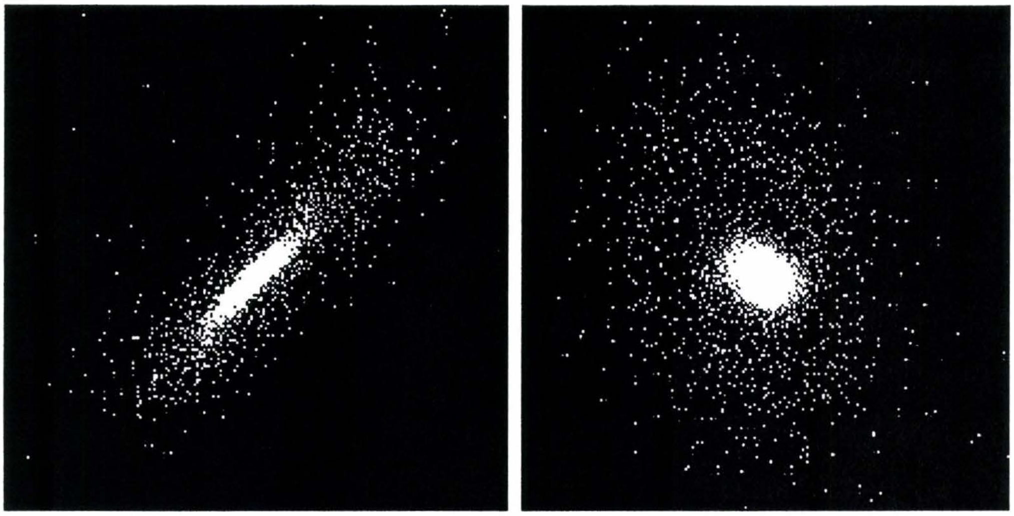

Figure 4.5 Disk-like fragment formed from the encounter. *left*: A clump formed in the case "Q09_rrco_4e4" viewing along z axis. *right*: The same clump viewing along y-axis.

served during their further evolution, and taking the final radii of the objects close to the observed radius of the brown dwarfs $R \sim 7 \times 10^9\ cm$ (Burrows et al., 1998), one can estimate the angular velocities of the final objects. It turns out that the rotational velocities at the outer edges of these objects exceed the break up velocities by more than a factor of 10. This indicates that in the further evolution, the clumps will have to lose most of their angular momenta.

One possible way to release angular momentum from the disk is via bipolar jets or outflows, which implies that it is possible to observe jet-like structures in brown dwarf disks. The observation of such structures in brown dwarf disks has been made possible by the emerge of high angular resolution telescope such as the Hubble Space Telescope (HST) (Bacciotti et al., 2005).

Another possible way is that, similar to the planet formation, a companion object forms inside the disk, and orbits around the young brown dwarf, holding the majority of angular momentum of the system. The companion can be either a planet or another brown dwarf with comparable mass, in the latter case the two objects orbit around each other and form a close binary system. While close binaries are frequently discovered (Martín et al., 2000), the observation of planetary companions of young brown dwarfs became possible only very recently. Nevertheless, an object has already been found as a companion to a brown dwarf in the TW Hydrae Association, which is very likely to be a giant planet (Schneider, 2005).

The angles between spins of the clump disks and the encounter orbit planes ("spin orientations") are also listed in Table 4.2. Most of the clumps keep the same spin-orbit relations as their parent encountering disks, i.e., clumps usually have prograde spins if they form from prograde disks and retrograde spins if they are from retrograde disks. However, most spin vectors of the fragments are not exactly coincident with the ones of the original disks, but tilted by angles even in the coplanar encounters. For clumps formed from retrograde disk encounters, including the non-coplanar "rr45_1e5" and "pr45_1e5" configurations, the angles are usually small and less than 20 degrees, with exception of fragment 3 and 4, whose formation were strongly affected by the shock layer. On the other hand, clumps from prograde disks are likely to be tilted by large angles, especially in the non-coplanar encounters. Moreover, in the case "pp45_4e4" where a binary system formed, the entire circumbinary disk has spin orientation about 20 degrees, a value lies in between the spins of two original disks, as shown in the last panel of Figure 3.14. These significant changes of spin vectors in both the fragments and the circumbinary disk reflect that there were strong spin-orbit resonances during the encounters for prograde rotating disks. It also implies that a random distribution of disk orientation is most likely to be observed for both brown dwarf disks and protostellar disks.

4.4.3 The Further Evolution and Fate of the Fragments

4.4.3.1 Dynamic Evolution of the Fragments in the System

Figure 4.6 shows an example of the orbits of the resultant clumps. There are bound (to the star) objects which have elliptical orbits (solid lines) and unbound (to the star) objects with parabolic or hyperbolic trajectories (dashed lines).

As indicated in Table 4.2, approximately one third of the fragments formed in this study are not bound to the system. The percentage is higher if only coplanar encounters are considered, since the shock layer fragmentation would take place relatively far from the potential field of the inner disks and the stars (e.g., the fragmentation in the "ppco_1e5" encounter). It is still possible for these unbound fragments to lose their mechanical energy due to the interaction with the environment, migrate inwards and finally become companions to the stars, or even accrete onto them. However, as shown in most of the simulations, strong dispersion of gas always exists during the encounter and competes with the inflow motion due to accretion. In this dissipative environment, as long as the unbound fragments do not lose too much energy and migrate inwards too fast, they are likely to leave the inner dense region and finally become free floating brown dwarfs. Also, there is a case (Fragment 16 in Table 4.2) where

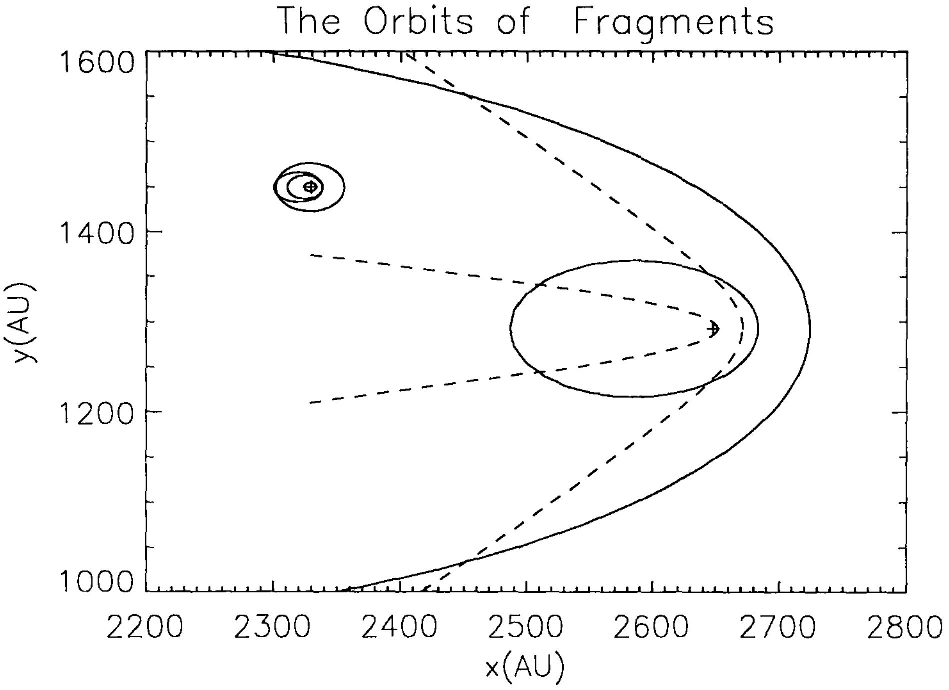

Figure 4.6 The orbits of the fragments formed from the slow retrograde-retrograde coplanar encounter (case 1). The orbit calculation for each clump only takes into account the gravitational potential generated by the star which is closer to the clump. Effects of viscous gas and perturbations by other orbits are not considered. Trajectories of unbound objects are indicated by dashed lines.

the fragment acquired large velocity in the z-direction $v_z \sim 1.8\ km/s$ during a coplanar encounter. The reason for the high velocity is that the pressure increased quickly in the "head on" encounter and pushed the gas in the shock layer along z direction. In this situation, the unbound clump is very likely to leave its parent disk since the gas motion of the parent disk is mostly confined to the x-y plane, and the energy exchange between the clump and surrounding gas is expected to be small.

Objects which are bound to the stars comprise two thirds of the total clumps. Again, some of them will finally accrete onto the star, but if any clumps survive the inwards migration, they may become substellar companions to the stars. The eccentricities and semi-major axes of their orbits are listed in Table 4.2. As indicated from the values of semi-major axes, the rate of close brown dwarf companion with separation $< 3\ AU$ is low (0 out of 32). This is consistent with observational "brown dwarf desert" which states that brown dwarfs are rarely observed as close companions with $R < 3\ AU$ to F-M0 main sequence stars but frequently observed in the field (Marcy & Butler, 2000). Several orbits have large semi-major axes $R > 500\ AU$ but the objects are still bound, as the one plotted in Figure 4.6. Because the orbits are big and reside in the outer dissipative region, they are unlikely to be significantly affected by the interaction with other orbits or the accretion inflow of gas materials. Hence, these objects may remain as wide-separation brown dwarf companions, whose existence has already been confirmed by some observations (Gizis et al., 2001).

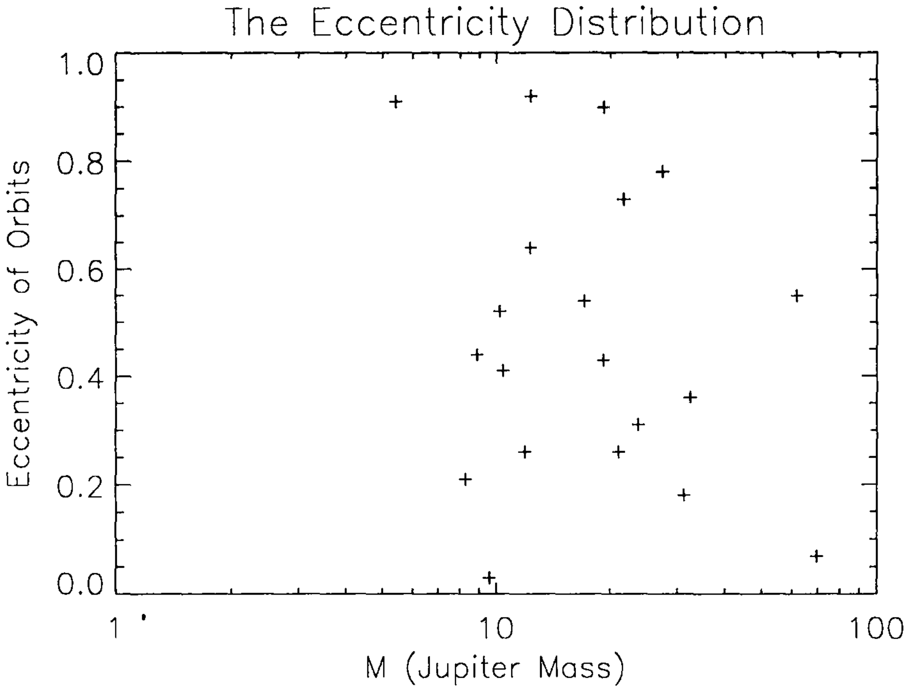

Figure 4.7 The eccentricity-mass distribution of the bound fragments.

The distribution of orbital eccentricity versus clump mass is plotted in Figure 4.7. The average eccentricity of the orbits is $\bar{e} = 0.47$ with dispersion $\sigma = 0.27$. The distribution and average value of eccentricity are similar to those of the observed brown dwarf companion eccentricity distribution by Mayor et al. (1998) (compare Figure 4.7 with their Figure 5). In the work of Mayor et al. (1998), they also observed eccentricity of planetary mass objects and found that there was a clear discontinuity in the eccentricity distribution around $3-7M_J$, because most of their observed planetary companions with mass less than $5M_J$ have quasi-circular orbits while brown dwarfs have highly eccentric ones (this may not be exactly true since quite a few of recently observed exosolar planets have highly eccentric orbits). In this study the data of planetary objects are not enough, and the few clumps which have mass less than $7M_J$ are either unbound or have large eccentricity. Note that the mass of the clumps may not be the same as the mass of the final objects. The fate and final properties of the clumps are closely related to whether or not accretion onto the clumps can be stopped , which will be discussed in the next section.

4.4.3.2 Accretion vs. Ejection

As mentioned in the introduction, Reipurth & Clarke (2001) first propose the ejection scenario which states that brown dwarfs form from the fragmentation of molecular cloud cores and are ejected out of the system so that they can keep the mass in substellar region. This scenario is then used to explain the lack of wide brown dwarf binaries and the "brown dwarf desert". Simulations of core collapse by Bate et al. (2003) then find that fragmentation of protostellar disks is the major reason for brown dwarf formation, and ejection can happen in their simulations. However, most of the ejected brown dwarfs do not have disks. Observations, on the other hand, find that $\sim 65\% \pm 15\%$ of the brown dwarfs have disks (Muench et al., 2001), and the existence of wide-separation brown dwarf binaries (Luhman, 2005) indicates that a 100% ejection scenario can be incorrect.

The simulations of protostellar encounters in this work produced a significant percentage of unbound fragments, some of which even have high vertical velocities. These clumps will easily leave the system and halt accretion. Ejection of bound clumps are also possible, especially in multiple systems. As shown in Figure 4.6, an orbit in a multiple system often intersects with others, which would induce the gravitational scattering effect when the the objects are close to each other. And this will cause ejection. If any ejection happens, the dense, fast-spinning disk-like object is likely to be ejected as a whole. Therefore, the observational fact that disks surround most of the young brown dwarfs does not conflict with the ejection scenario. And as discussed before, the no-disk brown dwarf result in Bate et al. (2003) is mainly because the scale under 10 AU is not resolved in their simulations.

On the other hand, some results in this work also imply that ejection is not necessarily required for a clump to stop accreting mass. Firstly, for a clump with a large orbit, it lies in the dissipative outer region. The dispersion of gas will then effectively prevent the gas from accreting onto the object. Secondly, even for a disk-like object in the inner, dense region of its parent disk, as long as it spins fast, the gas can not accrete directly onto the center of the object, but only onto the outer edge of the disk. Hence the disk will grow in size quickly, but since the object (with the growing disk) is orbiting around the parent disk, and its spin direction is likely to be similar as its parent disk's, a smaller-scale prograde-prograde interaction will then take place. Significant amount of mass from the object will hence be carried out by tidal tails, leaving the objects in the substellar region. These two scenarios help prevent the substellar objects from accreting mass but more simulations should be designed in the future to test these ideas.

Bibliography

Bacciotti, F., Ray, T. P., Eislöffel, J., Woitas, J., & Coffey, D. 2005, Memorie della Societa Astronomica Italiana, 76, 366

Bate, M. R., Bonnell, I. A., & Bromm, V. 2003, MNRAS, 339, 577

Bate, M. R., & Burkert, A. 1997, MNRAS, 288, 1060

Binney, J., &Tremaine, S., *Galactic Dynamics*, Princeton University Press, 1987

Burrows, A., et al. 1998, ASP Conf. Ser. 134: Brown Dwarfs and Extrasolar Planets, 134, 354

Clarke, C. J., & Pringle, J. E. 1993, MNRAS, 261, 190

Gizis, J. E., Kirkpatrick, J. D., Burgasser, A., Reid, I. N., Monet, D. G., Liebert, J., & Wilson, J. C. 2001, ApJ, 551, L163

Kim, W.-T., Ostriker, E. C., & Stone, J. M. 2002, ApJ, 581, 1080

Larson, R. B. 1990, ASSL Vol. 162: Physical Processes in Fragmentation and Star Formation, 389

Lin, D. N. C., Laughlin, G., Bodenheimer, P., & Rozyczka, M. 1998, Science, 281, 2025

Luhman, K. L. 2005, ApJ, 633, L41

Marcy, G. W., & Butler, R. P. 2000, PASP, 112, 137

Martin, E. L., Zapatero Osorio, M. R., & Rebolo, R. 1998, ASP Conf. Ser. 134: Brown Dwarfs and Extrasolar Planets, 134, 507

Martín, E. L., Brandner, W., Bouvier, J., Luhman, K. L., Stauffer, J., Basri, G., Zapatero Osorio, M. R., & Barrado y Navascués, D. 2000, ApJ, 543, 299

Masunaga, H., & Inutsuka, S.-i. 2000, ApJ, 531, 350

Mayor, M., Udry, S., & Queloz, D. 1998, ASP Conf. Ser. 154: Cool Stars, Stellar Systems, and the Sun, 154, 77

Muench, A. A., Alves, J., Lada,C. J., and Lada, E. A. 2001, ApJ, 558, L51

Reipurth, R. & Clarke, C. 2001, ApJ, 122, 432

Schneider, G. 2005, HST Proposal, 6858

Stahler, S. W., & Palla, F. 2004, *The Formation of Stars* (2004 WILEY-VCH Verlag GmbH & Co. KGaA, Weinheim)

Toomre, A., & Toomre, J. 1972, ApJ, 178, 623

Watkins, S. J., Bhattal, A. S., Boffin, H. M. J., Francis, N., & Whitworth, A. P. 1998, MNRAS, 300, 1205

Watkins, S. J., Bhattal, A. S., Boffin, H. M. J., Francis, N., & Whitworth, A. P. 1998, MNRAS, 300, 1214

Wright, J. T., Butler, R. P., Marcy, G. W., Vogt, S. S., Fischer, D. A., Tinney, C. G., & Jones, H. R. A. 2005, American Astronomical Society Meeting Abstracts, 207,

Chapter 5

Conclusions

A series of simulations of protostellar disk encounters and fragmentation were presented. The simulations, for the first time, resolve both the local Jeans Mass during fragmentation and the disks' finite scale heights. The influence of the disks' Toomre Q parameter on fragmentation was studied, followed by exploration of the encounter parameter space including the disk-orbit configuration and relative encounter velocities. Properties and further evolution of the resultant fragments were then discussed. The results confirm the conclusion of Watkins et al. (1998a,b) and Lin et al. (1998) that the physical impact of extended protostellar disks can induce the formation of substellar objects, but also find the fragmentation can only take place under certain conditions, and different configurations can result in different mechanism of fragmentation.

Encounters can lower the initial Toomre Q parameter in the inner disk and, if the minimum value of Toomre Q in the disk can be lowered below a critical value, the disk undergoes fragmentation. In this study, the criterion is $Q_{crit} = 0.9$. For a relatively high initial Q disk with $Q_{ini} \geq 1.3$, fragmentation cannot happen since the encounter is not able to decrease the Q down to less than 0.9. This upper limit restricts encounter-induced fragmentation, but since most early disks are massive and cold ($T \sim 10K$), the condition $Q_{ini} \lesssim 1.1$ is likely to be satisfied so that disk-disk encounters should be one of the important scenarios in the formation of substellar objects.

The simulations demonstrate that shock layers, tidal tails and inner disk instabilities can all cause fragmentation. The effectiveness of each mechanism is closely related to the encounter configuration. Shock layers only form and fragment in coplanar encounters; tidal tails are generated by spin-orbit resonance only in prograde disks; and disk instabilities can be induced by either inner disk accretion as in the retrograde encounters, or by tidal tails as in the prograde encounters. Fragments formed from shock layers are usually unbound to the stars, and can sometimes acquire high vertical velocities and easily leave the system. Tidal tail formation may provide an efficient mechanism of star capture and binary formation, and may induce circumbinary disk fragmentation (case 9 in Chapter 3). But the fragmentation of the filamentary structures themselves can only occur in the dense region between the two disks (case 6 in Chapter 3). No condensation happens in the tail far away from the inner disk as described in Lin et al. (1998). Also, the number of fragments usually decreases with the encounter speed, because the interaction is too fast to sufficiently perturb the evolution of the inner disks when the encounter speed is high.

The mass of the resultant 32 clumps are in the range of 1-75 Jupiter Masses, with the majority in the brown dwarf region. The number of clumps with mass less than $5M_J$ may be numerically suppressed due the gravitational softening. The mass distribution shows a decreasing trend toward the high mass end, roughly consistent with the observed IMF in Pleiades. The clumps usually have very high spin angular momenta and disk-like shapes, which imply that young brown dwarfs may also have disks, bipolar jets, or planetary mass companions. Further evolution of the clumps may then result in free floating brown dwarfs or brown dwarf companions to stars. By the end of simulation there are no clumps in the orbit less than 3 AU, which is consistent with the observational "brown dwarf desert". The orbital eccentricity distribution and the average eccentricity are similar to the observed values of brown dwarfs. Orbit interaction in multiples can cause ejection which keeps the ejected clumps in the substellar mass range, but the gas-dissipative environment after the encounters may also help the clumps prevent accreting significant mass.

A resolution study was undertaken to explain the discrepancy between this work and previous studies of protostellar disk encounters. It was demonstrated that unresolved vertical structure of the disk as well as insufficient resolution could result in artificial fragmentation in both isolated disks and in dynamical interacting disks. Therefore, it is essential for the simulation to resolve the Jeans Mass and the vertical structure to obtain trustworthy fragmentation results.

Heating and cooling rate in the retrograde coplanar case were calculated and compared in order to test the local isothermal assumption. The results show that although the heating rate increases significantly during the encounter, it still has the same magnitude as the disk's cooling rate. Therefore, the use of locally isothermal condition is acceptable during the encounter, and is not expected to affect the result significantly.

Fruitful avenues for future works include studies of thermal regulation during the encounters and studies of the further evolution of the fragments. As stated in the first chapter, thermal regulation is very important in fragmentation studies. Though a simulation with local isothermal condition still gives a reasonable picture, it cannot provide the correct thermal properties of the resultant fragments. A more realistic simulation of protostellar disk encounters should include radiative transfer and explore how various factors such as the dust component and disk geometry can affect the fragmentation, and obtain correct temperatures and detailed structures of the clumps.

Further evolution of the disk-like fragments is interesting because it will allow detailed observational predictions of brown dwarf disks and outflows. Numerically, it is hard for a simulation to cover the whole range of timescales from the extended disk encounter down to the internal evolution of brown dwarf disks. It is the task for future work to separate the small scale evolution from the whole simulation and focus on the evolution of the brown dwarf disk systems.

Bibliography

Lin, D. N. C., Laughlin, G., Bodenheimer, P., & Rozyczka, M. 1998, Science, 281, 2025

Watkins, S. J., Bhattal, A. S., Boffin, H. M. J., Francis, N., & Whitworth, A. P. 1998, MNRAS, 300, 1205

Watkins, S. J., Bhattal, A. S., Boffin, H. M. J., Francis, N., & Whitworth, A. P. 1998, MNRAS, 300, 1214